

NASA Contractor Report 198504

Aeropropulsion Technology (APT)

Task 23—Stator Seal Cavity Flow Investigation

N.J. Heidegger, E.J. Hall, and R.A. Delaney
Allison Engine Company
Indianapolis, Indiana

December 1996

Prepared for
Lewis Research Center
Under Contract NAS3-25950



National Aeronautics and
Space Administration

Preface

This report was prepared by Nathan J. Heidegger, Edward J. Hall, and Robert A. Delaney of the Allison Engine Company, Indianapolis, IN. The work was performed under NASA Contract NAS3-25950 from June, 1994 to August, 1996. Principal investigator for this program was Nathan J. Heidegger. The Allison Program Manager for this contract was Robert A. Delaney. The NASA Project Manager was Michael D. Hathaway.

Acknowledgements

The authors would like to express their appreciation to the following people who contributed to this program:

Drs. Michael Hathaway, Anthony Strazisar, and John Adamczyk, NASA Lewis Research Center, and Mr. Peter Tramm and Mr. Richard Alverson, Allison, for their suggestions, and guidance throughout the duration of this contract.

Dr. Steven Wellborn, Allison, for the several discussions of seal cavity dynamics and his concurrently collected experimental seal cavity data.

Jim Forry, Allison, for his secondary flow experience and his suggestions with respect to the seal cavity parameterized study.

Staffs of the NASA Lewis LACE Cluster and the NASA Ames HPCCP/CAS Project, where the majority of the numerical solutions were collected.

Contents

1	SUMMARY	1
2	INTRODUCTION	3
3	HIGH-SPEED COMPRESSOR SEAL CAVITY STUDY	7
3.1	Introduction	7
3.2	High-Speed Compressor Model Selection	7
3.3	Grid Generation	8
3.4	<i>ADPAC</i> Navier-Stokes Numerical Algorithm	10
3.5	Data Reduction	12
3.6	Grid Resolution Study	12
3.6.1	Grid Resolution Sensitivity Results	14
3.7	Rotor-Stator-Rotor Interaction with a Seal Cavity	16
3.7.1	Rotor-Stator-Rotor Performance Comparison	20
3.7.2	Axisymmetrically-Averaged Solution Comparison	21
3.7.3	Detailed Near-Hub Flow Field Comparison	21
3.7.4	Spanwise Profile Comparison	24
3.8	Isolated Upstream Rotor Study	28
3.8.1	Upstream Rotor Performance Re-evaluation	33
3.9	Isolated Stator Analysis	34
3.9.1	Isolated Stator Results	37
4	SEAL CAVITY PARAMETERIZED STUDY	49
4.1	Introduction	49
4.2	Seal Cavity Parameter Selection	49
4.2.1	Test Matrix Development	51
4.3	Figures of Merit	51
4.4	Parameter Study Grid Generation	53
4.4.1	Definition of the Coupled Geometry	53
4.4.2	Axisymmetric Distribution of the Points	54
4.4.3	Pitchwise Distribution of Points	54
4.5	Numerical Solution Collection and Post-Processing	57
4.6	Baseline Case Description	58
4.6.1	Comparison of 3-D and 2-D Axisymmetric Seal Cavity Solutions	59
4.6.2	Pitchwise Distributions in the Cavity Trenches	63

4.7	Comparison of All Parameterized Cases	63
4.8	Tooth Gap Parameter	69
4.8.1	Comparison with Current Design Methods	76
4.9	Lower Wheel Speed Cavity Case	78
4.10	Cavity Depth Parameter	84
4.11	Hub Radial Mismatch Parameter	90
4.12	Axial Trench Gap Parameter	99
4.13	Hub Corner Parameter	105
4.14	Stator Land Edge Parameter	111
4.15	Rim Seal Cavity Configuration	116
5	CONCLUSIONS	121
A	<i>ADPAC</i> Solution Collection on Various Platforms	131

List of Figures

2.1	Schematic of typical high-speed axial compressor with close-up view of the seal cavity region under the inner-banded stator.	4
3.1	Rotor-stator-rotor geometry showing the detailed seal cavity under the stator of a high-speed compressor.	8
3.2	Axisymmetric slice from the stator seal cavity mesh with triple-knife seal.	9
3.3	Solid surfaces for the coupled seal cavity and main flow path grids for the stator of a high-speed compressor.	9
3.4	Axisymmetric slice from the stator seal cavity mesh with a single-knife seal.	10
3.5	Radial distributions into the seal cavity trenches of absolute flow angle between experimental measurements and <i>ADPAC</i> predictions of the NASA Low-Speed Axial Compressor (LSAC) showing the ability of <i>ADPAC</i> to model the seal cavity flow correctly.	11
3.6	Schematic diagram of the stator and seal cavity identifying position of the four measuring stations and the seal cavity trench locations. . . .	13
3.7	Comparison of the four grid resolutions used in the grid study including the total number of grid points in the corresponding 3-D grid with the seal cavity and grid extensions.	15
3.8	Comparison of radial distributions of the stator blade performance between mesh Levels 1, 2, 3, and 4 for the no cavity geometry.	17
3.9	Comparison of radial distributions of the stator blade performance between mesh Levels 1, 2, 3, and 4 for the nominal gap seal cavity geometry.	18
3.10	Radial distributions of area-averaged flow quantities (across constant radial grid index planes) into the upstream and downstream seal cavity trenches on mesh Levels 1, 2, 3 and 4, for the standard nominal gap seal cavity configuration.	19
3.11	Contours of static pressure and axial velocity taken from the axisymmetrically-averaged <i>ADPAC</i> fine-mesh mixing-plane solution of the rotor/stator/rotor geometry with the seal cavity.	22
3.11	Contours of radial velocity and tangential velocity taken from the axisymmetrically-averaged <i>ADPAC</i> fine-mesh mixing-plane solution of the rotor/stator/rotor geometry with the seal cavity.	23

3.12	Contours of radial velocity located one computational cell above the hub surface for the two coarse-mesh (Level 2) rotor-stator-rotor <i>AD-PAC</i> solutions.	25
3.13	Axial location of spanwise profile stations between the rotor and stator blades.	26
3.14	Spanwise profiles of total pressure, total temperature, axial velocity, and tangential velocity at the upstream rotor inlet.	26
3.15	Spanwise profiles of total pressure, total temperature, axial velocity, and tangential velocity at the upstream rotor / stator interface. . . .	27
3.16	Spanwise profiles of total pressure, total temperature, axial velocity, and tangential velocity at the stator / downstream rotor interface. . .	27
3.17	Spanwise profiles of total pressure, total temperature, axial velocity, and tangential velocity at the downstream rotor exit.	28
3.18	Grid distribution at the hub surface from the isolated upstream rotor grid with the grid block extensions. (Grid has been copied one rotor blade pitch to clarify blade shape.)	29
3.19	Inlet total pressure profiles tested with the isolated upstream rotor. .	30
3.20	Pressure ratio and efficiency speed lines for the upstream rotor at 100% rotation speed for the range of inlet profiles tested. (Note: The solid symbols represent cases to be compared later within the chapter.) . .	31
3.21	Spanwise profiles of the upstream rotor blade performance for Inlet Profiles A and C.	32
3.22	Spanwise profiles of the upstream rotor exit flow for Inlet Profiles A and C.	32
3.23	Pressure ratio and efficiency 100% constant speed lines for the upstream rotor using the scaled stator profile with cavity effects compared with other inlet profiles tested. (Note: The solid symbols represent cases to be compared later within the chapter.)	33
3.24	Spanwise profiles of the upstream rotor blade performance using the scaled stator exit profile that included the seal cavity effects.	34
3.25	Spanwise profiles of the upstream rotor exit flow used as inlet conditions for the stator.	35
3.26	Axisymmetric outlines of the stator flow path and the four various seal cavity geometries tested.	35
3.27	Axisymmetric slice of the single-knife seal cavity grid (Level 3 grid resolution) with the knife seal clearance gap doubled radially.	36
3.28	Axisymmetric slice of the seal cavity without any knife seals (Level 3 grid resolution)	36
3.29	Radial distributions of axial and tangential velocities from the four measuring stations through the stator.	39
3.30	Radial distributions of flow angles, incidence, and deviation from the four measuring stations through the stator.	40
3.31	Radial distributions of the stator blade performance parameters measured across the outside stations (UP and DN).	41

3.32	Radial distributions of area-averaged flow quantities into the upstream and downstream seal cavity trenches for various seal cavity configurations.	43
3.33	Near-wall axial velocity distributions along the hub and suction surfaces of the stator blade showing the variation in separation region between the four seal cavity configurations.	44
3.34	Axial velocity distributions across the trailing edge plane showing the regions of reversed flow.	45
3.35	Stator blade incidence measured upstream of the seal cavity gap and at the leading edge.	46
3.36	Particle traces released from the leading edge of the upstream seal cavity trench showing the blockage associated with the different seal cavity geometries tested.	46
3.37	Axisymmetric-averaged tangential velocity distributions through the seal cavity as measured by wheel speed. The bold contour line represents the 50% wheel speed line.	48
4.1	Geometric parameters defining the overall seal cavity geometry. . . .	50
4.2	Geometric parameters defining the individual seal tooth geometry. . .	50
4.3	Test matrix of geometric parameters to be tested from the Baseline case.	52
4.4	Meridional plane mesh distribution for the baseline triple-knife seal cavity coupled to the stator main flow path. Details of the upstream and downstream interface regions are highlighted in the lower half of the figure.	55
4.5	Comparison of the grids around the leading and trailing edges at the hub surface from the previous and new grid generation methods. . . .	56
4.6	Meridional slice of the Baseline configuration mesh showing the coupled stator and seal cavity.	58
4.7	Location of upstream and downstream plenums (dotted lines) for simulation of the main flow in the axisymmetric solution.	60
4.8	Comparison of radial distributions at upstream mid-trench axial location between the averaged full 3-D baseline solution and the 2-D axisymmetric solution.	61
4.9	Comparison of radial distributions at downstream stream mid-trench axial location between the averaged full 3-D baseline solution and the 2-D axisymmetric solution.	62
4.10	Spanwise locations where flow quantities were mass-averaged generating the pitchwise distributions across the upstream and downstream trench gaps.	64
4.11	Pitchwise variation of flow quantities mass-averaged across the upstream trench gap at several spanwise radii for the Baseline case. . . .	65
4.12	Pitchwise variation of flow quantities mass-averaged across the downstream trench gap at several spanwise radii for Baseline case.	66
4.13	Comparison of the figures of merit for all parameterized seal cavity solutions collected.	68

4.14	Meridional plane grids showing the variation of the Seal Tooth Gap parameter.	70
4.15	Axisymmetrically-averaged particle traces within the seal cavity for the Tooth Gap parameter series.	71
4.16	Radial profiles of axial and tangential velocities upstream and downstream of the stator blade for variations of the Tooth Gap parameter.	72
4.17	Radial profiles of flow angles upstream and downstream of the stator blade, and incidence and deviation for variations of the Tooth Gap parameter.	73
4.18	Radial profiles of stator blade performance parameters measured across the stator blade for variations of the Tooth Gap parameter.	74
4.19	Zero axial velocity contour line at the near-hub location for the No Cavity, No Gap, Baseline, 2x Tooth Gap, and 4x Tooth Gap configurations.	75
4.20	Leakage flow rate comparison between 3-D <i>ADPAC</i> seal cavity solutions and BC88 seal cavity solutions.	77
4.21	Alternating black and white passages of particle traces released in the upstream cavity trench for the Baseline case.	79
4.22	Alternating black and white passages of particle traces released in the upstream cavity trench for the Lower Wheel Speed case.	80
4.23	Comparison of radial profiles of change in total pressure and total temperature distributions across the stator blade between the No Cavity case, the Baseline case, and the Lower Wheel Speed case.	80
4.24	Radial profiles of axial and tangential velocities upstream and downstream of the stator blade for the Lower Wheel Speed case.	81
4.25	Radial profiles of flow angles upstream and downstream of the stator blade, and incidence and deviation for the Lower Wheel Speed case.	82
4.26	Radial profiles of stator blade performance parameters measured across the stator blade for the Lower Wheel Speed case.	83
4.27	Meridional plane grids showing the variation of the Seal Cavity Depth parameter.	85
4.28	Axisymmetrically-averaged particle traces within the seal cavity for the Cavity Depth parameter series.	86
4.29	Radial profiles of axial and tangential velocities upstream and downstream of the stator blade for variations of the Cavity Depth parameter.	87
4.30	Radial profiles of flow angles upstream and downstream of the stator blade, and incidence and deviation for variations of the Cavity Depth parameter.	88
4.31	Radial profiles of stator blade performance parameters measured across the stator blade for variations of the Cavity Depth parameter.	89
4.32	Meridional plane grids showing the variation of the Hub Radial Mismatch parameter.	91
4.33	Axisymmetrically-averaged particle traces within the seal cavity for the Radial Mismatch parameter series upstream of the stator blade.	92

4.34	Axisymmetrically-averaged particle traces within the seal cavity for the Radial Mismatch parameter series downstream of the stator blade. . .	93
4.35	Schematic diagrams of the four different Radial Mismatch parameter cases showing the general area trend in the shaded area.	95
4.36	Radial profiles of axial and tangential velocities upstream and downstream of the stator blade for variations of the Hub Radial Mismatch parameter.	96
4.37	Radial profiles of flow angles upstream and downstream of the stator blade, and incidence and deviation for variations of the Hub Radial Mismatch parameter.	97
4.38	Radial profiles of stator blade performance parameters measured across the stator blade for variations of the Hub Radial Mismatch parameter.	98
4.39	Meridional plane grids showing the variation of the Axial Trench Gap parameter.	100
4.40	Axisymmetrically-averaged particle traces within the seal cavity for the Axial Trench Gap parameter series.	101
4.41	Radial profiles of axial and tangential velocities upstream and downstream of the stator blade for variations of the Axial Trench Gap parameter.	102
4.42	Radial profiles of flow angles upstream and downstream of the stator blade, and incidence and deviation for variations of the Axial Trench Gap parameter.	103
4.43	Radial profiles of stator blade performance parameters measured across the stator blade for variations of the Axial Trench Gap parameter.	104
4.44	Meridional plane grids showing the variation of the Hub Corner Treatment parameter.	106
4.45	Axisymmetrically-averaged particle traces within the seal cavity for the Hub Corner parameter series.	107
4.46	Radial profiles of axial and tangential velocities upstream and downstream of the stator blade for variations of the Hub Corner parameter.	108
4.47	Radial profiles of flow angles upstream and downstream of the stator blade, and incidence and deviation for variations of the Hub Corner parameter.	109
4.48	Radial profiles of stator blade performance parameters measured across the stator blade for variations of the Hub Corner parameter.	110
4.49	Meridional plane grids showing the variation of the Stator Land Edge Treatment parameter.	111
4.50	Axisymmetrically-averaged particle traces within the seal cavity for the Stator Land Edge parameter.	112
4.51	Radial profiles of axial and tangential velocities upstream and downstream of the stator blade for variations of the Stator Land Edge parameter.	113
4.52	Radial profiles of flow angles upstream and downstream of the stator blade, and incidence and deviation for variations of the Stator Land Edge parameter.	114

4.53	Radial profiles of stator blade performance parameters measured across the stator blade for variations of the Stator Land Edge parameter. . .	115
4.54	Meridional plane grids showing differences between the Baseline configuration and the Rim Seal configuration.	116
4.55	Particle traces released in the cavity region of the Rim Seal configuration.	117
4.56	Radial profiles of axial and tangential velocities upstream and downstream of the stator blade for the Rim Seal Geometry.	118
4.57	Radial profiles of flow angles upstream and downstream of the stator blade, and incidence and deviation for the Rim Seal Geometry. . . .	119
4.58	Radial profiles of stator blade performance parameters measured across the stator blade for the Rim Seal Geometry.	120

List of Tables

3.1	Mass flow rates through the stator blade passage and the cavity passage for mesh Levels 1, 2, 3, and 4 for the standard nominal gap seal cavity geometry.	14
3.2	Mass flow rates through the stator blade passage and the cavity passage for the four different seal cavity configurations.	37
4.1	Parameter lists dividing parameters into Top and Lower Levels. . . .	51
4.2	Lists of primary figures of merit used to evaluate the several parameterized seal cavity solutions.	53
A.1	Run times from three different computing resources for a typical seal cavity problem.	132

NOTATION

A list of the symbols and acronyms used throughout this document and their definitions are provided below for convenience.

Roman Symbols

i . . . incidence angle
m . . . mass flow rate
p . . . pressure
r . . . radius or radial coordinate
x . . . axial coordinate
ADPAC . . . Advanced Ducted Propfan Analysis Code
ADSPIN . . . ADPAC post processing program
APPL . . . Application Portable Parallel Library
AST . . . Advanced Subsonic Technologies
CAS . . . Computational Aerosciences
CFD . . . computational fluid dynamics
DF . . . diffusion factor
GRIDGEN . . . multiple block general purpose mesh generation system
IGES . . . Initial Graphics Exchange Specification
LACE . . . NASA Lewis Advanced Cluster Environment

LSAC ... NASA Lewis Low-Speed Axial Compressor
LSF ... Load Sharing Facility
MPI ... Message Passing Interface
NQS ... Network Queuing System
PBS ... Portable Batch System
PLOT3D ... post-processing 3-D visualization tool
PVM ... Parallel Virtual Machine
 R_c ... pressure ratio
 T ... temperature
TIGG3D ... NASA-Lewis multiple splitter mesh generation program
 U_{tip} ... rotor tip speed
 V ... velocity

Greek Symbols

Δ ... change in
 β ... flow angle
 δ ... deviation angle
 η ... efficiency
 θ ... tangential coordinate
 μ ... coefficient of viscosity
 ρ ... density
 σ ... blade row solidity
 ω ... rotational speed or loss coefficient
 ω_p ... loss parameter

Subscripts

$[]_{CAV}$... seal cavity
 $[]_{DESIGN}$... design value
 $[]_{DN}$... downstream measuring station
 $[]_{LE}$... leading edge measuring station
 $[]_r$... pertaining to the radial (r) cylindrical coordinate
 $[]_{REF}$... reference value
 $[]_s$... static value
 $[]_t$... total (stagnation) value or tangential direction
 $[]_{TE}$... trailing edge measuring station
 $[]_{UP}$... upstream measuring station
 $[]_x$... pertaining to the axial (x) cylindrical coordinate
 $[]_\theta$... pertaining to the circumferential (θ) cylindrical coordinate

Chapter 1

SUMMARY

The focus of NASA Contract NAS3-25950 Task 23 was to numerically investigate the flow through an axial compressor inner-banded stator seal cavity. The Allison/NASA developed *ADPAC* code was used to obtain all flow predictions. This task includes sections concentrated on a high-speed compressor study and a detailed parameterized study of seal cavity geometry.

Under the High-Speed Compressor study, *ADPAC* was applied to compute the flow through an inner-banded stator seal cavity of a multi-stage compressor. The 8th stator seal cavity of Allison's Advanced Subsonic Technology (AST) Candidate Compressor was selected as the high-speed model. Flow through a labyrinth stator seal cavity of the compressor was modeled by coupling the cavity flow path and the main flow path of the compressor. A grid resolution study was performed to guarantee adequate grid spacing was used. Both unsteady rotor-stator-rotor interactions and steady-state isolated blade calculations were performed with and without the seal cavity present.

The detailed parameterized seal cavity study of the high-speed stator seal cavity was performed by collecting a series of solutions for several different geometric variations. The geometric parameter list included seal tooth gap, cavity depth, wheel speed, radial mismatch of hub flowpath, axial trench gap, hub corner treatments, and land edge treatments. Again as above, the *ADPAC* code was used to solve both the seal cavity flow and the stator flow fields simultaneously. Solution data presented includes radial and pitchwise distributions of flow variables and particle traces describing the flow character. Significant conclusions drawn from the several numerical solutions of the coupled stator/cavity geometry include:

- Approximately 500,000 mesh points were needed to adequately resolve the coupled 3-D seal cavity and stator blade flow fields;
- Mixed positive and negative radial flows exist across *both* the upstream and downstream seal cavity / main flow interface regions;
- Driven cavity-like flow structures occur in both seal cavity trenches;
- There were large increases in tangential velocity of leakage flow as it passes through the seal cavity (up to 75% of hub wheel speed);

- Exit tangential velocity of the leakage flow plays a critical role in suction side separation near the hub.

Chapter 2

INTRODUCTION

In a high-speed axial compressor, the function of the stator seal cavity is to provide a flow seal between the rotating rotor wheel and the stationary inner-band stabilizing the stator vanes shown in Figure 2.1. Due to the increasing pressure in the axial direction, the driving potential causes the fluid to flow back through the seal cavity. Several different sealing mechanisms have been tested and employed to reduce the amount of mass flow traveling through the seal cavity, referred to as leakage flow, in order to minimize the associated losses [1, 2]. As axial compressor designs become more aggressive, the pressure differential across the stator seal cavity will become larger. To minimize inefficiencies due to the interaction between the two separate flow paths, the dynamics of the seal cavity and more importantly its effect on the main power stream must be fully understood,

Several investigations have been conducted focusing on the rotating cavity problem [3, 4, 5, 6]. The majority of these studies has been directed at the turbine sections of the engine and were primarily concerned with the balance of cool compressor bleed flow and the hot main gas path ingestion problem [7, 8]. Some experimental work has been collected for individual seal cavities and for the coupled system on lower rotational speed compressors [9]. However, due to the difficulty of obtaining data in the complex geometries of a high-speed compressor seal cavity, little experimental data for these configurations are available. The use of computational fluid dynamics (CFD) as an investigative tool becomes very useful in this situation.

CFD has been used previously to model individual compressor blades in previous compressor work at Allison and researchers have also implemented CFD to solve individual seal cavities [10]. Some research has coupled the turbine cavities to the main flow path [11, 12, 13]. The work presented within this report will focus not on the individual blade solution or the separate seal cavity solution, but the coupled system and the interaction between the two flow paths.

Using CFD in a parameterized study allows for “quick” geometry modifications using grid generation tools, as compared to machining experimental hardware. By selecting appropriate geometric parameters that emphasize the interface region between the seal cavity and the main flow path, results from the numerical solutions can provide insight and guidance to the critical design aspects of reducing any negative effects of the seal cavity flow.

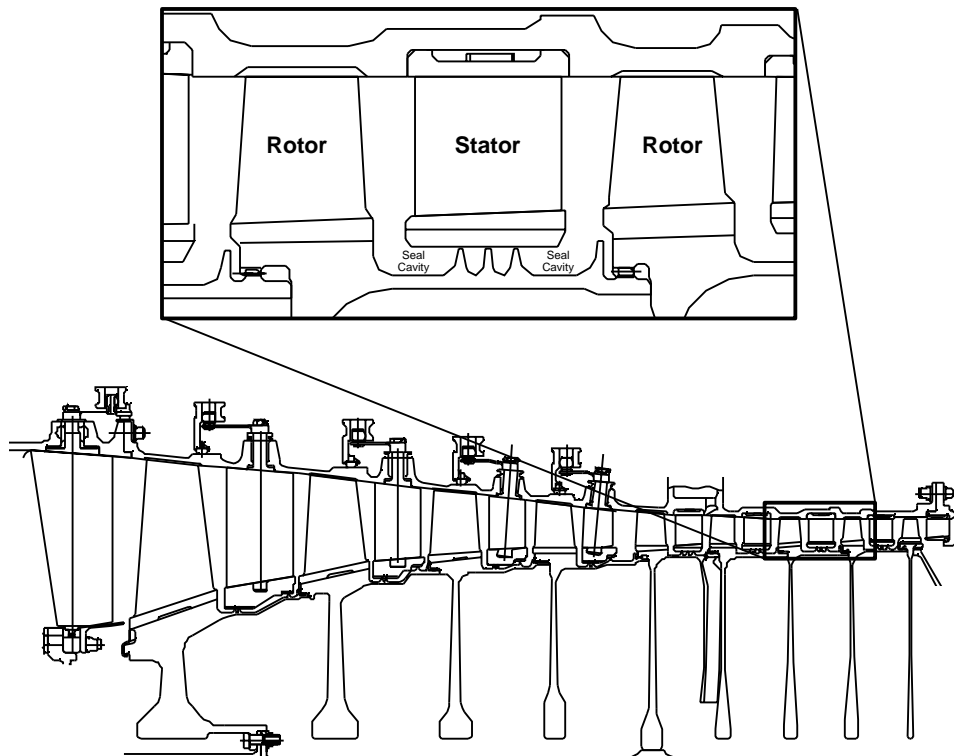


Figure 2.1: Schematic of typical high-speed axial compressor with close-up view of the seal cavity region under the inner-banded stator.

This report contains two main chapters covering the High-Speed Compressor Seal Cavity Study and the Seal Cavity Parameterized Study. The chapter over the high-speed study includes sections on the seal cavity model selection, grid generation, the *ADPAC* flow solver code, and data reduction. A section on the grid resolution study performed to guarantee adequate mesh spacing follows along with results from both the multiple blade row and the isolated stator flow simulations. The parameterized study chapter introduces the set of geometric seal cavity parameters and figures of merit used in the study. Results, including radial distributions of flow quantities and particle traces, are included for each of the parameters tested. A few important conclusions drawn from this work are the better description of the flow structure inside the seal cavity (including the mixed positive/negative radial flow across the hub boundary and the rotating regions of flow in the seal cavity trenches) and the impact of the tangential velocity increase of the leakage flow as it re-enters the main flow.

Chapter 3

HIGH-SPEED COMPRESSOR SEAL CAVITY STUDY

3.1 Introduction

Flow through a labyrinth stator seal cavity of a high-speed compressor was modeled by coupling the cavity flow path and the main flow path of the compressor. A grid resolution study was performed to guarantee adequate grid spacing was used. Both unsteady rotor-stator-rotor interactions and steady-state isolated blade calculations were performed with and without the seal cavity present. Significant findings included the discovery of “driven cavity”-like flow structures in the seal cavity trenches, the mixture of *both* positive and negative radial flow across both upstream and downstream trench hub boundaries, the influence of the downstream rotor, and the large increase in tangential velocity of the leakage flow and its effect on the stator blade incidence. This chapter includes sections on the seal cavity model selection, grid generation, data reduction, and the grid resolution study. Results are presented for the rotor-stator-rotor interaction with a seal cavity, the isolated upstream rotor, and the isolated stator with and without the cavity present. Variations in seal tooth gap were performed with the isolated stator study.

3.2 High-Speed Compressor Model Selection

The model seal cavity selected for this study was the eighth-stage stator seal cavity of Allison’s Advanced Subsonic Technologies (AST) Candidate 10-stage compressor. The outline of seal cavity geometry and nearby blades is shown in Figure 3.1. While the AST compressor is an advanced design with an aggressive pressure ratio, selecting a rear stage from this machine, where changes in flowpath are minimal, allowed the investigation to venture into a higher wheel speed stage while still maintaining several characteristics of current rear compressor stage designs.

Shown in Figure 3.1, the cavity geometry consists of a triple-knife labyrinth seal and a dam located to the far right of the cavity. This dam is used for the axial alignment of the rotor blades in the downstream blade row and is not used in a

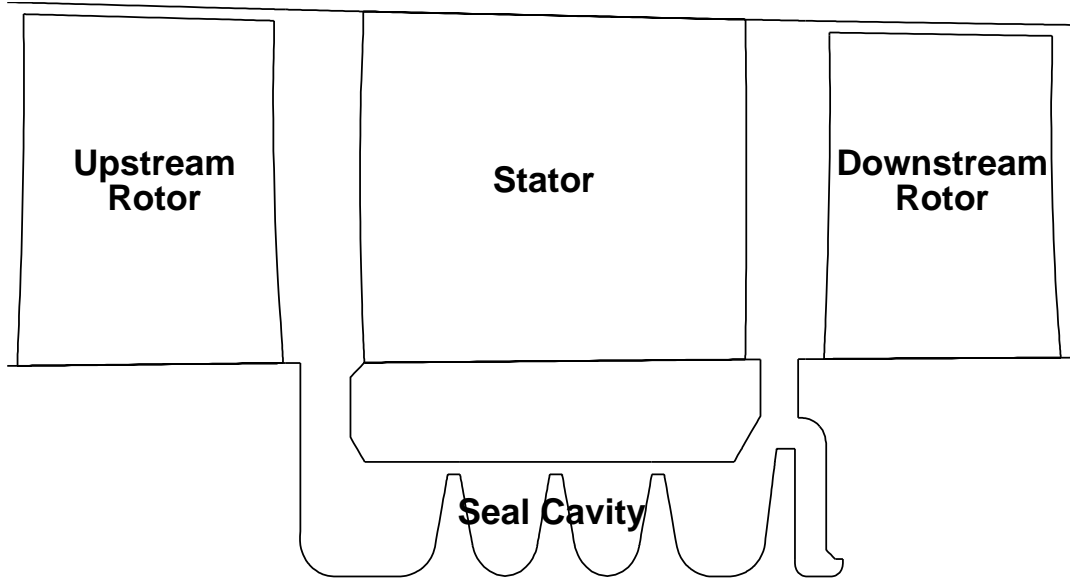


Figure 3.1: Rotor-stator-rotor geometry showing the detailed seal cavity under the stator of a high-speed compressor.

sealing capacity. For each rotor blade, a small tang hangs down from the rotor base such that the upstream face of the tang touches the downstream face of the dam. The circumferential extent of the tang is approximately one-third the blade pitch; therefore, about two-thirds of the entrance to the small cavity behind the dam is exposed to the main cavity flow. Preliminary 3-D flow solutions found that the amount of flow entering this small cavity was two orders of magnitude smaller than the main cavity recirculating flow and for the most part the mass in the small cavity behind the dam was in a pure rotational state.

3.3 Grid Generation

The complete axisymmetric seal geometry was obtained in an IGES format from CAD drawings. The geometry data was then converted into a database for *GRIDGEN*, a multiple-block mesh generation package. The seal tooth clearance taken from the database was 0.018 inches and will be referred to as the “nominal” value in this chapter. Test cases in the parameterized study, discussed in the next chapter, tested tighter seal tooth clearances. A 2-D grid was generated for the seal cavity using *GRIDGEN* tools. This axisymmetric representation of the triple-knife seal cavity, shown in Figure 3.2, was then mated with the 3-D *TIGG3D*-generated grid [31] of the main stator flow path. Due to the circumferential mating of the seal cavity to the stator passage, the grid topology selection was limited to using a H-grid. The coupled mesh showing the seal cavity in relation to the main flow path and the stator is shown in Figure 3.3.

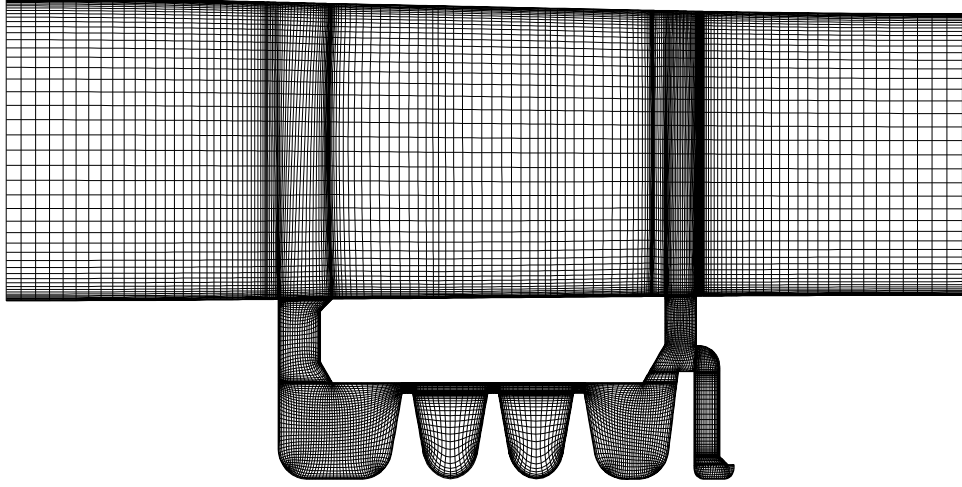


Figure 3.2: Axisymmetric slice from the stator seal cavity mesh with triple-knife seal.

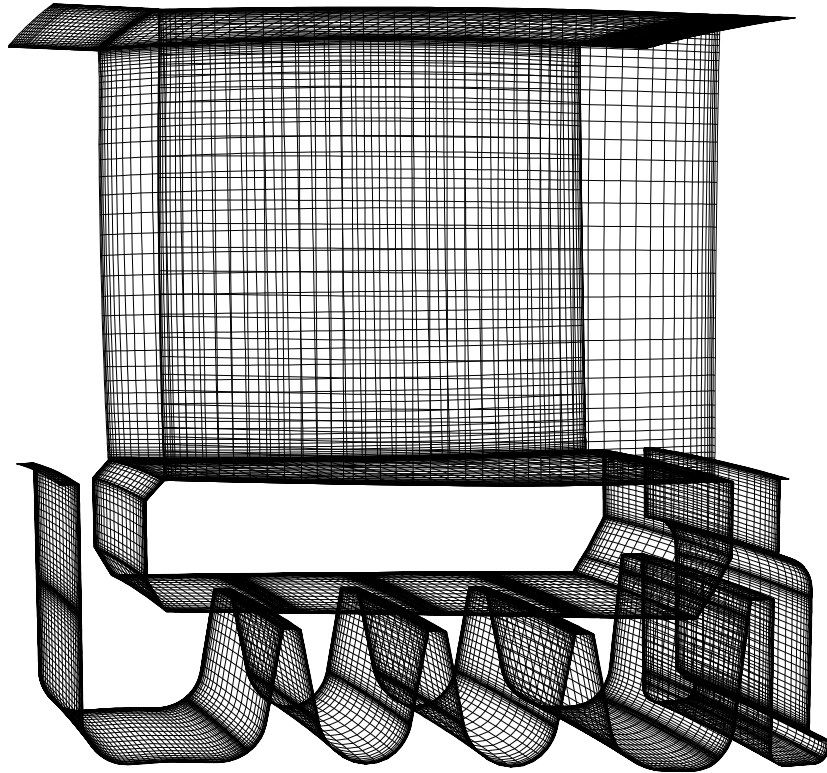


Figure 3.3: Solid surfaces for the coupled seal cavity and main flow path grids for the stator of a high-speed compressor.

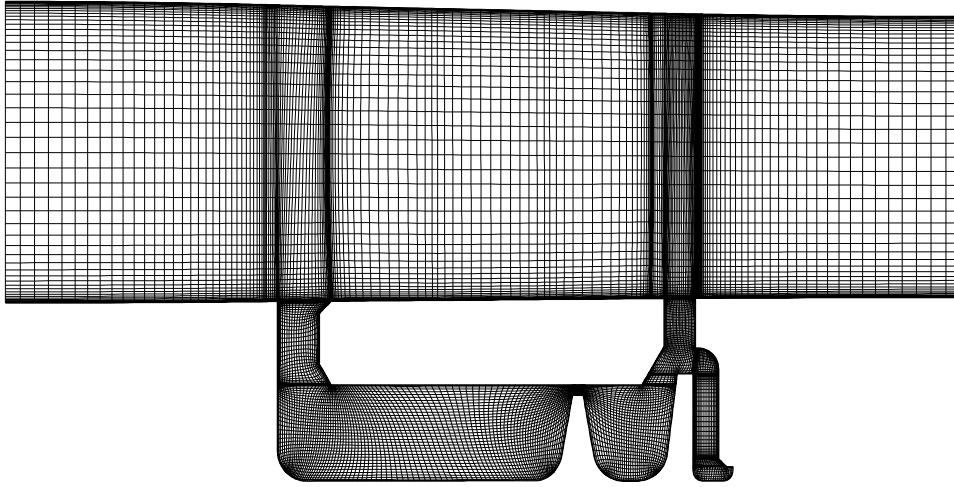


Figure 3.4: Axisymmetric slice from the stator seal cavity mesh with a single-knife seal.

A single-knife seal geometry was also investigated; the number of knife seals was reduced from three to one by removing the two upstream knife seals as shown in the modified axisymmetric representation in Figure 3.4. The most downstream knife seal was kept because in triple-knife cavity solutions this knife seal was performing the vast majority of the sealing and the remaining knives were merely dividing the remaining cavity volume into smaller rotating driven cavities.

3.4 *ADPAC* Navier-Stokes Numerical Algorithm

The aerodynamic predictions for the cases described in this study were obtained using the *ADPAC* analysis code. The *ADPAC* code is a general purpose turbomachinery aerodynamic design analysis tool which has undergone extensive development, testing, and verification [14, 15, 16, 17, 18]. Detailed code documentation is also available for the *ADPAC* program [19, 20, 21]. A brief description of the theoretical basis for the *ADPAC* analysis is given below, and the interested reader is referred to the cited references for additional details.

The *ADPAC* analysis solves a time-dependent form of the three-dimensional Reynolds-averaged Navier-Stokes equations using a proven time-marching numerical formulation. Solutions may be obtained using either a rotating cylindrical coordinate system for annular flows, or a stationary Cartesian coordinate frame for linear cascades or other non-cylindrical geometries. The numerical technique employs proven numerics based on a finite volume, explicit multigrid Runge-Kutta time-marching solution algorithm derived from the developmental efforts of Jameson, Adamczyk, and others [22, 23, 24, 25]. Steady-state flows are obtained as the time-independent limit of the time-marching procedure. Several steady state convergence acceleration techniques (local time stepping, implicit residual smoothing, and multigrid) are available to im-

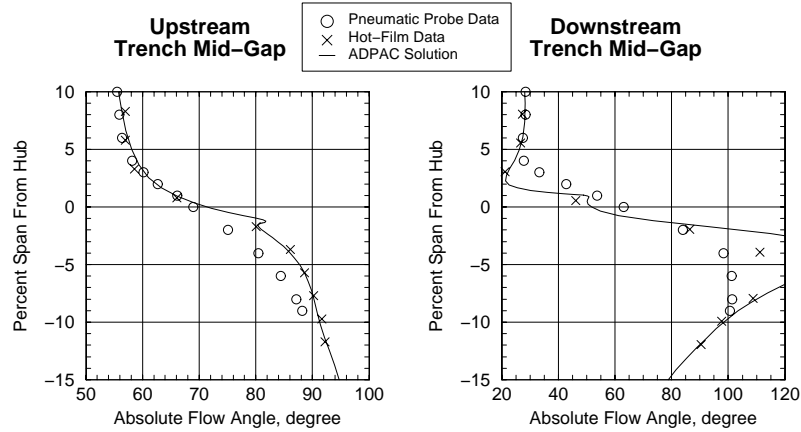


Figure 3.5: Radial distributions into the seal cavity trenches of absolute flow angle between experimental measurements and *ADPAC* predictions of the NASA Low-Speed Axial Compressor (LSAC) showing the ability of *ADPAC* to model the seal cavity flow correctly.

prove the overall computational efficiency of the analysis. An attractive feature of the *ADPAC* code is the versatility and generality of mesh systems upon which the analysis may be performed. The *ADPAC* code permits the use of a multiple-blocked mesh discretization which provides extreme flexibility for analyzing complex geometries such as the coupled stator/seal cavity geometry. The block gridding technique enables the coupling of complex, multiple-region domains with common (non-overlapping) grid interface boundaries through specialized user-specified boundary condition procedures.

Validation of the *ADPAC* code applied to the inner-banded seal cavity geometry was demonstrated under a parallel effort supported under a separate NASA contract [30]. In that work, the NASA Lewis Low-Speed Axial Compressor (LSAC) inner-banded seal cavity and stator passage were solved using *ADPAC*. The numerical results were compared with the experimental data collected for that compressor [9] which included slow-response pneumatic and fast-response hot-film data. Figure 3.5 is presented here as a sample from the parallel effort comparing absolute flow angles measured at the mid-trench gap location both immediately above and below the hub radius. Agreement between the *ADPAC* results and the experimental data was quite good with the *ADPAC* results matching the higher-response hot-film data better than the pneumatic data. Due to the differences in rotational speed and blade setting angle, no direct comparisons will be made between the LSAC data and the numerical *ADPAC* predictions of the high-speed compressor model used in this contract; however, the sample LSAC results show the capability of *ADPAC* to model the complex seal cavity leakage flow coupled to the stator main flow. Interested readers are referred to the cited report for additional details of this validation effort. The success of *ADPAC* to capture the LSAC cavity flow field gives additional confidence to the data presented within this report which tested the coupled stator and seal cavity geometry at much higher rotational speeds, more realistic of an advanced compressor design.

3.5 Data Reduction

The following section briefly describes the procedures followed to reduce the large amount of collected data into the figures presented in this chapter. Overall mass flows were calculated in all cases for both the main flow path and the seal cavity flow path. The seal cavity mass flow was determined from the amount of mass flow over the seal tooth once the solution was converged.

In order to determine the effect of the seal cavity on the main flow path, mass-averaged flow variable data were extracted from the solutions at four measuring stations. These stations, identified in Figure 3.6, were located just upstream of the upstream seal cavity trench, the stator leading edge, the stator trailing edge, and just downstream of the downstream seal cavity trench. Each of these four measuring stations are labeled with a unique subscript (UP, LE, TE, or DN) used as a reference throughout this entire report. The upstream and downstream seal cavity trench locations correspond to the trailing edge of the upstream rotor and the leading edge of the downstream rotor, respectively. The upstream and downstream seal cavity trench regions are also identified in Figure 3.6.

Radial distributions were calculated for various flow variables and blade performance parameters, including turning angle, diffusion factor, loss coefficient, and loss parameter, defined below in Equations 3.1, 3.2, 3.3, and 3.4, respectively. The UP and DN station referenced in the equations correspond to the upstream and downstream measuring stations, respectively, identified in Figure 3.6. The radial terms in the diffusion factor equation were neglected due to the minimal radius change in the stator flowpath. Due to the proprietariness of the flow data, the majority of the data presented within this report has been non-dimensionalized by a meaningful compressor flow quantity; if that was not possible, the variable was replaced by the change in variable to allow for relative comparison of the several solutions.

$$\text{Turning Angle} = |\Delta\beta| = |\beta_{DN} - \beta_{UP}| \quad (3.1)$$

$$\text{Diffusion Factor} = DF = 1 - \frac{V_{DN}}{V_{UP}} + \frac{|\Delta V_\theta|}{2\sigma V_{UP}} \quad (3.2)$$

$$\text{Loss Coefficient} = \omega = \frac{p_{tUP} - p_{tDN}}{p_{tUP} - p_{sUP}} \quad (3.3)$$

$$\text{Loss Parameter} = \omega_p = \frac{\omega \cos \beta_{DN}}{2\sigma} \quad (3.4)$$

3.6 Grid Resolution Study

The detailed analysis of the stator with and without the single-knife seal cavity was performed on four grid resolution levels. The baseline grid from which preliminary results were obtained represents the third finest grid (Level 3) of the four. The two coarsest levels (Levels 1 and 2) were generated by reducing the baseline grid by one and

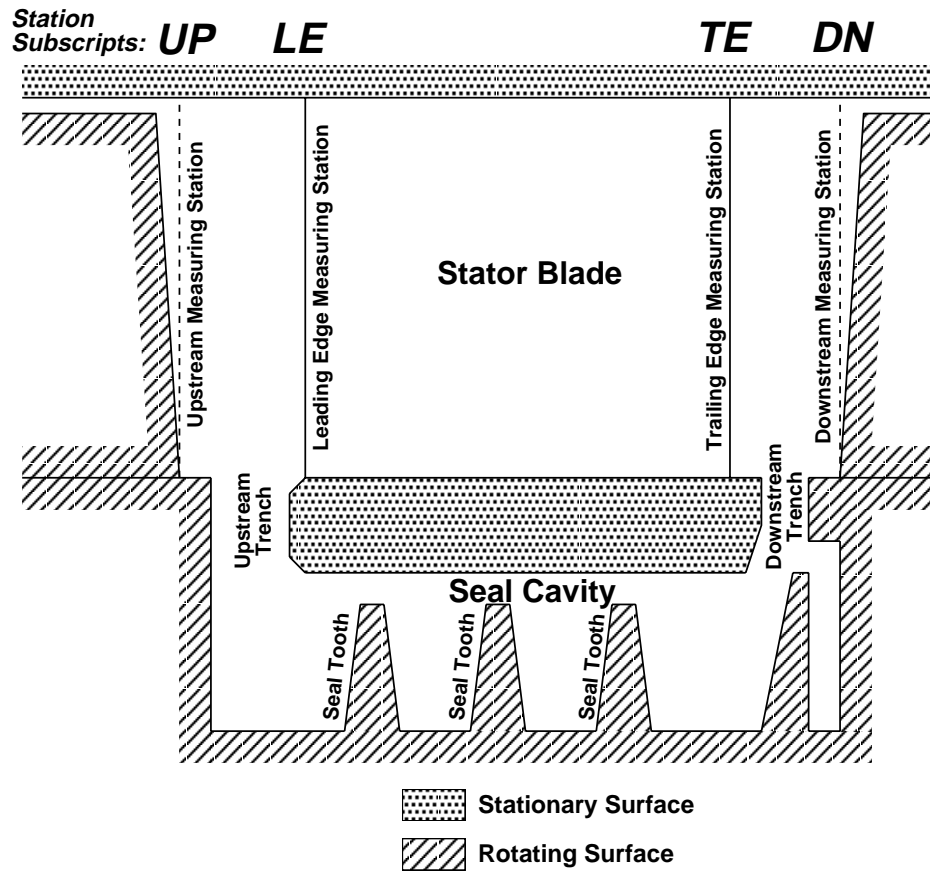


Figure 3.6: Schematic diagram of the stator and seal cavity identifying position of the four measuring stations and the seal cavity trench locations.

Grid Resolution Level	Stator Passage Mass Flow (normalized by Level 4 value)	Seal Cavity Mass Flow (as % of stator mass flow)
Level 1 (11,421 mesh points)	0.936	1.09%
Level 2 (78,897 points)	0.983	1.42%
Level 3 (584,991 mesh points)	0.996	1.74%
Level 4 (1,175,987 mesh points)	1.000	1.73%

Table 3.1: Mass flow rates through the stator blade passage and the cavity passage for mesh Levels 1, 2, 3, and 4 for the standard nominal gap seal cavity geometry.

two levels of multi-grid. The finest level for the grid study (Level 4) was generated by refining the Level 3 databases in *GRIDGEN* and *TIGG3D*, such that the total number of grid points was approximately doubled; this corresponded to an approximate 26% increase in the number of mesh points in each of the three computational indices. Even though the number of mesh points was increased from Level 3 to Level 4, the distance of the first mesh point off the surface was held constant at 0.0005 inches. A meridional slice through the seal cavity from each of the four grid resolution levels is shown for comparison in Figure 3.7. The number of points in the four grids, with the seal cavity included, ranges from approximately 11,000 to 1.2 million.

3.6.1 Grid Resolution Sensitivity Results

Solutions for the stator blade with and without the seal cavity were collected on the four different grid resolutions described above. Table 3.1 lists the mass flow rates of the stator main flow path and the seal cavity flow path for the nominal gap seal cavity geometry. As the grid resolution was refined, mass flow through the stator blade row and the seal cavity increased. This was primarily related to the increased resolution of the boundary layers and their associated blockage effects as the grid spacing became more clustered near the walls of the stator blade and seal cavity. There was very little difference between Levels 3 and 4 with respect to the mass flow values; this was one indication that grid resolution independence had been achieved. This leveling-off of mass flow values could also be attributable to the constant near wall spacing between the Level 3 and Level 4 meshes noted above; therefore, further investigation of grid dependence was performed using radial profiles across the stator span.

Radial profiles of stator blade performance calculated from the solutions on all four grid resolutions levels are shown in Figures 3.8 and 3.9 for the no cavity and nominal gap cavity cases, respectively. From these results, the Level 1 mesh (the coarsest mesh) appears to be inadequate to resolve the details of the flow as the results vary greatly from the finer mesh results. Due to the poor results obtained

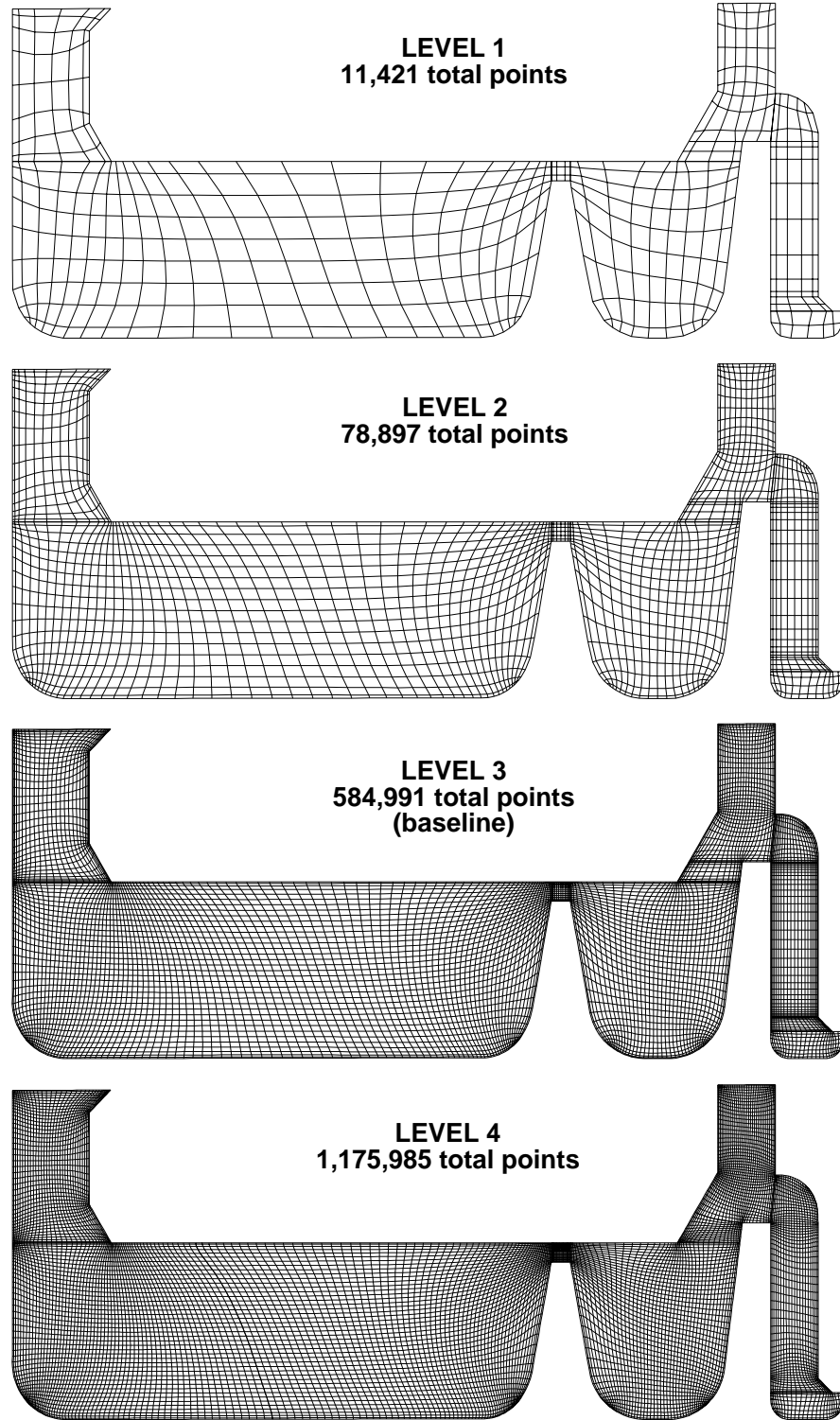


Figure 3.7: Comparison of the four grid resolutions used in the grid study including the total number of grid points in the corresponding 3-D grid with the seal cavity and grid extensions.

with the Level 1 mesh resulting from its coarseness, no other detailed results from that mesh are included in this chapter. Level 2 mesh results begin to capture the behavior of the stator blade. As was seen with the mass flow values, the radial profiles from the Level 3 and Level 4 solutions are very similar.

Spanwise distributions of total pressure, total temperature, and the three velocity components were area-averaged across constant radial grid index planes into the upstream and downstream seal cavity trenches. The comparison of the seal cavity trench flow between different grid resolution levels is shown in Figure 3.10. As was shown in the earlier comparisons of data for the different grid resolutions levels, the Level 1 results are the most outlying and the Level 2 results approach the solutions at Levels 3 and 4. The good agreement between the Levels 3 and 4 results again reinforces the finding that the Level 3 grid resolution is adequate for investigating the seal cavity fluid dynamics. Therefore, it was concluded that Level 3 grid resolution was adequate to identify the detailed characteristics of the coupled stator and seal cavity flow field. Level 2 resolution was used in a limited capacity to provide some basic trends with quicker run times or for cases with extremely large numbers of mesh points (i.e., rotor-stator-rotor cases).

3.7 Rotor-Stator-Rotor Interaction with a Seal Cavity

After evaluating results from the 3-D coupled seal cavity and stator-only grids, the question of whether the influence of the upstream and downstream rotors was being accurately modeled using only stator inlet and exit boundary conditions was raised. Therefore, three-dimensional rotor-stator-rotor steady and unsteady solutions were obtained to determine the inter-blade row flow conditions. The 3-D upstream and downstream rotor grids were constructed using *TIGG3D* such that the rotor grids mated with the stator grid at constant axial and radial positions. The steady solution was obtained using mixing plane coupling between the rotors and the stator grids. This mixing-plane solution appeared to more accurately capture the influence of the rotors on the stator. However, due to the small axial separation of the blades in the rear stages of this compressor, the mixing planes were located extremely close to both the seal cavity inlet and exit and the leading and trailing edges of the respective rotors.

In order to avoid the averaging across the mixing plane so close to the seal cavity openings, a second approach to the rotor-stator-rotor problem was needed. This approach was to perform an unsteady interaction calculation across several blade pitches. The original blade counts of the compressor would have required the modeling of the entire wheel; however, by removing at most two rotor blades and adding only one stator blade, the blade ratio was reduced to 2:3:2 (rotor:stator:rotor). A grid with two rotor blade passages for each rotor wheel and three stator passages was created and was coupled with the full seal cavity grid. Converged time-periodic solutions were obtained on the rotor-stator-rotor grids both with and without the seal cavity

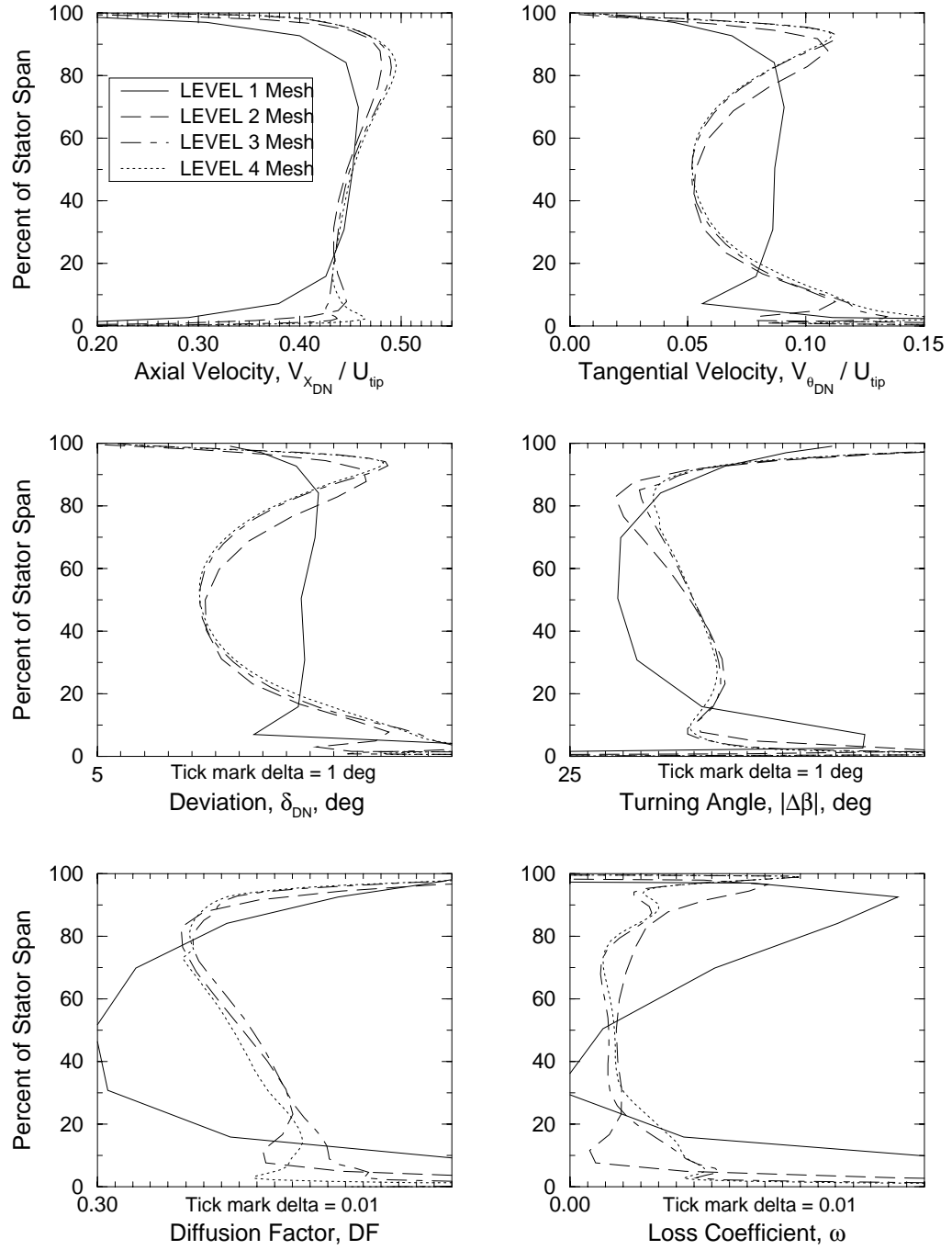


Figure 3.8: Comparison of radial distributions of the stator blade performance between mesh Levels 1, 2, 3, and 4 for the no cavity geometry.

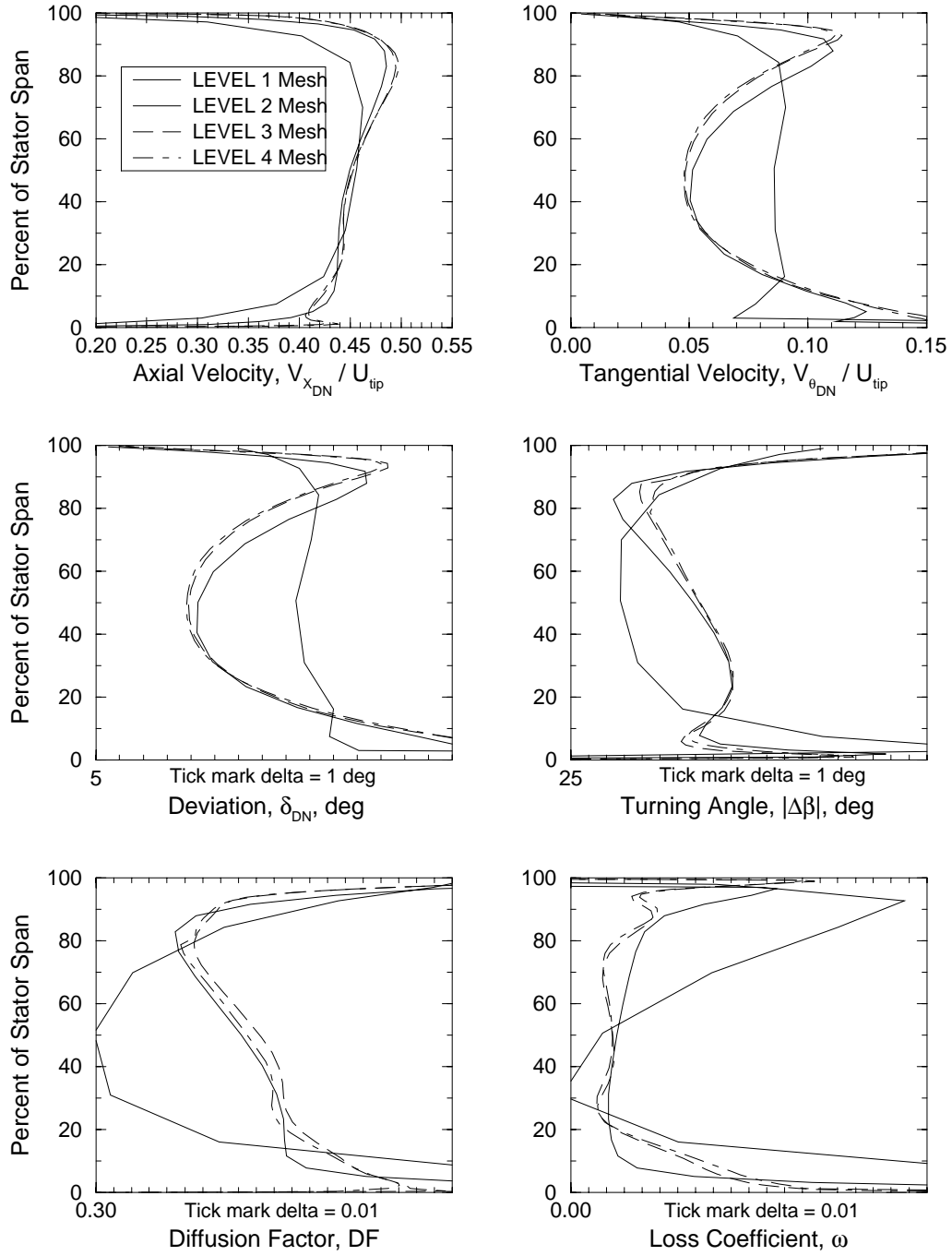


Figure 3.9: Comparison of radial distributions of the stator blade performance between mesh Levels 1, 2, 3, and 4 for the nominal gap seal cavity geometry.

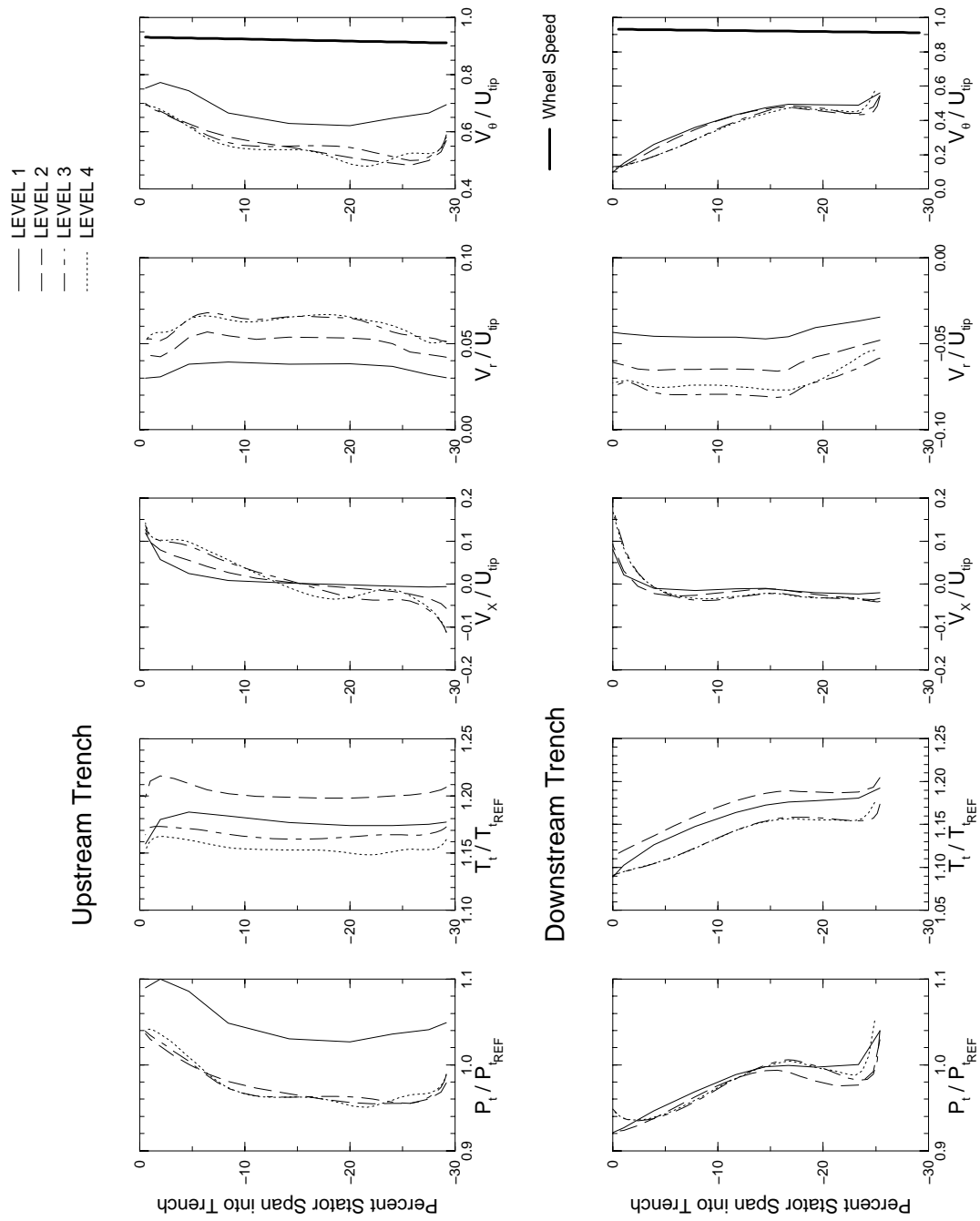


Figure 3.10: Radial distributions of area-averaged flow quantities (across constant radial grid index planes) into the upstream and downstream seal cavity trenches on mesh Levels 1, 2, 3 and 4, for the standard nominal gap seal cavity configuration.

geometry.

The mixing-plane solution was run at grid resolution Level 3 and Level 2, one resolution level coarser. The unsteady solution was not run at the finest level (Level 3) due to the extremely large size of the grid required. This allowed for direct comparison between the unsteady and mixing-plane solutions on the coarse grid level (Level 2). As found in the grid resolution study, results from the unsteady solution on a Level 2 resolution captured the overall trends of the flow character. Another grid was created for the 2:3:2 rotor-stator-rotor geometry without the seal cavity. This grid was identical to the mixing-plane grid being used above except without the geometry of the seal cavity included. A comparison between these two solutions showed the effects of including the detailed seal cavity geometry on the main flow.

In total four different solutions were collected for the high-speed rotor-stator-rotor interaction problem using *ADPAC*. All of the grids listed above were run with identical upstream and downstream boundary conditions for the main flow path (i.e., the same upstream rotor inlet profiles and the same exit static pressure). Three of the solutions include the full 3-D representation of the seal cavity. This combination of solutions allowed for comparisons with respect to the full unsteady vs. mixing-plane approach, grid density, and the inclusion of the seal cavity on the main flow. The four solutions are listed below:

- full unsteady solution on a *coarse* grid (Level 2)
- mixing-plane solution on a *coarse* grid (Level 2)
- mixing-plane solution on a *fine* grid (Level 3)
- mixing-plane solution on a *fine* grid (Level 3) without the seal cavity geometry

3.7.1 Rotor-Stator-Rotor Performance Comparison

Performance data were calculated for each of the four solutions to determine the pressure ratio and efficiency over the rotor-stator-rotor combination. Due to the proprietary nature of the data, only general comparisons are included in this report. All four of the *ADPAC* solutions had a higher mass flow and higher pressure ratio than the design point values; therefore, most of the comparisons are between the different numerical solutions and not with the design point data. This performance discrepancy between the *ADPAC* solutions and the design point can be attributed to raising the exit static pressure from the design point in order to reduce the mass flow in the numerical solutions closer to the design point mass flow. With respect to grid density, the fine meshes had higher mass flows and higher pressure ratios than the coarse meshes at the same back pressure. This might have been in part to the better resolution of the boundary layers and their associated losses similar to the grid resolution study.

When comparing the full unsteady solution with the corresponding mixing-plane solution, the mixing-plane solution had a slightly higher mass flow, pressure ratio, and efficiency. One possible explanation was that the localized losses from the upstream

blade rows were smeared out over the blade pitch and therefore did not create as great of a negative effect on the performance of the downstream blade rows. When the seal cavity was not modeled, there was a corresponding increase in the efficiency. For all the numerical solutions with the seal cavity geometry included, the seal cavity mass flow was slightly more than one-percent of the total mass flow through the main blade passage.

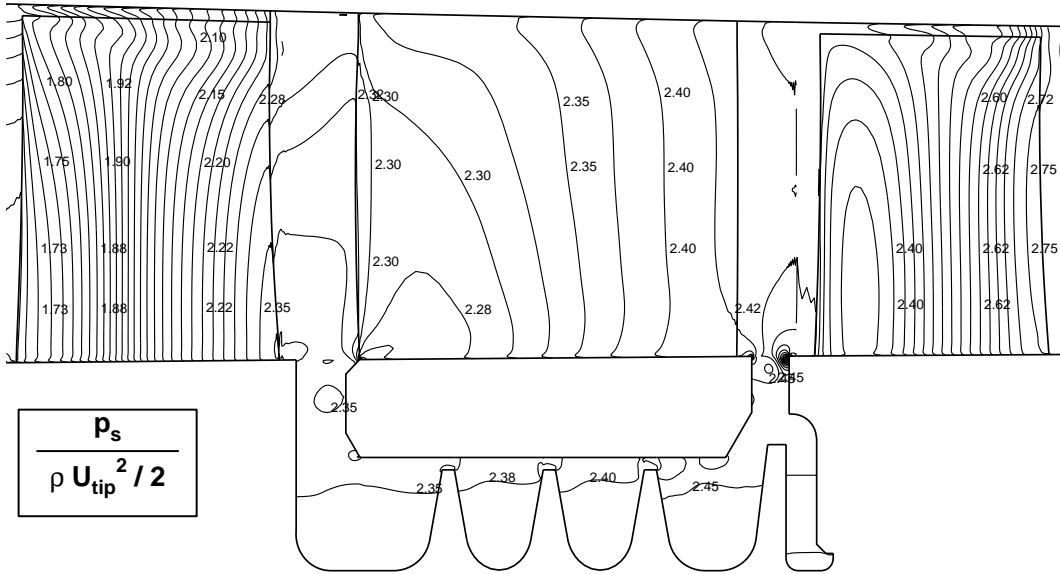
3.7.2 Axisymmetrically-Averaged Solution Comparison

An axisymmetrically-averaged flow file was created for each of the multiple blade solutions. Overall, there were no large differences between the solutions with respect to Mach number distribution and all of the axisymmetric solutions with the seal cavity included show approximately the same flow field. Therefore, detailed contours of the averaged flow field are presented for the fine-mesh mixing-plane solution of the rotor/stator/rotor geometry with the seal cavity. Figure 3.11 shows contours of static pressure and the three velocity components.

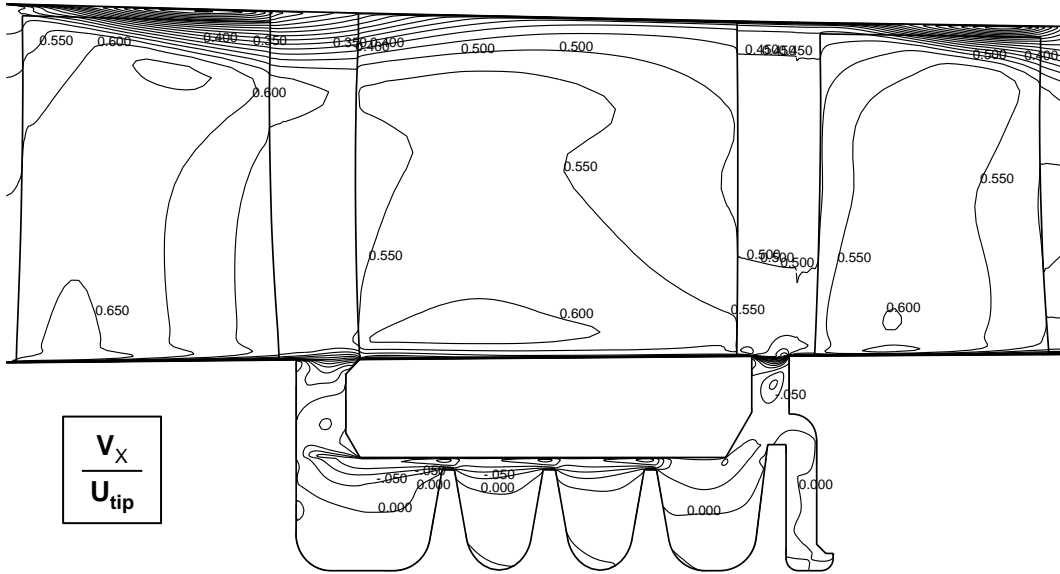
In Figure 3.11a, the static pressure contour levels increase going left to right, as would be expected. It is this increase in pressure across the seal cavity that provides the driving potential to the leakage flow. The axial velocity contours, shown in Figure 3.11b, show the sharp drop and reversal of the leakage flow as it enters the seal cavity passage. The effect of the rotor tip clearance is also visible as a region of reduced axial velocity. The sharp gradients in radial velocity levels, shown in Figure 3.11c, in the region of both the seal cavity trenches illustrates the rotating flow structure in these trenches similar to the classic “driven cavity” problem. The driven cavity-like flow structures are examined in more detail using particle traces later within this report. Changes in tangential velocity are shown in Figure 3.11d. In the main flow path, the tangential velocity increases as it passes through the upstream rotor, the stator then turns the flow back more axially decreasing the tangential component, and the downstream rotor again adds to the tangential component. However, of particular interest to this study is the variations of tangential velocity through the seal cavity. The leakage flow enters the seal cavity downstream of the stator at approximately zero tangential velocity and is spun up to a high tangential velocity level before being injected back into the main flow. This interaction between the “injected” leakage flow into the main stator flow field will be investigated in further detail later in this report.

3.7.3 Detailed Near-Hub Flow Field Comparison

In order to better understand the behavior of the flow near the hub surface, a more detailed analysis is presented below. Using cylindrical velocities and flow angles, the flow field was examined at the first computational cell away from the hub surface. This physical distance corresponded to 0.42% of the stator blade span for the coarse grids (Level 2). Using these near-hub surface distributions, comparisons were made with respect to unsteady vs. mixing-plane, grid density, and the inclusion of the seal cavity geometry.

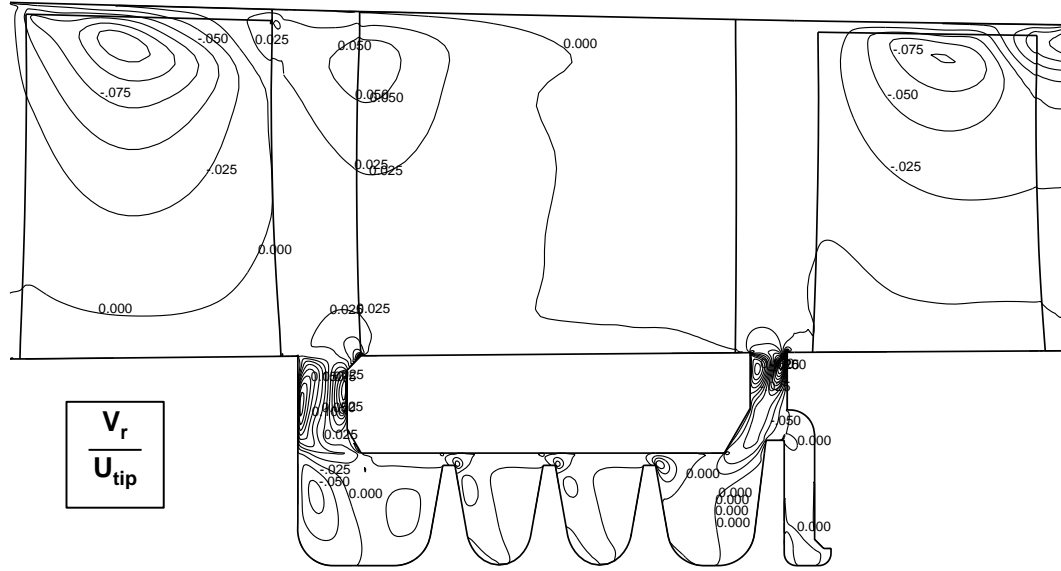


a. Static Pressure Contours

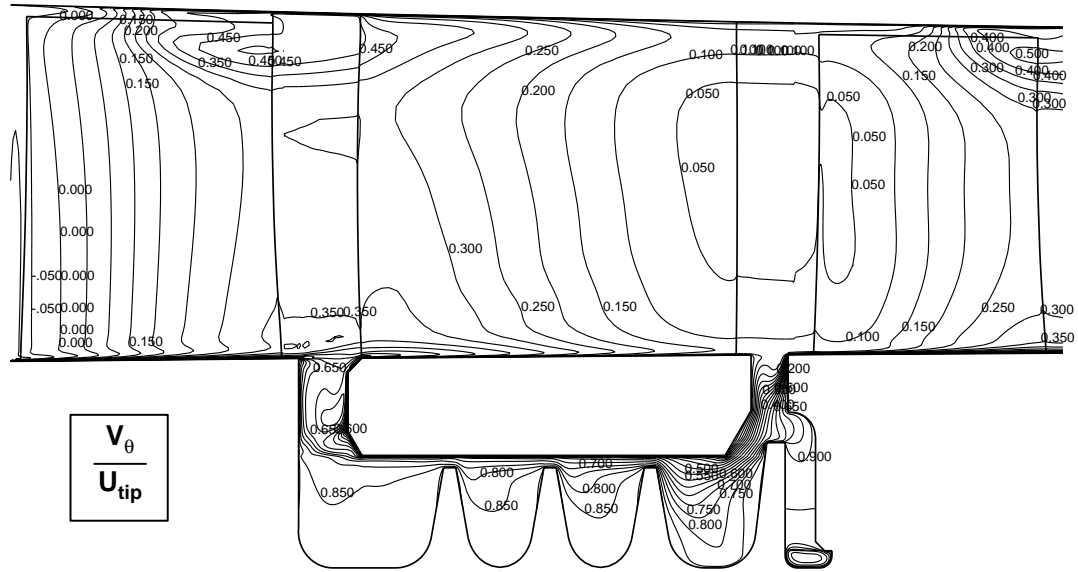


b. Axial Velocity Contours

Figure 3.11: Contours of static pressure and axial velocity taken from the axisymmetrically-averaged *ADPAC* fine-mesh mixing-plane solution of the rotor/stator/rotor geometry with the seal cavity.



c. Radial Velocity Contours



d. Tangential Velocity Contours

Figure 3.11: Contours of radial velocity and tangential velocity taken from the axisymmetrically-averaged *ADPAC* fine-mesh mixing-plane solution of the rotor/stator/rotor geometry with the seal cavity.

The comparison of radial velocity distributions between the full unsteady solution and the mixing-plane solution is shown in Figure 3.12. The contours for the unsteady solution were taken from a single point in time and not from a time-averaged solution; this allows for sharper contrast between the unsteady and the mixing-plane solutions. In the unsteady solution shown in Figure 3.12a, the radial velocity field in the upstream cavity gap, where the flow had a mostly positive radial velocity, appears to be somewhat constant in the circumferential direction with respect to axial location and not tied to the upstream rotors except possibly in small regions where the effect of the rotor wake can be seen. However, in the downstream cavity gap, where the flow enters the cavity, the negative radial flow regions were strongly tied to the rotor leading edge. This *pumping* action into the seal cavity was the influence of the rotor blade blockage on the main flow driving the flow into the cavity. Compared with the mixing-plane solution in Figure 3.12b, the upstream cavity gap distribution appeared to be similar to the unsteady solution; however, the influence of the downstream rotor, which had been smeared out by the mixing plane, did not show the strong relation between the rotor leading edge and the local regions of negative radial velocity.

The effect of modeling the seal cavity on the near-hub region was very significant, as was expected. Without the cavity, the flow along the hub traveled with almost no radial velocity; whereas, with the seal cavity included the radial velocity distribution near the hub was greatly affected primarily in the region near the seal cavity trenches. One of the conclusions of this comparison was that the mixing-plane approximation had a greater influence on the downstream seal cavity gap than the upstream gap. Also, the inclusion of the seal cavity geometry, as expected, has a very strong influence on the near-hub region of the flow.

3.7.4 Spanwise Profile Comparison

The multiple blade row *ADPAC* solutions without the cavity included were area-averaged axisymmetrically. Spanwise distributions were extracted from both the fine mesh and the coarse mesh solutions that used the mixing-plane approximation at four inter-blade stations. The axial locations of the inter-blade stations, shown in Figure 3.13, with respect to the rotor and stator blades were selected as the axial grid line that was closest to the hub midpoint between the two blades. Spanwise comparisons were made between the numerical solutions for the following four flow quantities: total pressure (p_t), total temperature (T_t), axial velocity (V_X), and tangential velocity (V_θ).

The series of spanwise plots is shown in Figures 3.14 to 3.17. The two *ADPAC* solutions are represented by solid lines with small symbols located at the grid data points. The *ADPAC* solutions matched the design data throughout the three blade rows with the fine mesh results matching closer than those from the coarser mesh, as was expected. Efforts were focused on examining the upstream rotor blade in isolation in order to assure the inlet flow to the stator blade row with the seal cavity was correctly specified.

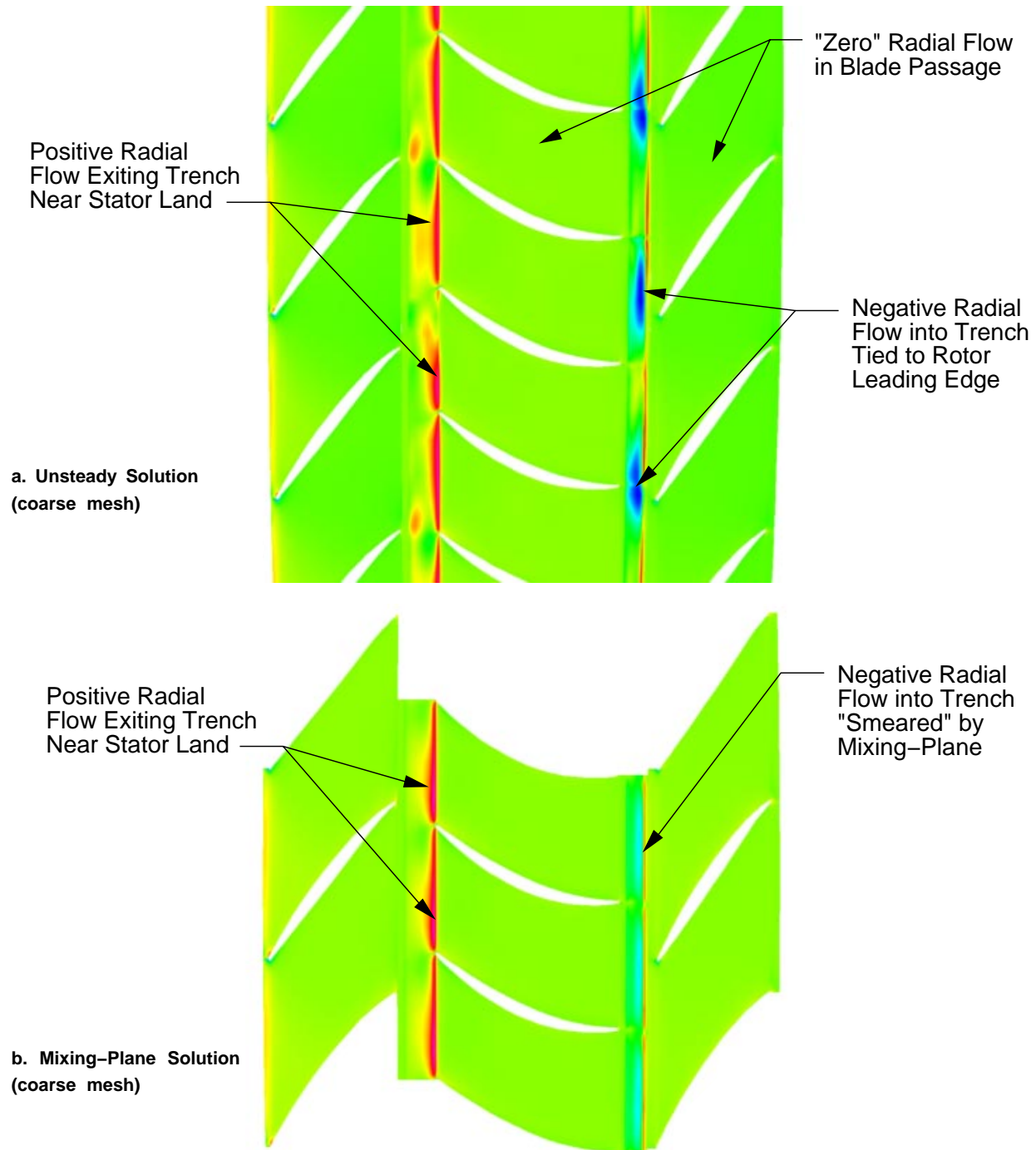


Figure 3.12: Contours of radial velocity located one computational cell above the hub surface for the two coarse-mesh (Level 2) rotor-stator-rotor *ADPAC* solutions.

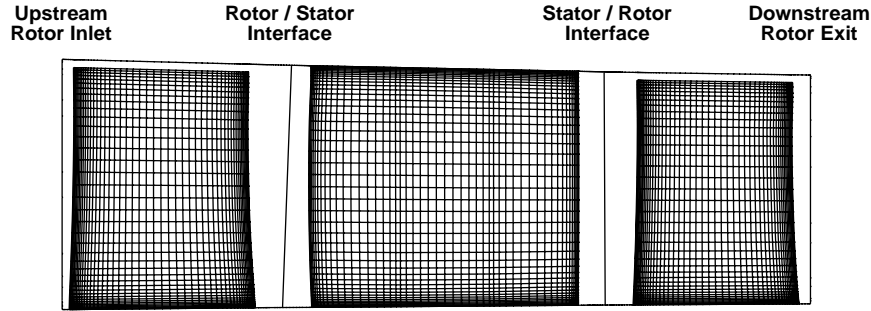


Figure 3.13: Axial location of spanwise profile stations between the rotor and stator blades.

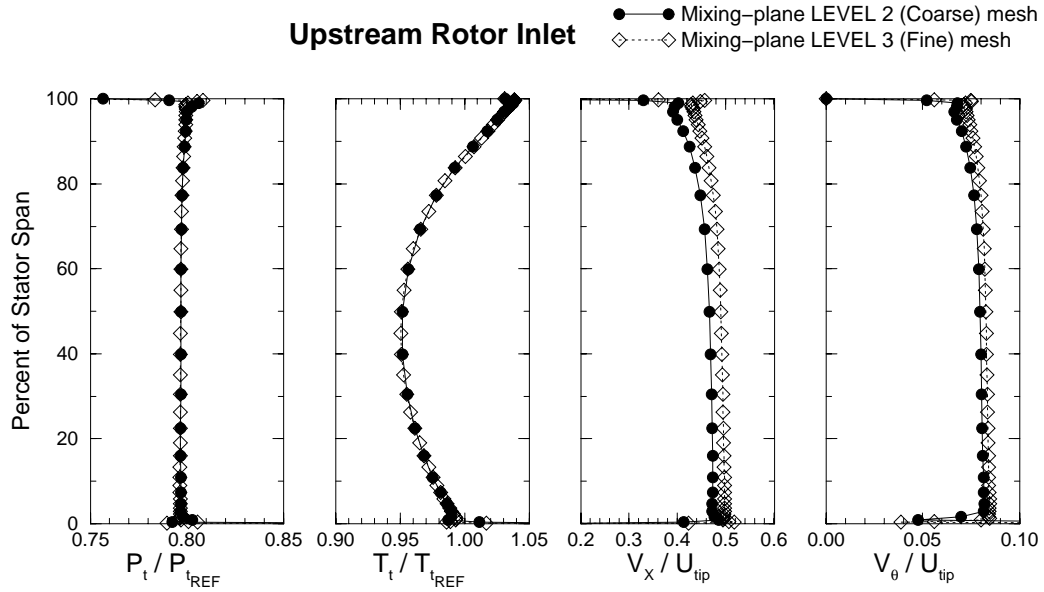


Figure 3.14: Spanwise profiles of total pressure, total temperature, axial velocity, and tangential velocity at the upstream rotor inlet.

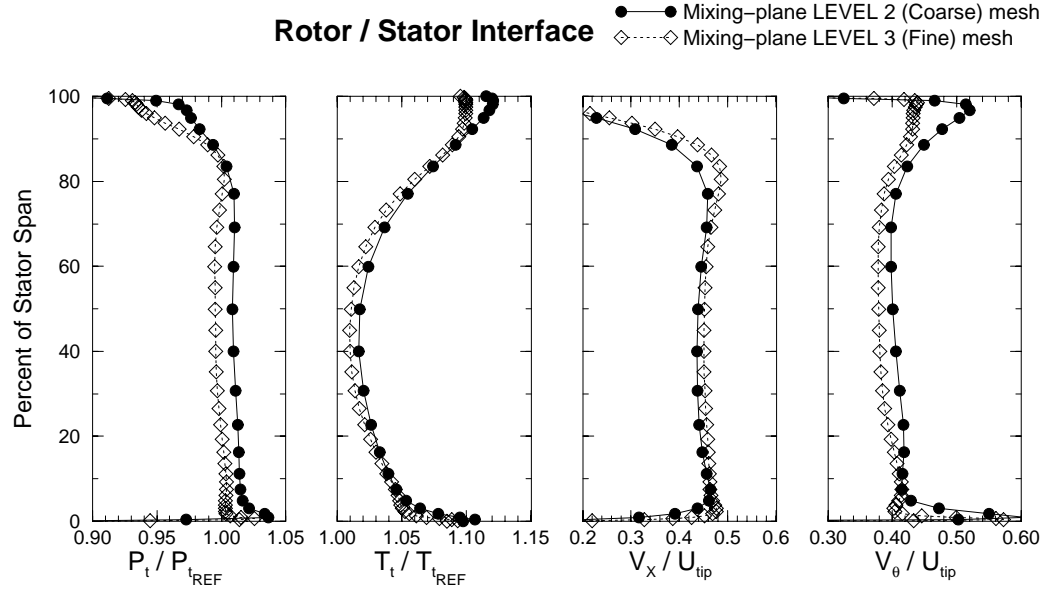


Figure 3.15: Spanwise profiles of total pressure, total temperature, axial velocity, and tangential velocity at the upstream rotor / stator interface.

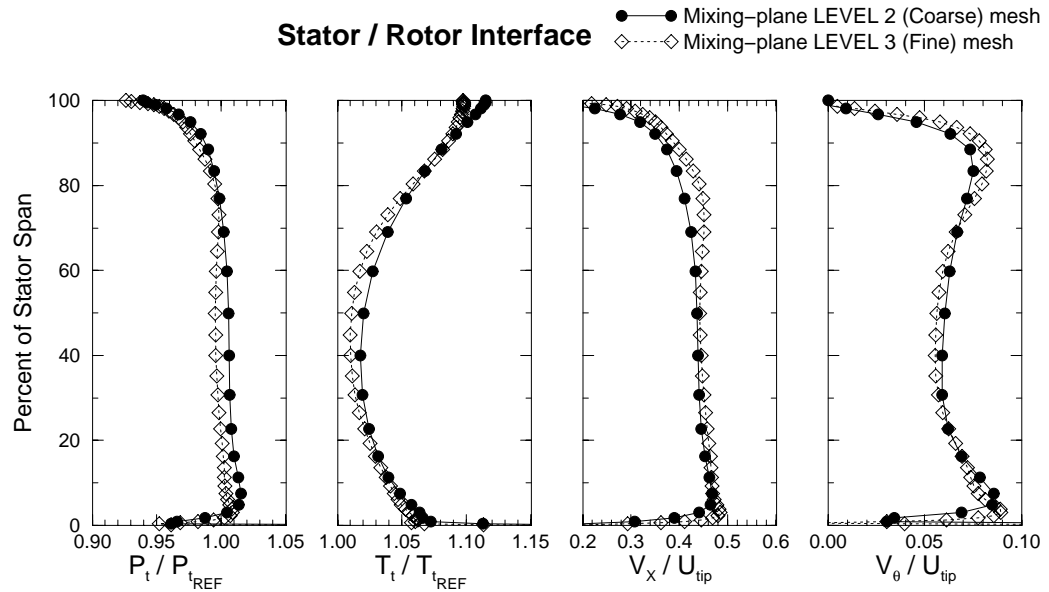


Figure 3.16: Spanwise profiles of total pressure, total temperature, axial velocity, and tangential velocity at the stator / downstream rotor interface.

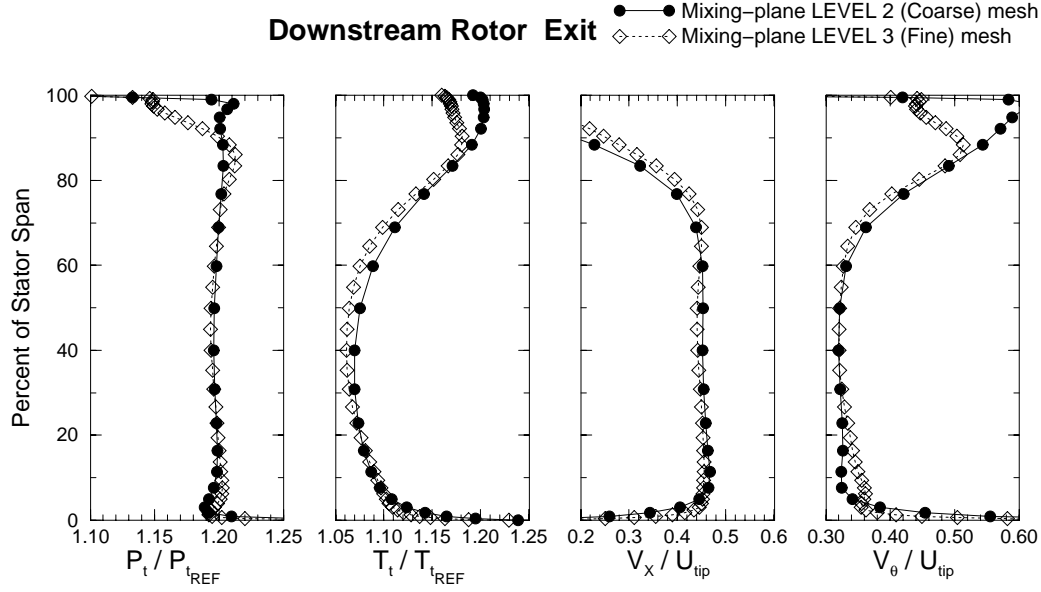


Figure 3.17: Spanwise profiles of total pressure, total temperature, axial velocity, and tangential velocity at the downstream rotor exit.

3.8 Isolated Upstream Rotor Study

In addition to the concern about inlet boundary conditions for the upstream rotor, the location of the inlet boundary was also a concern. For the rotor-stator-rotor solutions obtained, the upstream boundary of the first rotor was located extremely close to the rotor leading edge as shown in Figure 3.13. Grid extension blocks were added to the isolated rotor grid which moved the upstream and downstream boundaries away from the blades by approximately one blade axial chord. A blade-to-blade view of the hub surface from the isolated rotor fine mesh with the grid block extensions is shown in Figure 3.18. The grid extensions were rotated to match the trailing edge angle and better resolve the rotor wake.

A detailed study of the effect of inlet profile on the upstream rotor performance was completed in order to obtain a representative inlet condition for the stator blade row with the seal cavity. A series of four different inlet total pressure profiles were tested with the isolated upstream rotor mesh with the grid extensions. The four profiles are shown in Figure 3.19 and are described below:

Inlet Profile A - a quasi-constant pressure profile generated from the design data without accounting for any endwall blockage,

Inlet Profile B - a turbulent boundary layer profile generated by using the 1/7th-power law for the boundary layer shape to account for blockage,

Inlet Profile C - a profile taken from the exit of the stator in previous *ADPAC* solutions and scaled back to match the appropriate freestream total pressure

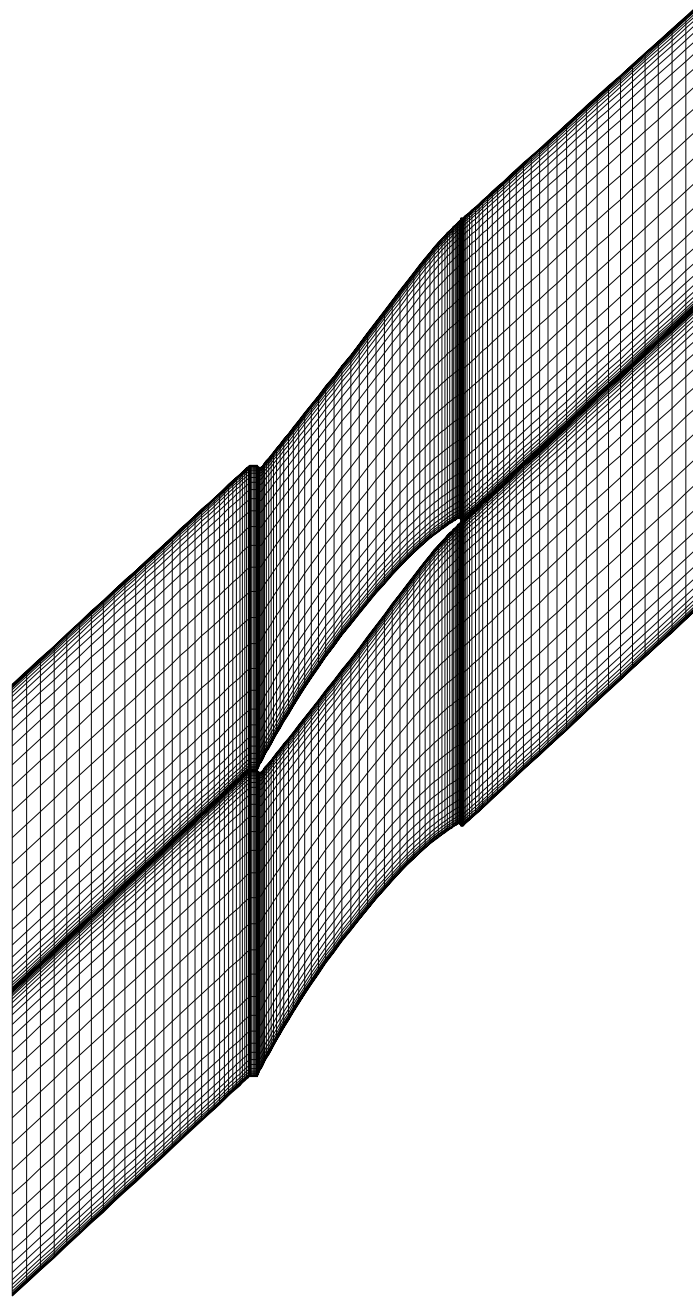


Figure 3.18: Grid distribution at the hub surface from the isolated upstream rotor grid with the grid block extensions. (Grid has been copied one rotor blade pitch to clarify blade shape.)

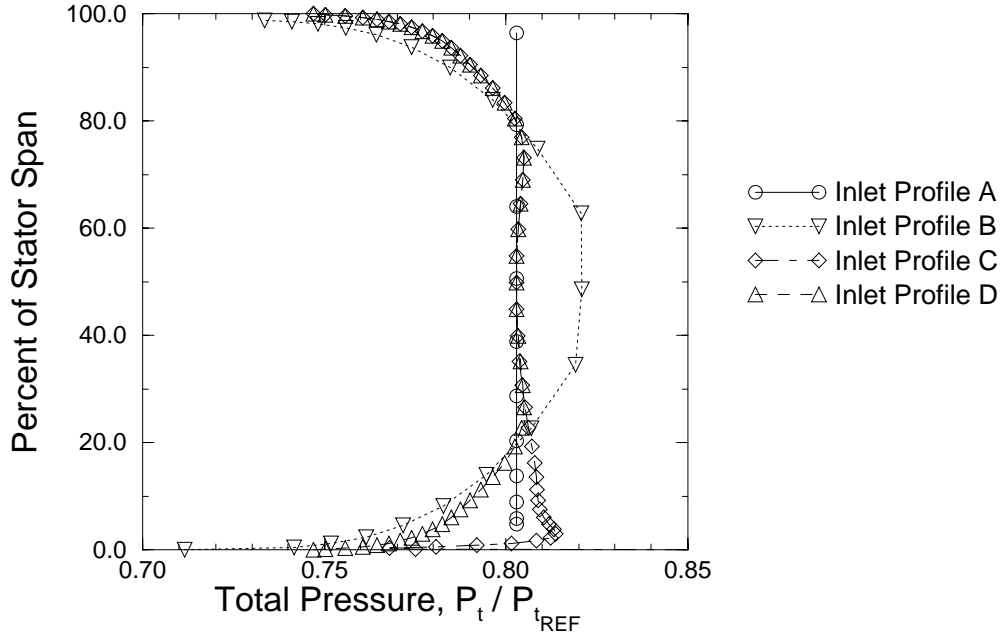


Figure 3.19: Inlet total pressure profiles tested with the isolated upstream rotor.

(similar to a repeating stage assumption),

Inlet Profile D - a profile generated by reflecting the upper 50% span of Inlet Profile C about the centerline to obtain equal blockage at hub and tip.

Several runs were performed using the different inlet profiles listed above over a range of rotor back pressures. After each run, it was determined whether the *ADPAC* solution was a valid converged point or whether the rotor solution was “stalled”. The series of converged solution points for each of the inlet profiles generated a speed line for each profile shown in comparison with the design point in Figure 3.20.

Only two of the inlet profiles (A and C) generated multiple converged points. Inlet Profile B, derived from the turbulent boundary layer theory, resulted in no converged point over the range of back pressures tested. Inlet Profile D was tested with viscous and inviscid walls on the grid extensions; however, only one converged point was found for each of these two cases. The difficulty in gathering converged points for some of the inlet profiles was directly related to the amount of blockage simulated by the profile; the profiles ordered by increasing blockage (A, C, D, B) corresponded to the increasing difficulty in obtaining converged solutions. The effect of increased blockage from Inlet Profile A to Inlet Profile C is shown in a decrease of mass flow and a decrease in efficiency. The speed line from the Inlet Profile C solutions passed closer to the design point than the speed line from the Inlet Profile A solutions. This showed that when no blockage was accounted for, as with Inlet Profile A, the converged solution overflowed.

By selecting points matching the design pressure ratio (solid symbols in Fig-

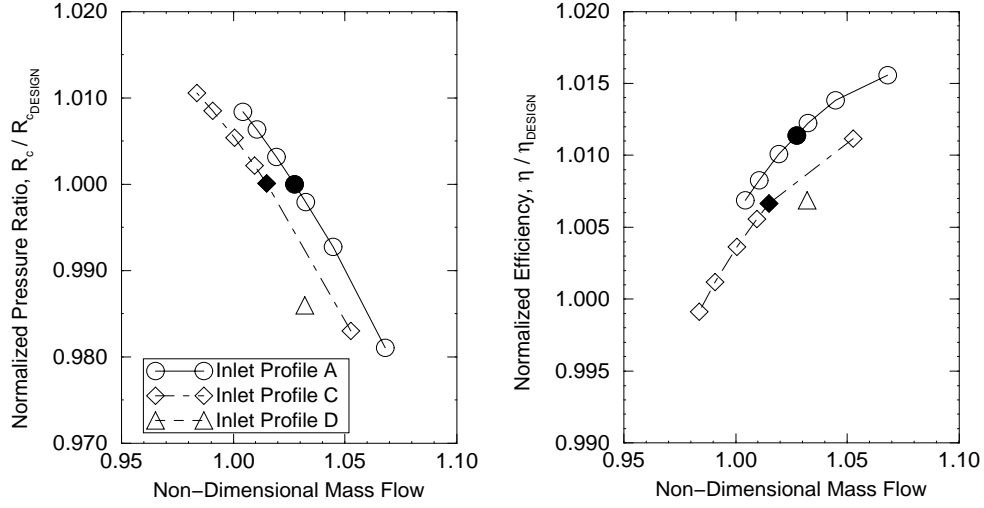


Figure 3.20: Pressure ratio and efficiency speed lines for the upstream rotor at 100% rotation speed for the range of inlet profiles tested. (Note: The solid symbols represent cases to be compared later within the chapter.)

ure 3.20), a comparison of the rotor performance was made. Spanwise profiles of pressure ratio, efficiency, and diffusion factor, shown in Figure 3.21, were calculated for the two *ADPAC* solutions. The small variation in spanwise pressure ratio between the Inlet Profile A case and the Inlet Profile C case was related to the redistribution of total pressure entering the rotor blade from the tip to the hub. This had the effect of reducing the pressure ratio at the hub and increasing the pressure ratio at the tip for the Inlet Profile C case. The Inlet Profile C case appeared to capture the reduction in efficiency of the design data from midspan to the endwall region better than the Inlet Profile A case. Both profile solutions appeared to match the design diffusion factor distributions equally well. As mentioned earlier, the objective of analyzing the isolated rotor was to obtain a satisfactory exit profile to feed into the isolated stator solutions. The exit profiles of total pressure, total temperature, axial velocity, and tangential velocity magnitude for Inlet Profiles A and C are shown in Figure 3.22.

From the data presented above for all the inlet profile cases, the inlet profile which most closely matched the design operating point for the rotor was Inlet Profile C; this was the profile generated by scaling the profile shape coming out of the stator. The exit profile obtained from the Inlet Profile C solution was used as inlet conditions for the initial isolated stator calculations. The increase in blockage from Inlet Profile A to Inlet Profile C appeared to be adjusting the solutions in the proper direction. However, since Inlet Profile C was taken from a solution without the stator inner-band seal cavity, additional modifications were necessary near the hub region of the inlet profile to account for the effects of the inner-banded stator seal cavity. The current upstream rotor exit profile was used as the inlet profile to calculate flow through the stator with the seal cavity. The resulting stator exit profile including the seal cavity effects was then scaled and used to re-evaluate the upstream rotor performance.

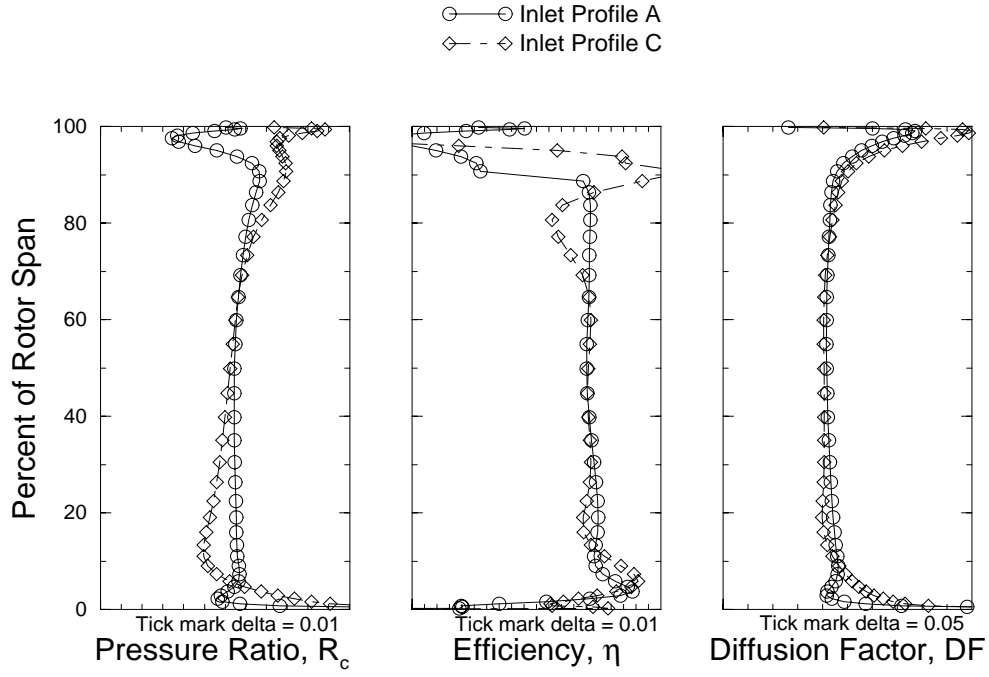


Figure 3.21: Spanwise profiles of the upstream rotor blade performance for Inlet Profiles A and C.

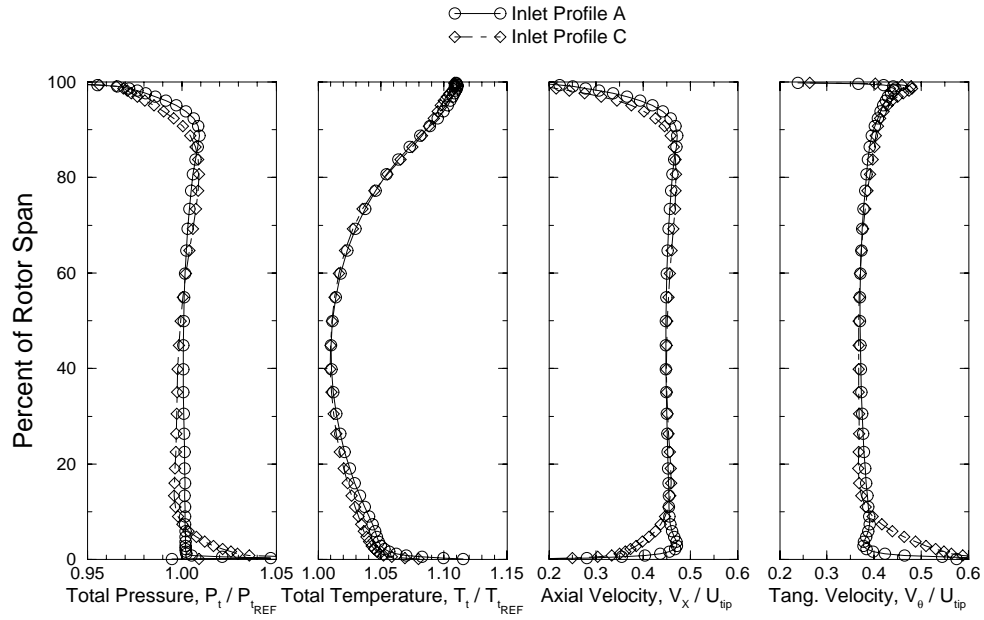


Figure 3.22: Spanwise profiles of the upstream rotor exit flow for Inlet Profiles A and C.

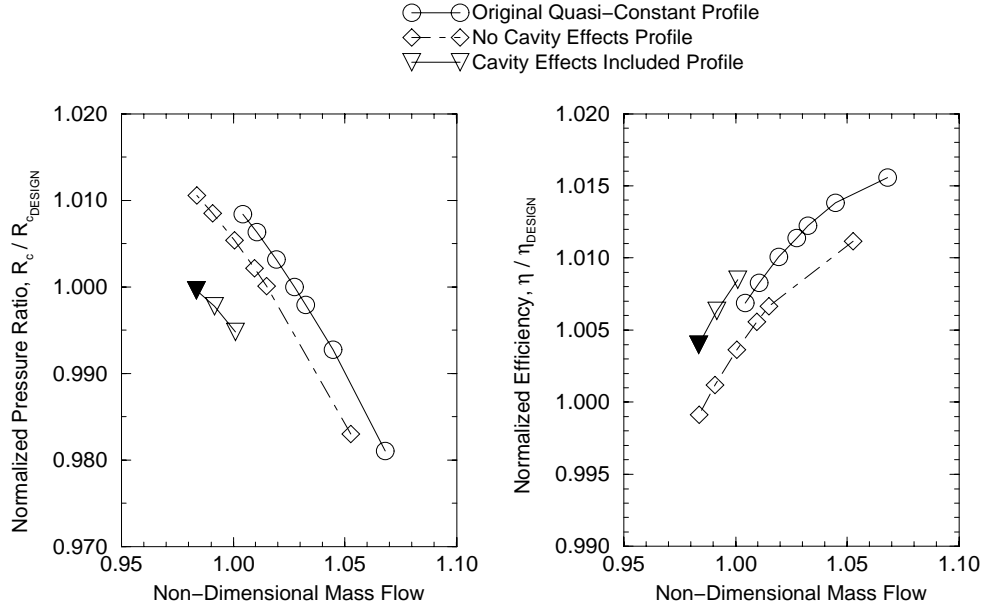


Figure 3.23: Pressure ratio and efficiency 100% constant speed lines for the upstream rotor using the scaled stator profile with cavity effects compared with other inlet profiles tested. (Note: The solid symbols represent cases to be compared later within the chapter.)

3.8.1 Upstream Rotor Performance Re-evaluation

Using the stator exit profile including cavity flow effects, the upstream rotor performance was re-evaluated. The rotor solutions were again collected over a range of back pressures in order to determine the point closest to the design point. This series of points is shown as a 100% constant speed line in Figure 3.23 (represented by inverted triangles). For comparison, the figure also contains the results obtained previously, shown in Figure 3.20, which include the original quasi-constant profile (Profile A) results (represented by circles), and the previous scaled stator exit profile without the cavity effects (Profile C) results (represented by diamonds). By using the mass-averaged profile including the cavity effects, the additional blockage created by the recirculating seal cavity flow has reduced the overall mass flow for the speedline approximately 1.5% from the design point.

The corresponding performance data at the point nearest the design pressure ratio is shown in Figure 3.24. The data include spanwise distributions of pressure ratio, efficiency, and diffusion factor. The *ADPAC* solution matched the design data well as far as the pressure ratio and diffusion factor, but it was slightly off in predicting the efficiency distribution shape; however, this predicted rotor performance obtained from using the most recent scaled stator exit profile appeared to match the design data as well as any of the previous solutions. Since the apparent effect of the upstream stator blade row including the inner-banded seal cavity flow effects had been accounted for

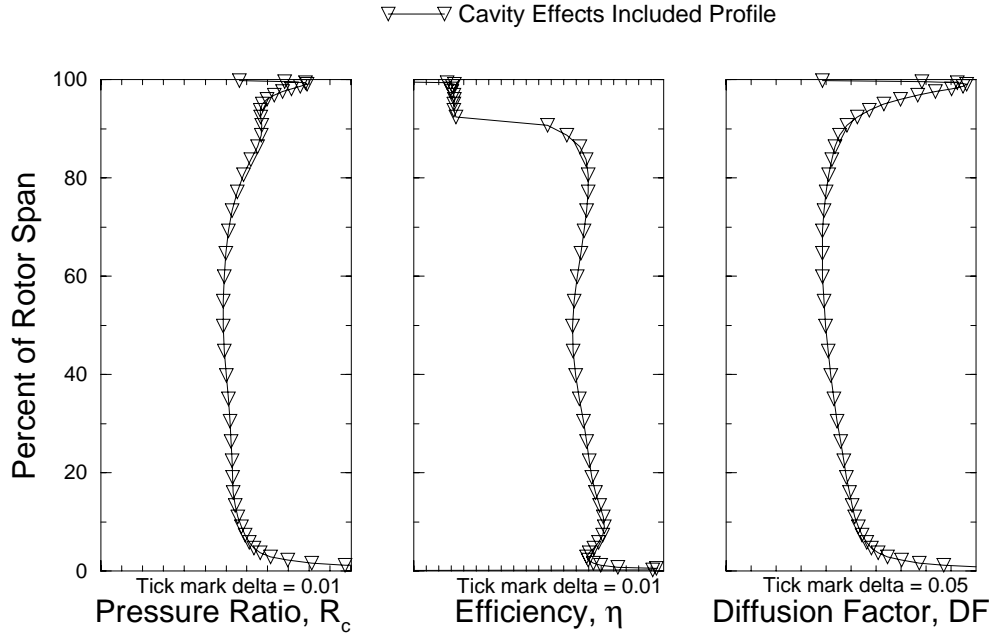


Figure 3.24: Spanwise profiles of the upstream rotor blade performance using the scaled stator exit profile that included the seal cavity effects.

in this rotor calculation, the exit profiles, shown in Figure 3.25, obtained from this solution were representative of the flow entering the stator blade row with the seal cavity and were used to create the new inlet boundary conditions to the stator.

3.9 Isolated Stator Analysis

Using the “re-evaluated” inlet profile obtained from the exit of the upstream rotor, solutions of the isolated stator were collected for a total of four different seal cavity configurations shown in Figure 3.26. In order to determine whether differences between the solutions with and without the seal cavity were due to the presence of the seal cavity or just a result of small run-to-run variations, two additional seal cavity geometries were generated by modifying the nominal gap single-knife seal cavity geometry. The first modification was to increase the nominal gap between the single-knife seal and the stator inner-band as shown in Figure 3.27. This resulted in a slight increase in mass flow recirculating through the seal cavity. The second geometry modification to the existing grid was to remove the knife seal entirely from the seal cavity as shown in Figure 3.28. Without any type of obstruction in the seal cavity, large amounts of mass flow recirculated around the stator land. By testing four geometric configurations, the significance of the differences between the solutions and the trends of the data were easier to interpret.

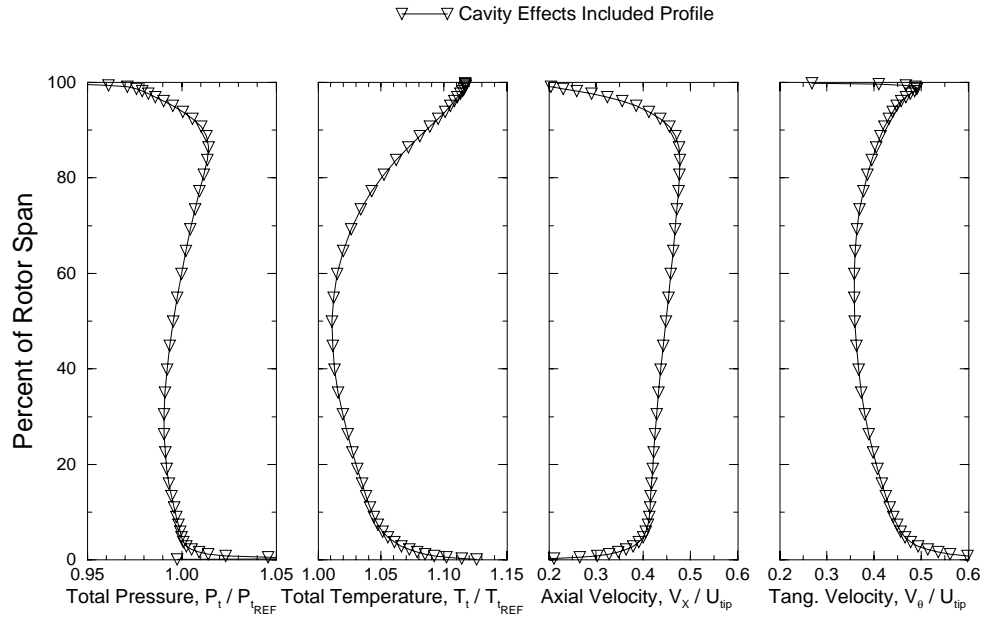


Figure 3.25: Spanwise profiles of the upstream rotor exit flow used as inlet conditions for the stator.

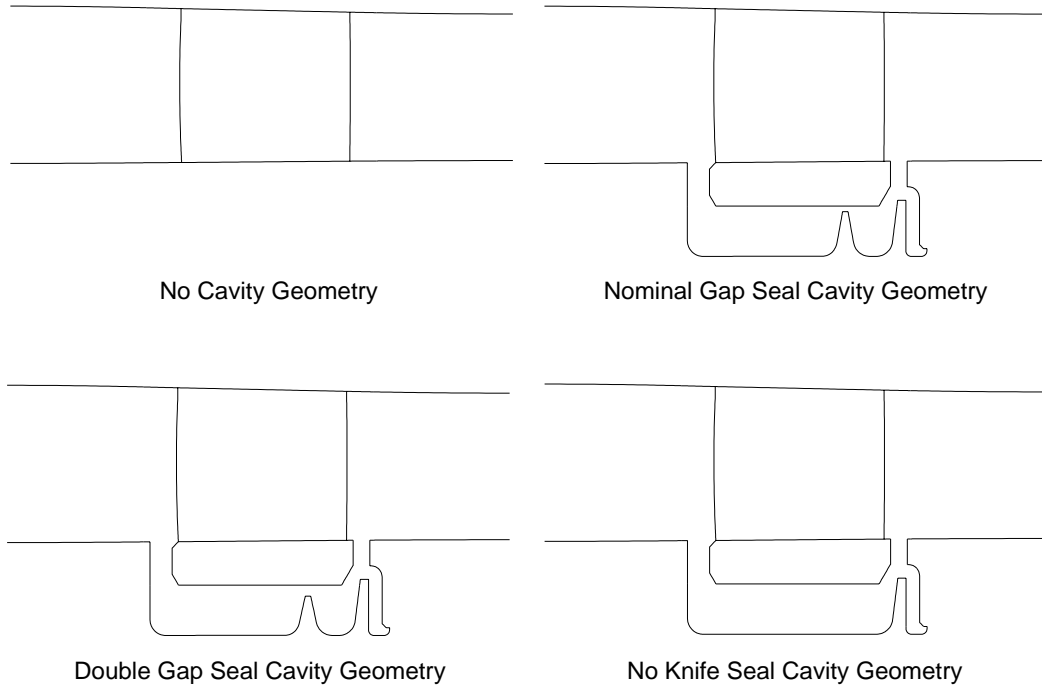


Figure 3.26: Axisymmetric outlines of the stator flow path and the four various seal cavity geometries tested.

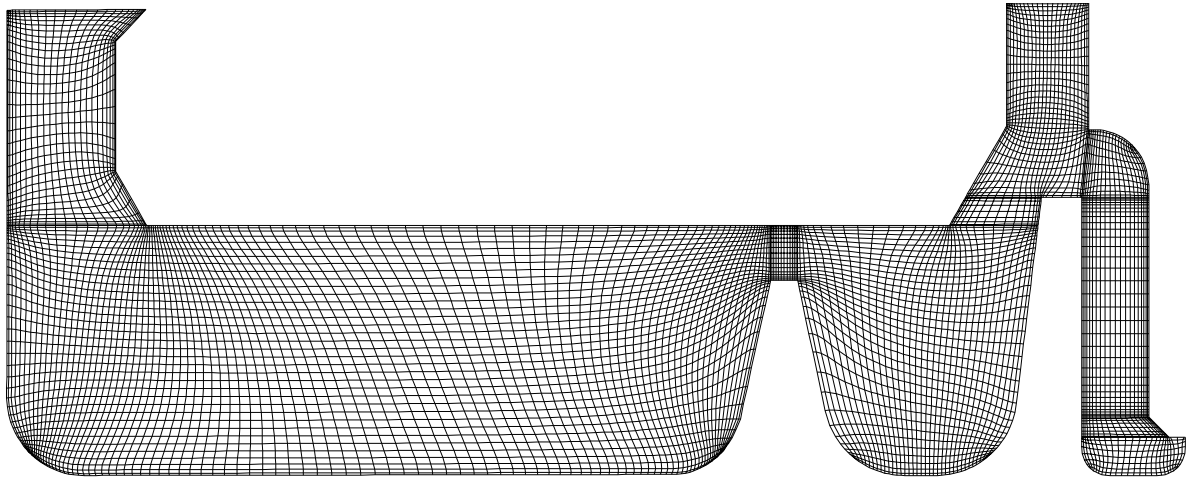


Figure 3.27: Axisymmetric slice of the single-knife seal cavity grid (Level 3 grid resolution) with the knife seal clearance gap doubled radially.

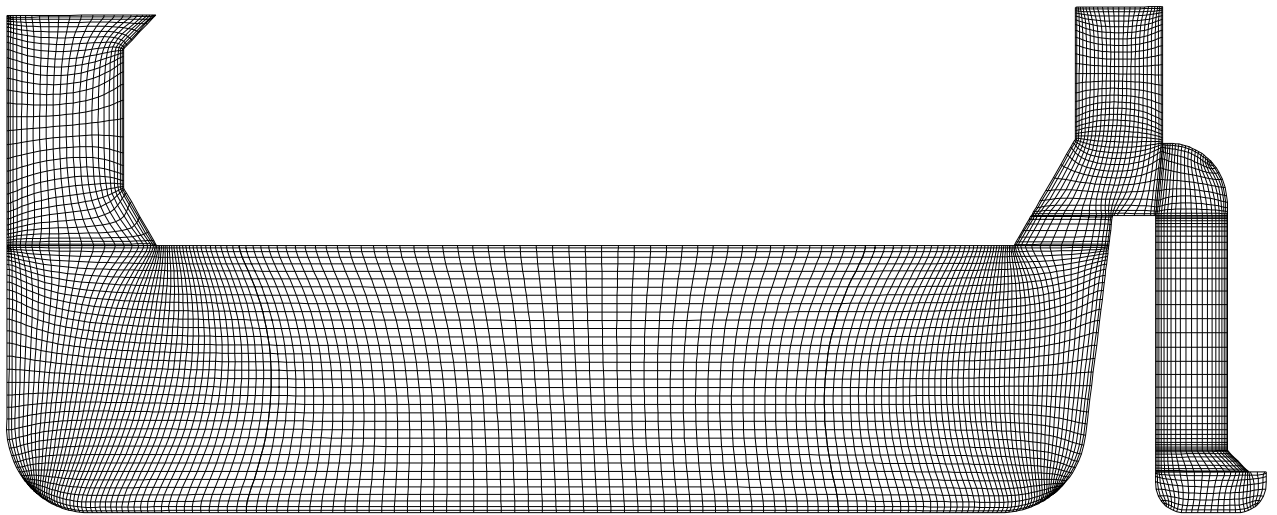


Figure 3.28: Axisymmetric slice of the seal cavity without any knife seals (Level 3 grid resolution)

Seal Cavity Configuration	Stator Passage Mass Flow (normalized by No Cavity value)	Seal Cavity Mass Flow (as % of stator mass flow)
No Cavity	1.000	0.00%
With Cavity (Nominal Gap)	1.004	1.74%
With Cavity (Double Gap)	1.009	2.50%
With Cavity (No Knife)	0.997	3.56%

Table 3.2: Mass flow rates through the stator blade passage and the cavity passage for the four different seal cavity configurations.

3.9.1 Isolated Stator Results

Detailed results from the different seal cavity configuration on the grid resolution Level 3 are compared below with respect to mass flows and radial distributions of flow variables and performance parameters. Several different flow quantities were plotted including radial spanwise distributions of axial velocity, tangential velocity, and flow angle at the four measuring stations (UP, LE, TE, and DN), referred to in Figure 3.6, and distributions of incidence, deviation, turning angle, diffusion factor, and loss coefficient. As noted in the data reduction section, the stator blade performance distributions were calculated across the UP measuring station and the DN measuring station.

Mass flows through the main stator blade flow path and the seal cavity flow path, shown in Table 3.2, were calculated for each of the four cavity geometry configurations. For approximately the same amount of mass flow in the main flow path, the increase in seal cavity mass flow with increasing seal tooth gap was significant. In addition to affecting the mass flow through the seal cavity, the inclusion of the seal cavity and the changes within the seal cavity also showed an effect on the stator blade performance, especially near the hub region.

Figures 3.29, 3.30, and 3.31 show the radial distributions of flow variables and stator blade performance parameters described above. The effect of the recirculating flow about the stator land can be seen in the axial velocity distributions shown in Figure 3.29. The axial velocity distributions at the upstream measuring station showed a slightly increasing deficit near the hub region as the seal cavity flow was increased causing additional blockage near the hub. At the leading edge, the added flow coming out of the seal cavity was seen as an increase in axial velocity near the hub region. This increase became somewhat mixed out by the trailing edge, and at the downstream measuring station the profiles including the seal cavity geometry showed a larger deficit from the mass leaving the main flow path and entering the seal cavity. In order to maintain the same mass flow through the stator when the

seal cavity geometry was included, the axial velocity profiles adjusted by accelerating the flow slightly in the upper 80% span to account for the blockage in the lower 20% span region. The incoming tangential velocity remained mostly unchanged at the upstream measuring station; however, after the flow was injected through the seal cavity gap the lower 20% showed an increase in tangential velocity. Through the stator blade row the tangential velocities showed some redistribution from the no cavity configuration. The no knife configuration shows a much larger departure from the other solutions.

Due to the realignment of the axial and tangential velocities, the flow angle distributions became slightly readjusted from the no cavity case as shown in Figure 3.30. The change in incidence to the stator blade from upstream of the seal cavity gap to the leading edge was most prominent from 10% to 60% span. As more flow was allowed to pass through the seal cavity, the change in incidence from the no cavity solution also increased. A corresponding influence of the downstream seal cavity gap on the deviation angle was not as apparent as the upstream cavity gap's influence on the incidence angle.

Figure 3.31 contains four performance parameters measured across the stator blade using the upstream and downstream measuring stations. As the seal cavity flow was increased, the loading on the blade also increased as shown in the diffusion factor, especially near the hub region; however, as mentioned above, there was a transition point when the seal tooth was completely removed, and the flow field character changed significantly. This significant change in the progression of the solutions was seen in all four performance parameters, especially in the diffusion factor distribution. This “unloading” of the blade with a crossover near the hub region agreed with the data trends found experimentally in the Low-Speed Axial Compressor when the seal tooth was set to maximum leakage [9].

The effect of the seal cavity mass flow on the loss coefficient was seen near the hub. The lower 10% of the stator span showed an increase in loss coefficient with increasing seal cavity flow. Between 10% span and 40% span the loss coefficient decreased initially with increasing seal cavity flow and then increased sharply when the seal tooth was removed. The effect on the loss parameter was very similar to the loss coefficient.

Radial distributions of total pressure, total temperature, and the three velocity components were area-averaged across constant grid index planes into the upstream and downstream seal cavity trenches. Figure 3.32 presents trench profiles for the three seal cavity configurations. In almost all cases, the double gap cavity results lie between the nominal gap results and the no knife results. The greatest percentage variation between the three configurations appears in the radial velocity profiles. As expected, when the seal tooth gap was enlarged allowing more mass to pass through the cavity, the absolute value of the radial velocity increased in magnitude (the negative sign on the radial velocity at the downstream trench indicates flow into the cavity). From the tangential velocity distributions, it appeared that the average cavity flow quickly reached most of its final value within the first 15% of the stator span into the trench. Also, as the mass flow through the cavity increased, the influence of the constant tangential wheel speed decreased. This variation in upstream trench exit swirl velocity

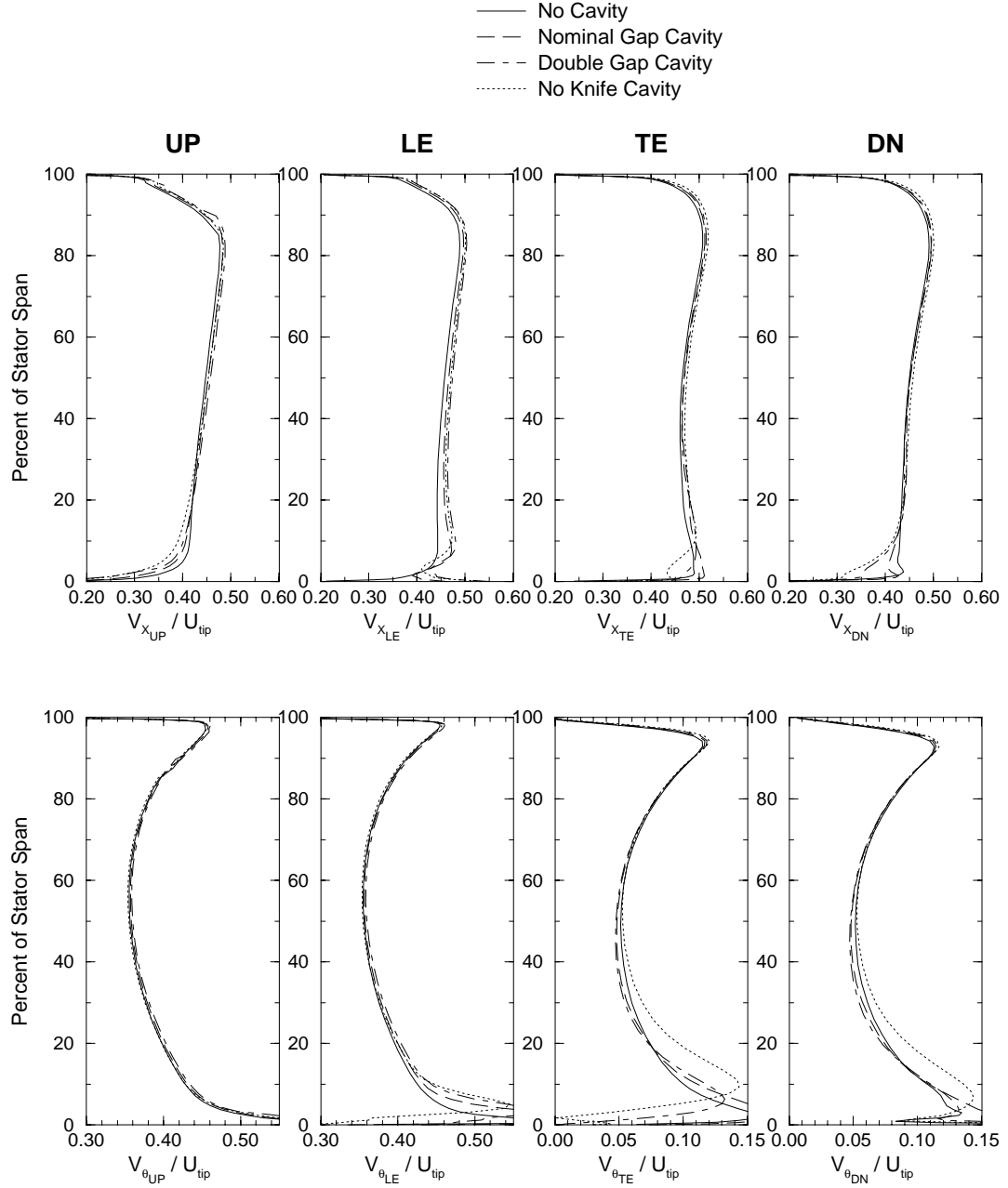


Figure 3.29: Radial distributions of axial and tangential velocities from the four measuring stations through the stator.

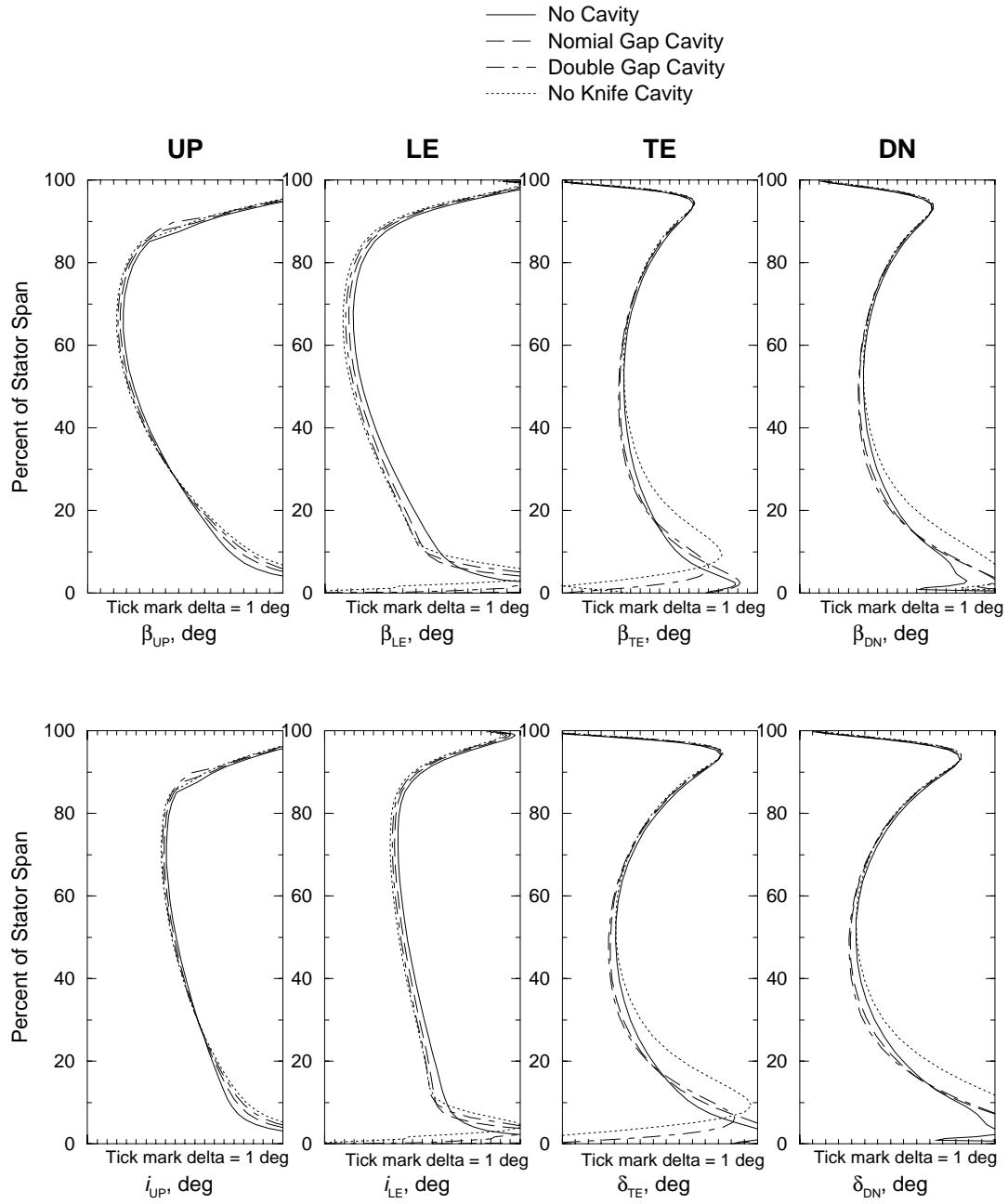


Figure 3.30: Radial distributions of flow angles, incidence, and deviation from the four measuring stations through the stator.

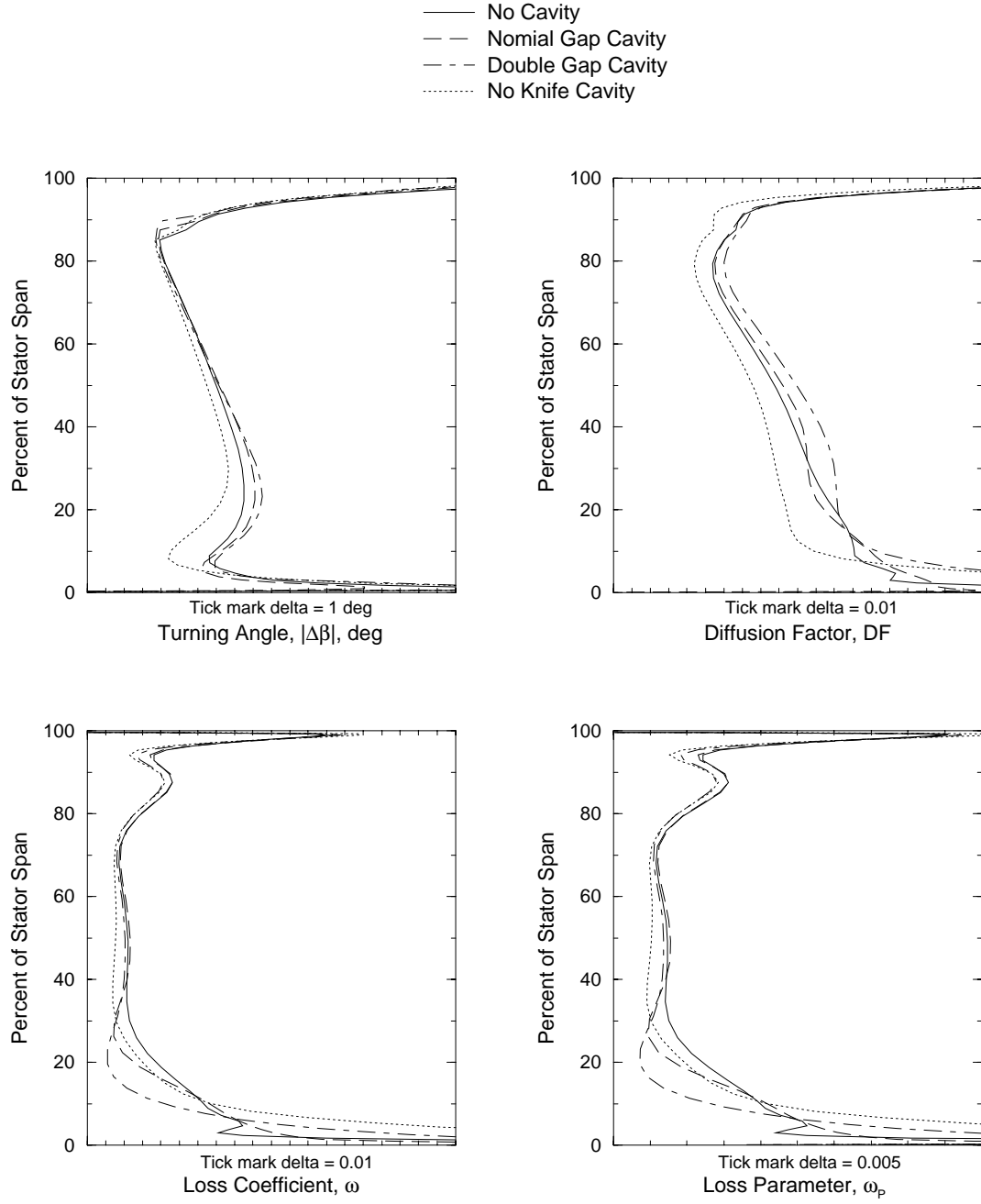


Figure 3.31: Radial distributions of the stator blade performance parameters measured across the outside stations (UP and DN).

between the three seal configurations, in combination with the approximately constant axial velocity, gave rise to a variation in tangential flow angle. This change in flow angle as the seal cavity flow re-enters the main flow explains some of the differences in the stator performance presented above.

After reviewing the radial distributions of flow variables and blade performance, a more detailed look into the 3-D flow solutions was conducted. Two performance issues studied in more detail were the impact of the different seal cavity geometries on the area of separated flow and the amount of power input into the flow by the seal cavity.

Stator Suction Surface Near-Hub Separation

The regions of separated flow were identified from near-wall distributions of axial velocity evaluated at one computational cell from the hub and suction surface of the blade. These distributions are shown in Figure 3.33 for each of the four seal cavity configurations; the bold contour line represents the boundary of zero axial velocity outlining the reversed flow regions. For the case with no cavity included, the stator blade showed a small amount of separation along the hub corner on the suction side starting at approximately 60% chord and extending radially to 20% span by the trailing edge. When the seal cavity was added, the separation on the suction side of the stator was reduced as more flow was allowed to pass through the seal cavity. A method of quantifying the level of separation was to calculate the size of the reversed flow area as a percentage of the total annulus area at the trailing edge. Contours of axial velocity across the trailing edge along with the reversed flow area measurements are shown in Figure 3.34.

This separation resulted primarily from the high incidence on the stator blade near the hub caused from the overturning in the rotor exit profile. The radial distributions of the incidence angle from the hub to 20% span, taken both upstream of the seal cavity trench and at the leading edge, are shown in Figure 3.35. Since all solutions had the same flow angles set at the inlet plane of the grid extension, there was already some adjustment in the incidence profiles by the upstream measuring station. The hub region blockage created by the seal cavity recirculating flow shifted the radial profiles higher, up to 5% at the leading edge in the highest seal cavity mass flow case. The amount of increased blockage due to the recirculating region around the stator inner band is shown in Figure 3.36. Figure 3.36 was generated by releasing particle traces at the corner of the upstream rotor wheel hub in an axisymmetrically-averaged solution for each of the seal configurations; while these traces do not represent 3-D stream surfaces, they do give an indication of the level of hub recirculation and the blockage associated with it. As the amount of mass flow through the cavity increased, the peak on the incidence distribution, shown in the right-hand plot in Figure 3.35, corresponding to the flow coming off the rotor wheel near the hub, had been shifted approximately the same amount by the point it reached the leading edge.

At 1% span off the hub for the case with no seal cavity present, the incidence on the blade was over 20 degrees higher than its midspan value. As the clearance of the seal tooth was increased allowing more mass flow through the seal cavity, the

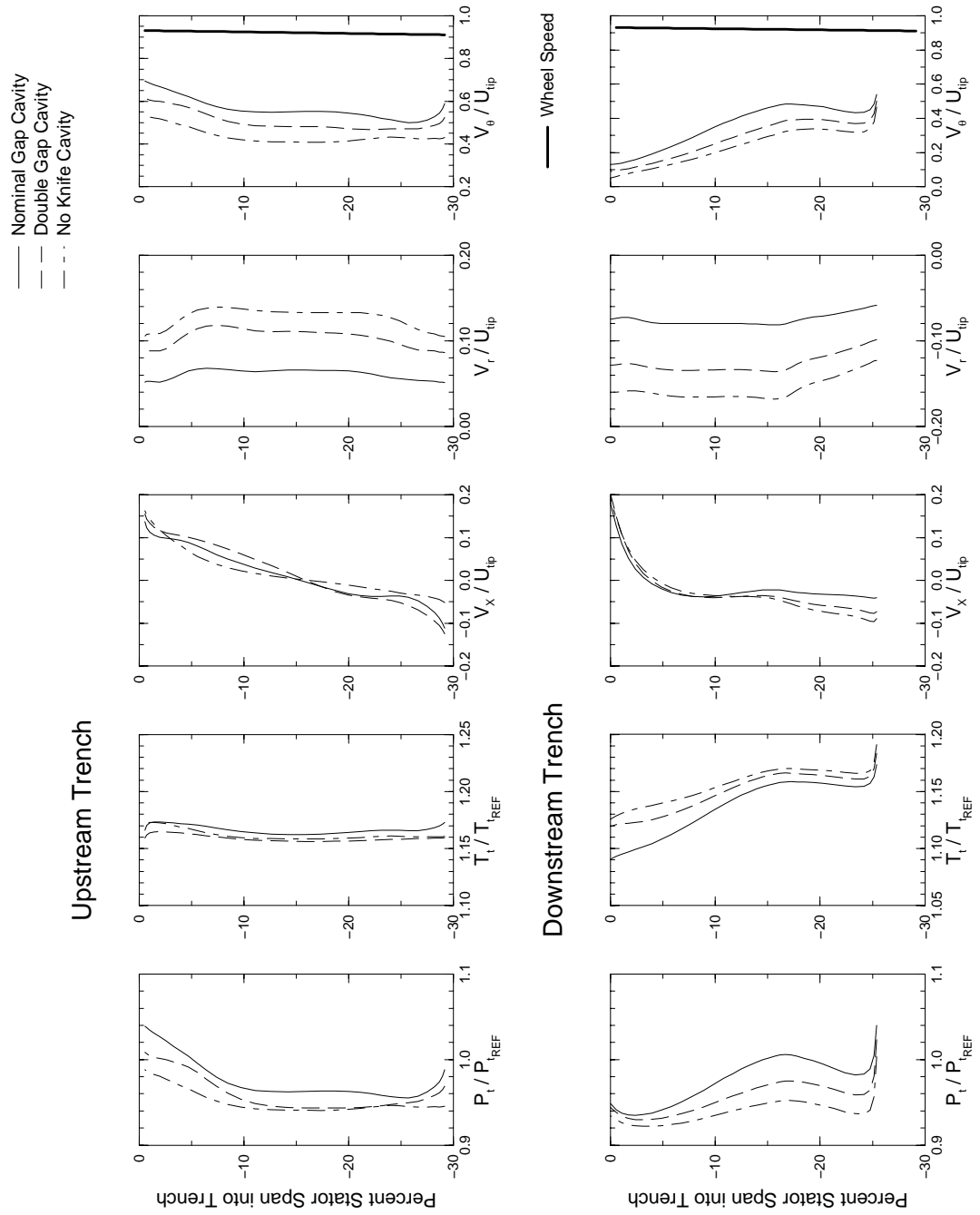


Figure 3.32: Radial distributions of area-averaged flow quantities into the upstream and downstream seal cavity trenches for various seal cavity configurations.

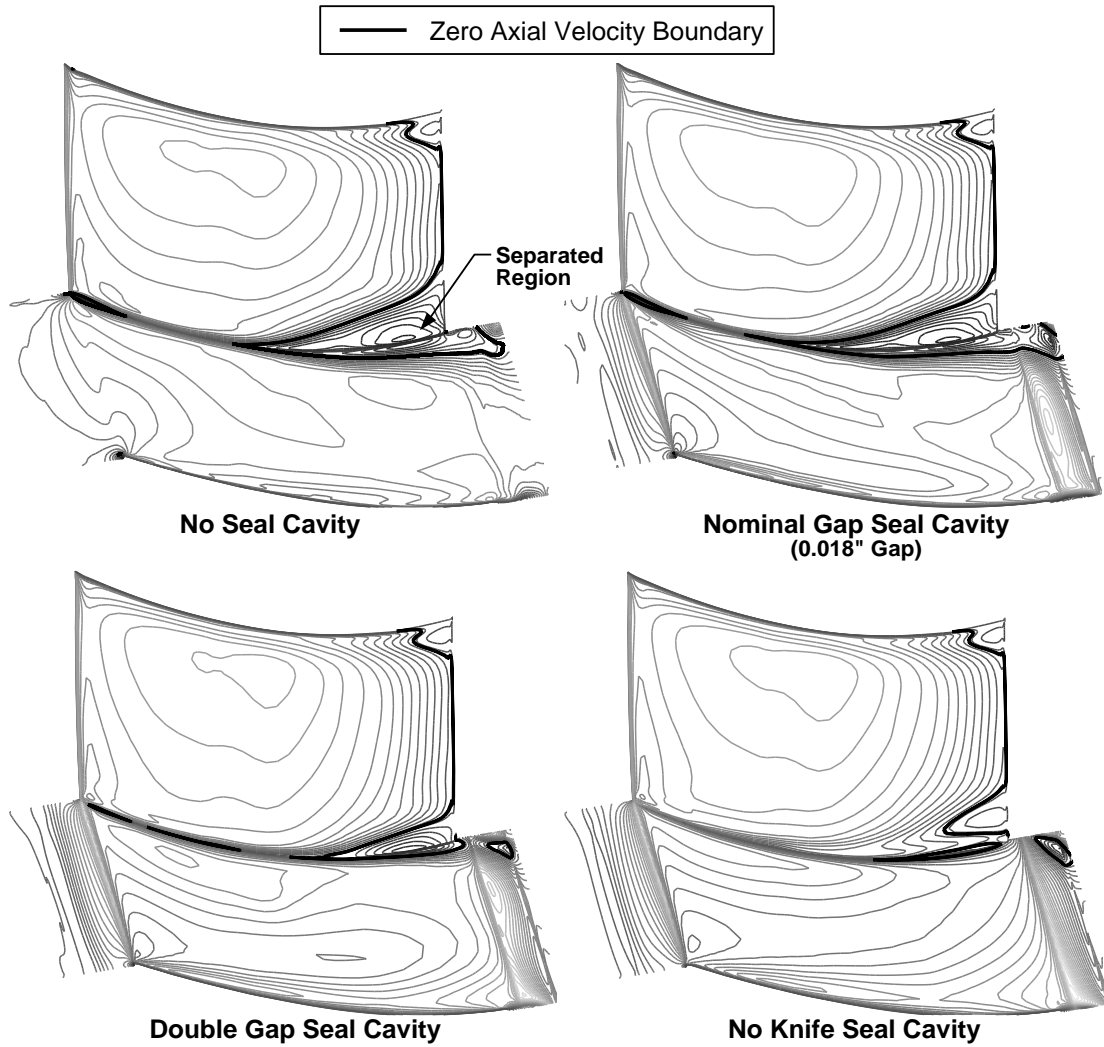


Figure 3.33: Near-wall axial velocity distributions along the hub and suction surfaces of the stator blade showing the variation in separation region between the four seal cavity configurations.



Figure 3.34: Axial velocity distributions across the trailing edge plane showing the regions of reversed flow.

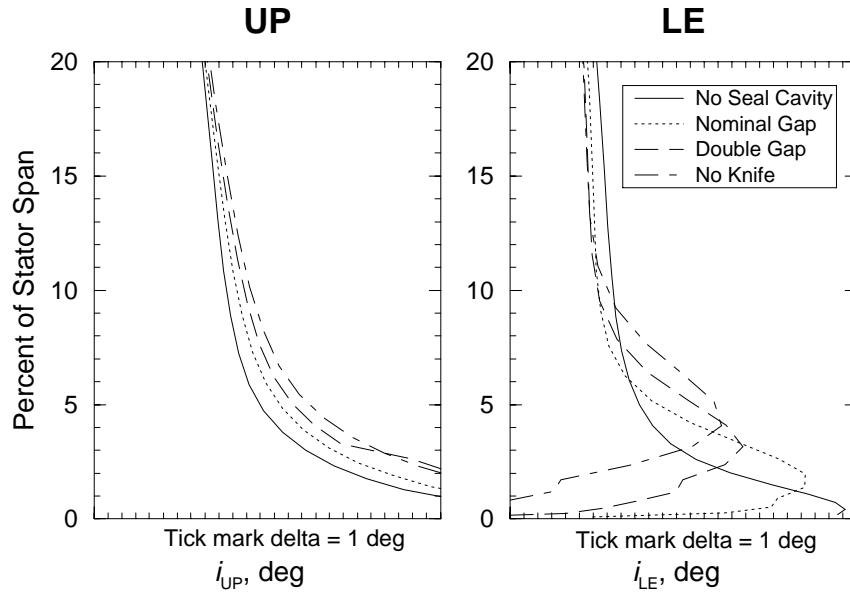


Figure 3.35: Stator blade incidence measured upstream of the seal cavity gap and at the leading edge.

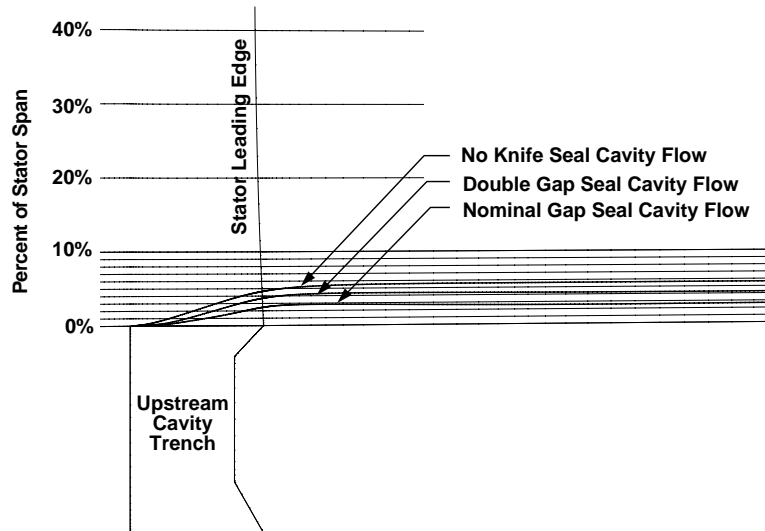


Figure 3.36: Particle traces released from the leading edge of the upstream seal cavity trench showing the blockage associated with the different seal cavity geometries tested.

tangential velocity of the flow being injected into the main flow path was decreased substantially as shown in Figure 3.37; the 50% wheel speed contour line has been emphasized to allow for easier reference and comparison. For the three geometries with seal cavities included, a significant range of injection tangential velocity was observed. The seal geometry with the least amount of mass flow had the highest mass-averaged injection tangential velocity of 67% wheel speed. When the seal tooth gap was doubled, the injection tangential velocity dropped to 56%, and with the tooth completely removed, it fell to 45%. The injection of slower tangentially-moving fluid near the hub region reduced the incidence on the stator blade, as seen in Figure 3.35, resulting in a smaller region of separated flow.

From these results with respect to the suction side separation, it appears that the tangential velocity of the injected fluid has significant effect on the stator performance. A reduction in swirl velocity was found by increasing the amount of mass flow through the cavity; however, this also increased the amount of blockage and loss near the hub. From spanwise distributions of swirl velocity down into the seal cavity trenches, the majority of the increase in tangential velocity is initiated within the first 15% span into the downstream trench.

Power Balance Through the Seal Cavity

The amount of work being input into the fluid as it travels through the seal cavity was calculated by two methods: by integrating the wall shear stress along all rotating surfaces in the seal cavity, and by calculating the difference in total energy entering and leaving the computational domain (all solid surfaces were adiabatic). The rise in total temperature between the inlet and exit planes had a much larger fluctuation over the history of iterations than the calculated wall shear stresses; however, the difference between the averaged values over 1000 iterations after convergence was reached of both power calculations was under 8% for the two solutions with the knife present and was 16% for the no knife seal cavity solution. The power values oscillated with iteration count due to the small variations in the total temperature of mass entering and leaving the computational region at different time intervals.

As the amount of mass flow through the seal cavity increased, by increasing the seal tooth gap, the work input into the flow also increased. The related increase in total temperature in the cavity flow was also measured. The power input through the nominal gap seal cavity makes up 94% of the total power input into the system with the remaining power entering the system through the rotating hub surfaces upstream and downstream of stator blade row. When the seal tooth gap was doubled, the amount of power input into the system increased by 21% over the nominal gap seal cavity geometry configuration.

In addition to calculating the global power input, the regions where large portions of the total work were input were identified by subdividing the cavity into separate regions. Approximately half of the work was input into the fluid by the downstream trench rotating wall, and the remaining work input was split between the two cavity volumes divided by the seal tooth. A small percentage of the work was input into the flow through the upstream cavity trench rotating wall.

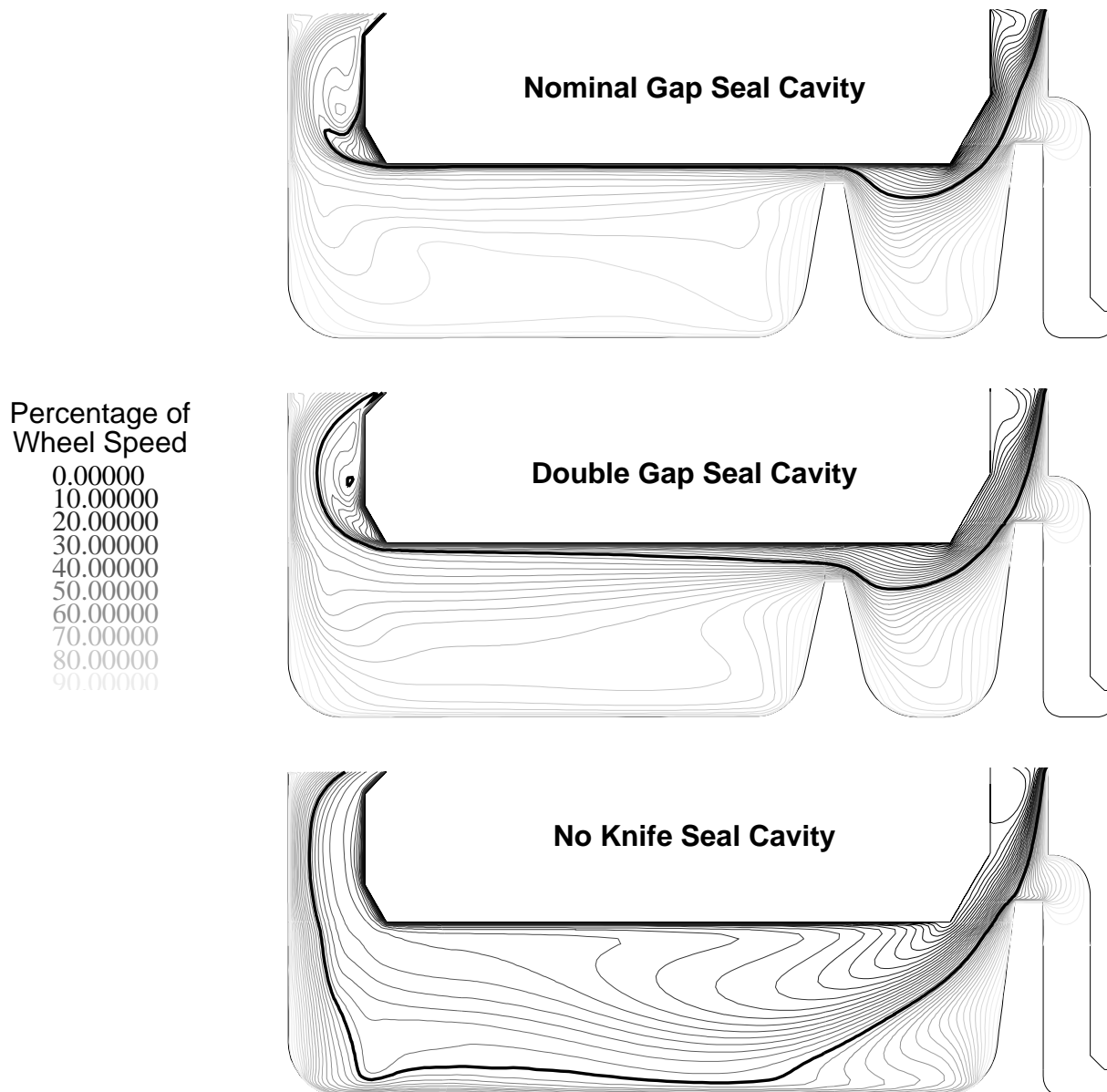


Figure 3.37: Axisymmetric-averaged tangential velocity distributions through the seal cavity as measured by wheel speed. The bold contour line represents the 50% wheel speed line.

Chapter 4

SEAL CAVITY PARAMETERIZED STUDY

4.1 Introduction

A parameterized study of the high-speed stator seal cavity required the collection of a series of solutions for different geometric variations. The parameter list included seal tooth gap, wheel speed, cavity depth, radial mismatch of hub flowpath, axial trench gap, hub corner treatments, and land edge treatments. An alternative sealing approach was also modeled using a rim seal geometry. This chapter describes the parameter list selection, the figures of merit used, the grid generation process used during the parameterized study, and the post-processing performed on the converged numerical solutions. Solution data presented include radial and pitchwise distributions of flow variables and particle traces describing the flow character. Results from the seal cavity parameterized study are presented as follows: first, a detailed look at the baseline configuration; second, a comparison of *all* the parameterized cases collected; and third, a more detailed look at each of the individual parameter groups.

4.2 Seal Cavity Parameter Selection

Several geometric parameters were identified for the seal cavity parameterized study. These parameters were split into two types, shown in Figures 4.1 and 4.2, respectively: those affecting the overall seal cavity configuration and those specifically affecting the seal tooth geometry. Since only a limited number of parameters could be investigated, the list of parameters was divided into two groups shown in Table 4.1. The top level parameters listed were those parameters identified as having the greatest impact on the interaction between the seal cavity flow and the main power stream. A test matrix of variations of these parameters was developed and is presented in the following section. Those parameters listed in the lower level were parameters that were considered but were not tested; most of these parameters described the details of the individual seal tooth and not the overall cavity geometry or the relative placement of the seal cavity with respect to the main flow path.

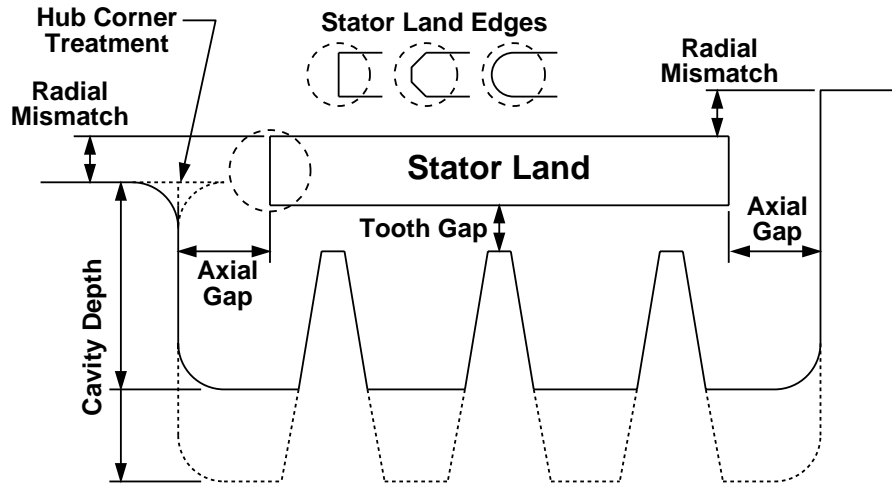


Figure 4.1: Geometric parameters defining the overall seal cavity geometry.

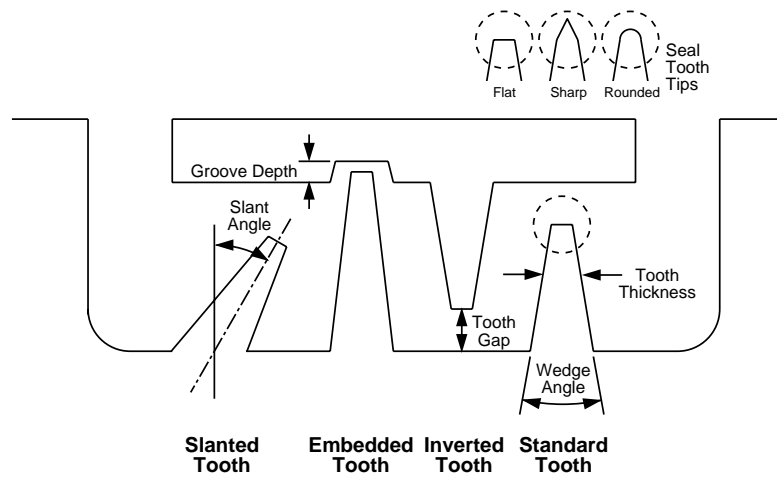


Figure 4.2: Geometric parameters defining the individual seal tooth geometry.

Top Level Parameters
<ul style="list-style-type: none"> • Seal Tooth Gap (Seal Cavity Mass Flow Rate) • Seal Cavity Depth (Cavity Volume) • Radial Mismatch of Hub Flow Path • Axial Gap Between Rotor Wheel and Stator Land • Rotor Wheel Hub Corner Treatments • Stator Land Edge Treatments • Rim Seal Geometry
Lower Level Parameters
<ul style="list-style-type: none"> • Seal Tooth Pitch (Height-to-Pitch Ratio) • Number of Seal Teeth • Inverted Seal Teeth • Seal Tooth Thickness • Seal Tooth Tip Treatment • Embedded Seal Teeth (Groove Depth) • Slanted Seal Teeth • Seal Tooth Wedge Angle

Table 4.1: Parameter lists dividing parameters into Top and Lower Levels.

4.2.1 Test Matrix Development

Using the top level parameters listed in Table 4.1 describing the labyrinth knife seal cavity configuration, a test matrix was developed to coordinate the collection and organization of the numerical solutions. In order to avoid an extremely large number of test runs requiring large amounts of computational resources and producing an overflow of data, only one of the parameters was varied at a time. Each of the parameters was varied individually away from a baseline geometry defined in a following section. Since some of the parameters could be applied to either the region near the upstream trench or near the downstream trench, a larger number of permutations was required to test all cases. In the test matrix shown in Figure 4.3, each of the primary seal cavity parameters is identified along with their baseline configuration value. A brief schematic is also provided to describe the variations of the parameter.

4.3 Figures of Merit

Figures of merit, listed in Table 4.2, were also identified in order to evaluate each parametric seal cavity design. Most of the figures of merit were concerned with the immediate effect of the seal cavity flow on the stator blade row. Also listed in the table are the flow variables used to quantify the figures of merit. One figure of merit considered but not listed was concerned with the impact of the seal cavity on the downstream rotor performance. Not only does the seal cavity flow affect the rotor

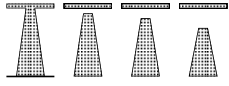
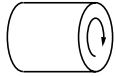
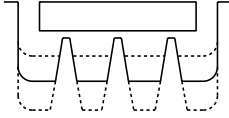
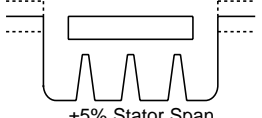
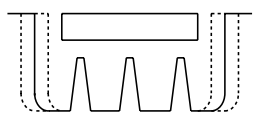
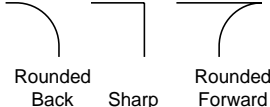

Parameter	Baseline Case	Variations
Seal Tooth Gap	0.010"	 No Cavity, No Gap, 0.020", 0.040"
Wheel Speed (RPM)	100%	 58% Baseline Speed
Seal Cavity Depth	0.184"	 $\pm 50\%$ of Baseline Cavity Depth
Radial Mismatch of Hub Flow Path Upstream Downstream	0.000" 0.000"	 $\pm 5\%$ Stator Span $\pm 5\%$ Stator Span
Axial Trench Gap Upstream Downstream	0.081" 0.061"	 $\pm 20\%$ of Baseline Gap
Hub Corner Treatment Leading Edge Trailing Edge	Sharp Sharp	 Rounded Back Sharp Rounded Forward
Stator Land Edge Treatment	Faceted	 Faceted Rounded

Figure 4.3: Test matrix of geometric parameters to be tested from the Baseline case.

Figure of Merit	Measured By
• Seal Cavity Mass Flow over Center Seal Tooth	\dot{m}
• Losses within the Cavity Due to Windage Heating	ΔT_t
• Injection Flow Velocity and Angle from Seal Cavity	$V_{\theta_{CAV}}$
• Stator Total Pressure Loss	ΔP_t

Table 4.2: Lists of primary figures of merit used to evaluate the several parameterized seal cavity solutions.

performance immediately downstream of the stator blade row, but it also affects additional stages downstream possibly compounding the effect of the seal cavity flow. Results in the previous chapter from the isolated rotor study with and without the effect of the seal cavity flow showed significant differences in the rotor performance. However, due to the length of time to calculate multiple blade row solutions and the large number of the parameter variations, it was decided to model the stator blade in isolation with the seal cavity.

4.4 Parameter Study Grid Generation

In order to maintain constant grid quality over the several grids to be generated for the parameterized study, a systematic procedure was developed. The previous meshes used in the High-Speed Compressor Study were generated using two separate grid generation codes: *TIGG3D* for the main blade passage and *GRIDGEN* for the seal cavity. These two grids were then combined into one multi-blocked mesh. This method worked well if the geometric changes only occurred completely within the seal cavity (i.e, tooth gap clearance) or within the main flow path. However, this method of generating each passage separately became iteratively cumbersome when varying parameters that affected the interface region between the two passages.

For this reason, a grid generation methodology that allowed for the definition of geometry and the distribution of points for both the main stator flow passage and the complex seal cavity passage simultaneously was required. The process was split into three parts: defining the geometry including any perturbations to the parameters, distributing the grid points in the axisymmetric meridional (x-r) plane, and expanding this axisymmetric distribution across the blade pitch.

4.4.1 Definition of the Coupled Geometry

The axisymmetric geometries of the seal cavity and the main flow path were defined using *GRIDGEN*. A utility program was written that read in a *TIGG3D* input file and output *GRIDGEN* network files which were used as databases for creating the main

flow path. The seal cavity database was extracted from a CAD database defining the high-speed compressor. Since both the main flow path and the seal cavity geometry were defined simultaneously, the interface region could be easily modified (i.e., radial hub mismatch, hub corner and stator land treatments).

4.4.2 Axisymmetric Distribution of the Points

With the boundaries of the geometry defined, the next step was to distribute points on the meridional plane. This step was also performed using *GRIDGEN*. The advantages to distributing points over both the main flow path and the seal cavity using the same program included: even near-wall spacing (0.0005") around the interface region, consistent elliptic smoothing of interior points, and exact matching at all mesh block boundaries. The near-wall spacing value was chosen as 0.01% of the stator span which corresponded to y^+ values in the range of 30 - 150, within the range of the wall functions accuracy. As the tight near-wall spacing was also held across the seal cavity trench openings, the axial distribution of points across this hub interface region was such that the aspect ratio of the computational cells in the center of the trench did not exceed twenty. The total number of points used over the geometries was similar to that for the Level 3 meshes used in the Grid Resolution Study; the number of grid points in the 3-D mesh totaled over 500,000 points split evenly between the main flow path and the seal cavity.

The baseline grid was generated using this method and the meridional plane distribution of the points is shown in Figure 4.4. The configuration geometry was similar to grids used in the High-Speed Compressor Study with the exceptions of a tighter knife seal gap and the removal of the "boot" section of the mesh. This "boot" removal was done to save grid points as the flow in this region in all the high-speed study solutions was in pure rotation and had minimal impact on the seal cavity flow solution.

4.4.3 Pitchwise Distribution of Points

After the meridional distribution was complete, a 2-D mesh file defining all the (x,r) coordinates of the points was generated. A utility code was written to read this 2-D mesh file and the stator blade shape from the original *TIGG3D* input file and to construct the grid in the main flow path through the stator blade. The code used a bilinear interpolation scheme to project the meridional points onto the pressure and suction sides of the blade definition. The pitchwise placement of the points was governed by a symmetric distribution about the mid-passage surface holding a user-input near-wall spacing (0.0005"). The angles of the grids extending upstream of the leading edge and downstream of the trailing edge were user specified. The new method defined the blade leading and trailing edges better than the previous method used in the High-Speed Compressor Study as shown in Figure 4.5.

After a standardized grid generation procedure was established for the parameterized study, the creation of the remaining grids proceeded. Each new grid started with

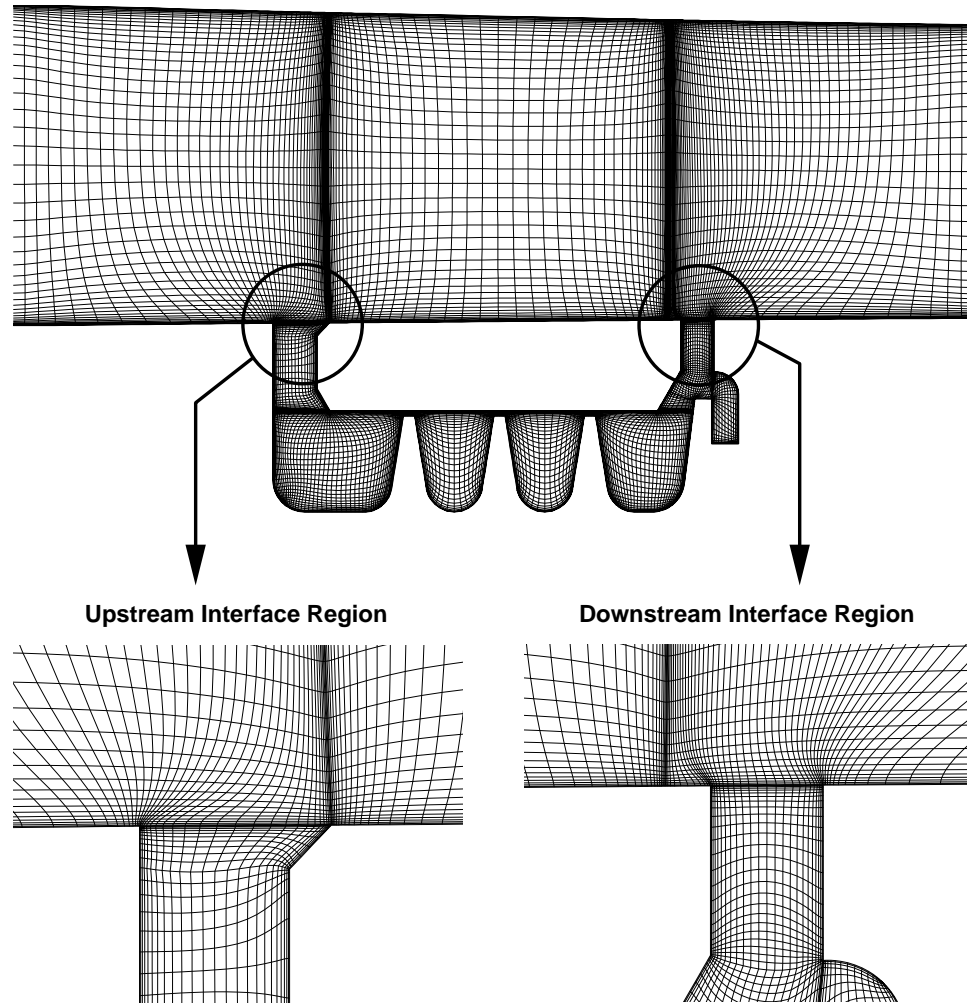
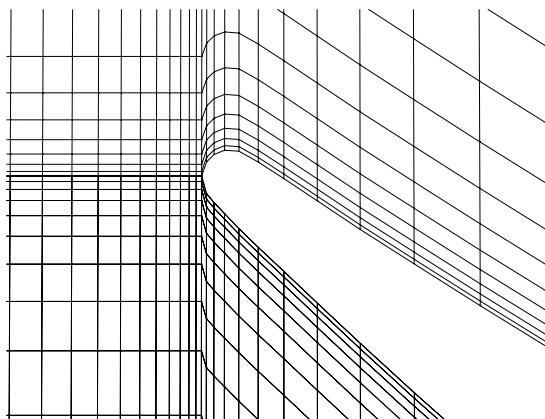
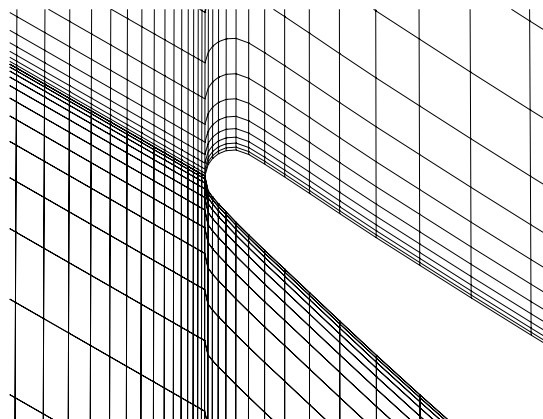


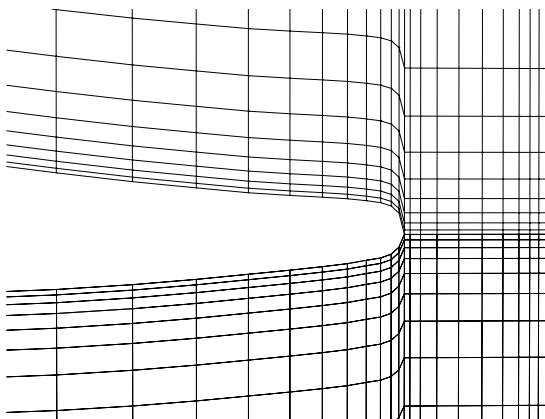
Figure 4.4: Meridional plane mesh distribution for the baseline triple-knife seal cavity coupled to the stator main flow path. Details of the upstream and downstream interface regions are highlighted in the lower half of the figure.



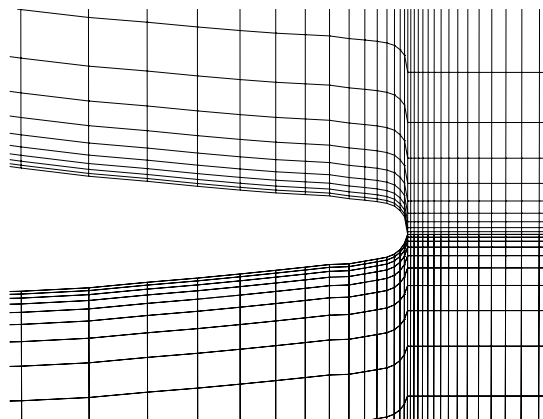
Leading Edge
Previous Method



Leading Edge
New Method



Trailing Edge
Previous Method



Trailing Edge
New Method

Figure 4.5: Comparison of the grids around the leading and trailing edges at the hub surface from the previous and new grid generation methods.

the baseline geometry and point distribution file, and any changes were made from this baseline definition. This ensured that the majority of the grid distributions were the same except for the localized region affected by the specific parameter which was being varied. Results for each of the parameter variations that follow show meridional slices through each of the different grids. These 2-D grid representations define the axisymmetric seal cavity geometry. The baseline configuration is included with all of the figures for comparison.

4.5 Numerical Solution Collection and Post-Processing

Because this parameterized study was based on 3-D Navier-Stokes simulations, a large number of CPU hours was required to complete all of the solutions for the several test configurations. However, the total calendar time required for these solutions was reduced by making use of the portability and flexible parallelization of the *ADPAC* code. Solutions were collected on several different computing platforms simultaneously throughout the Seal Cavity Flow Investigation. Details of the solution collection on different parallel computing platforms can be found in the appendix.

The parameterized solutions were obtained using a constant mass flow exit boundary condition; the exit back pressure was iteratively changed internally by *ADPAC* until a prescribed exit mass flow was reached. This allowed for comparison of velocity profiles and stator blade performance numbers between seal cavity configurations for the same mass flows. A list of primary results used for comparison included mass flow calculations through the seal cavity, pitchwise profiles in the upstream and downstream trench gaps, and radial profiles of stator blade performance. Radial profiles of velocities, flow angles, and performance data were extracted from each of the converged solutions.

The computational meshes were generated with consideration given to fitting the seal cavity geometry, reducing the amount of grid shear and limiting cell expansion ratios. This process, while a requirement for satisfactory solutions, did not always allow for the exact matching of every grid line between seal cavity configurations or allow grid lines to follow a constant axial location near the blade. Therefore, a set of two constant axial location data planes from the main passage solution were extracted at the UP and DN locations described in the previous chapter. The stator blade performance and radial profiles were evaluated from these data at the exact same location in every solution regardless of the computational mesh locations. As in the High-Speed Compressor Study, the axial location of the upstream data station corresponded to the trailing edge of the upstream rotor; likewise, the downstream data station corresponded to the leading edge of the downstream rotor as shown in Figure 3.6.

Pitchwise distributions were obtained by interpolating the flow solution to a plane of constant radius passing through the solution and then calculating mass-averaged flow quantities across that plane for separate $\Delta\theta$ segments. Investigations of the Baseline case showed that pitchwise profiles became somewhat axisymmetric (not varying across the pitch) below 5% of the stator span into the seal cavity trenches.

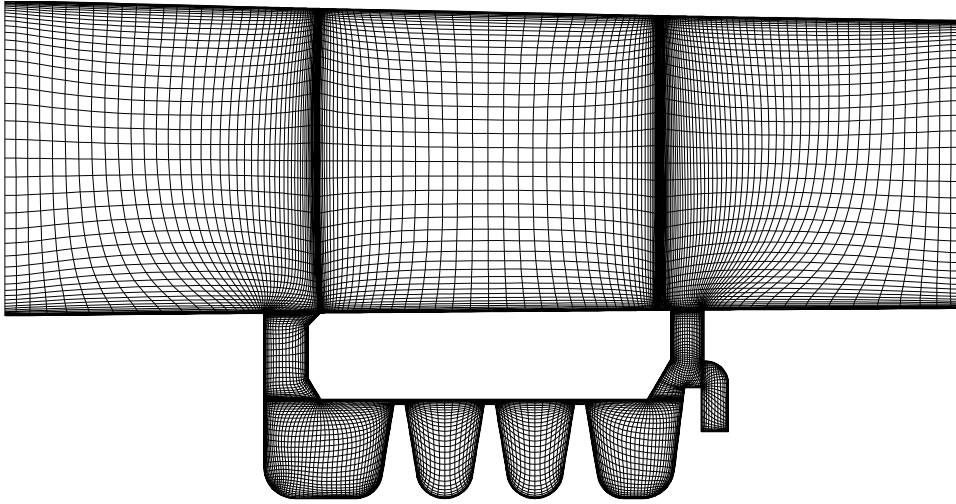


Figure 4.6: Meridional slice of the Baseline configuration mesh showing the coupled stator and seal cavity.

Therefore, flow quantities were measured at the constant radius plane corresponding to -5% stator span in both the upstream and downstream trenches. The flow data were directionally mass averaged; the flow was separated into two averages depending upon the direction the normal velocity vector pointed across the constant radius plane. These averaged flow data was used for comparison between all the parameterized cases.

4.6 Baseline Case Description

A baseline cavity configuration which was representative of a seal cavity used in current compressor design was defined. This cavity consisted of three knife seals equally spaced across the seal cavity with a height-to-pitch ratio close to one. The gap between the tip of the squared knife edges and the bottom of the stator land was set at 0.010 inches (1.79% stator span), which produced a seal cavity leakage mass flow of approximately 0.6% of the main power stream mass flow. This baseline knife seal gap was **half** of the “nominal” case tested in the High-Speed Compressor Study and was believed to be more representative of actual seal tooth clearances. The Baseline case had no radial mismatch in the hub flow path as the hub flow path was essentially a straight line with a small degree of slope. The minimum axial gaps of the trenches between the rotor wheel and the stator land were the same as those used for the high-speed study with the upstream trench slightly larger than the downstream trench. The rotor hub had sharp 90-degree corners at both the upstream and downstream trenches. The stator land edges were also the same as those in the high-speed study model, having faceted leading and trailing edges.

4.6.1 Comparison of 3-D and 2-D Axisymmetric Seal Cavity Solutions

One of the objectives of this investigation was to collect a database of seal cavity solutions to be used in future work to possibly generate a simplified seal cavity model. To model every seal cavity passage in a multi-stage compressor with a 3-D analysis would take large amounts of grid points and computational time with current resources. One option to reduce this burden is to model these cavities with a 2-D axisymmetric analysis. While a 2-D axisymmetric solution of the seal cavity does not give all the details of the complex 3-D flowfield, it can be used to determine global effects upon the stator flow.

As a test example, an axisymmetric solution of the baseline seal cavity was run and compared to the axisymmetrically area-averaged 3-D baseline solution. Over the upstream and downstream cavity trenches, the main flow field was modeled using two plenums. The locations and sizes of these plenums are shown in Figure 4.7 along with the stator blade location. Two separate plenums were needed to support the adverse pressure gradient without the presence of the stator blade to turn the flow. Boundary conditions for these plenums were set such that the main flow conditions at the entrances to the seal cavity trenches were the same as in the averaged 3-D solution; the inlet and exit conditions were extracted from the averaged 3-D solution and the upper boundary was modeled as an inviscid wall simulating a streamline.

Non-dimensional radial profiles were extracted from the axisymmetrically-averaged 3-D solution and the 2-D axisymmetric solution at the mid-trench location in both the upstream and downstream cavity trenches. These radial profiles are shown in Figures 4.8 and 4.9. The mid-trench axial locations corresponded to where experimental data might be typically measured, as was the case in the LSAC experimental study [9]. When the main flow boundary conditions were modeled correctly, the agreement between the 3-D solution and the axisymmetric solution was very good. The pressure distributions set up fairly quickly whereas the temperature distributions took longer to settle to steady-state values.

The temperature profiles did show the large heating of the leakage flow as it passed through the cavity; approximately half of the temperature rise occurred in the downstream trench before reaching -25% stator span. The peaks in p_t , T_t , V_θ , and V_{abs} located at the 0% span location were attributed to the hub boundary layer coming off of the upstream rotor. As was expected, the radial velocities are positive in the upstream trench and negative downstream. The static pressure distribution showed very little radial variation at both the upstream and downstream locations. A significant increase in tangential velocity occurred almost immediately after the leakage flow entered the downstream trench. A corresponding increase in total temperature was also observed as energy from the spinning rotor wheel was transferred to the leakage flow. Some of these same trends were also found in the pitchwise distributions in the cavity trenches which are presented in the following section.

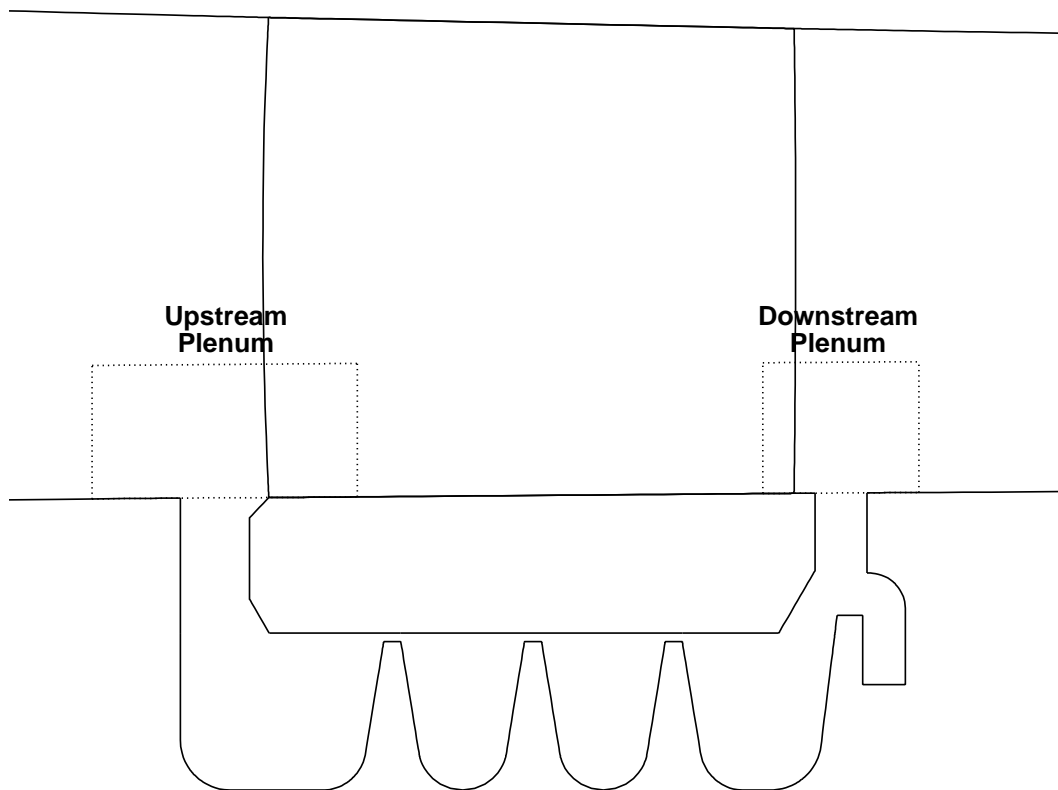


Figure 4.7: Location of upstream and downstream plenums (dotted lines) for simulation of the main flow in the axisymmetric solution.

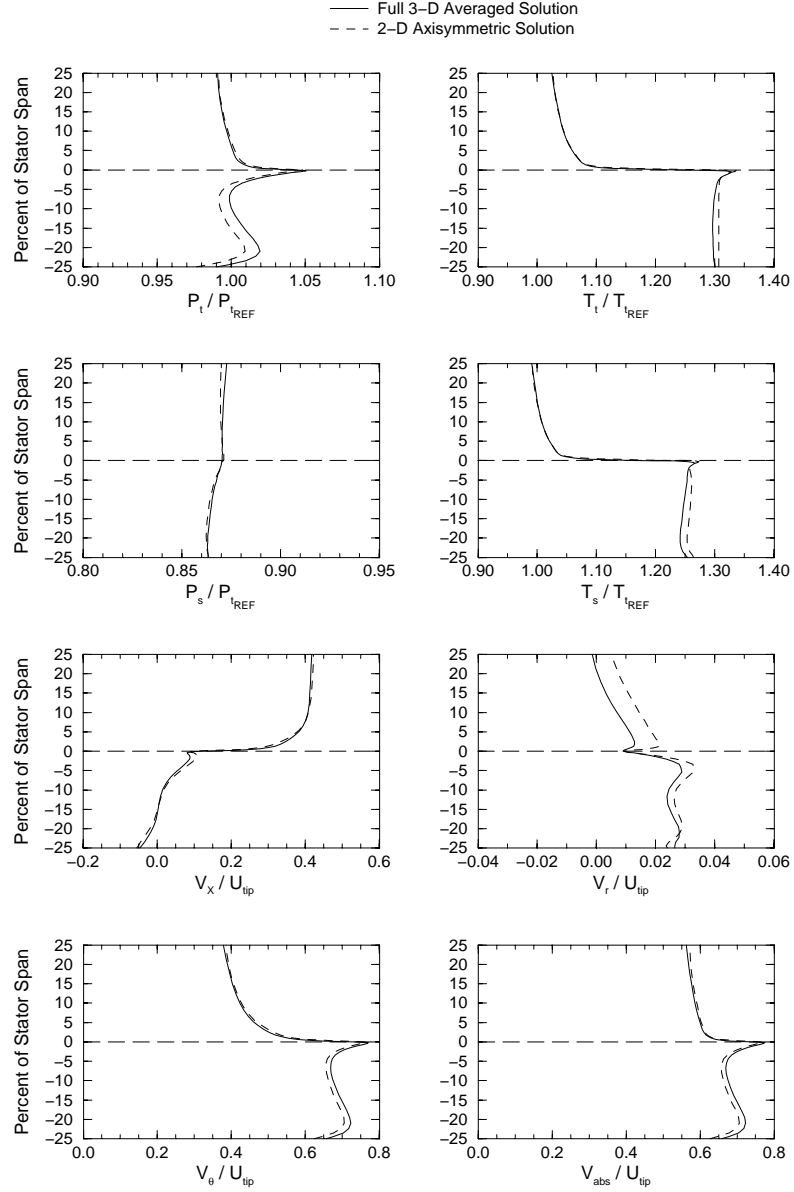


Figure 4.8: Comparison of radial distributions at upstream mid-trench axial location between the averaged full 3-D baseline solution and the 2-D axisymmetric solution.

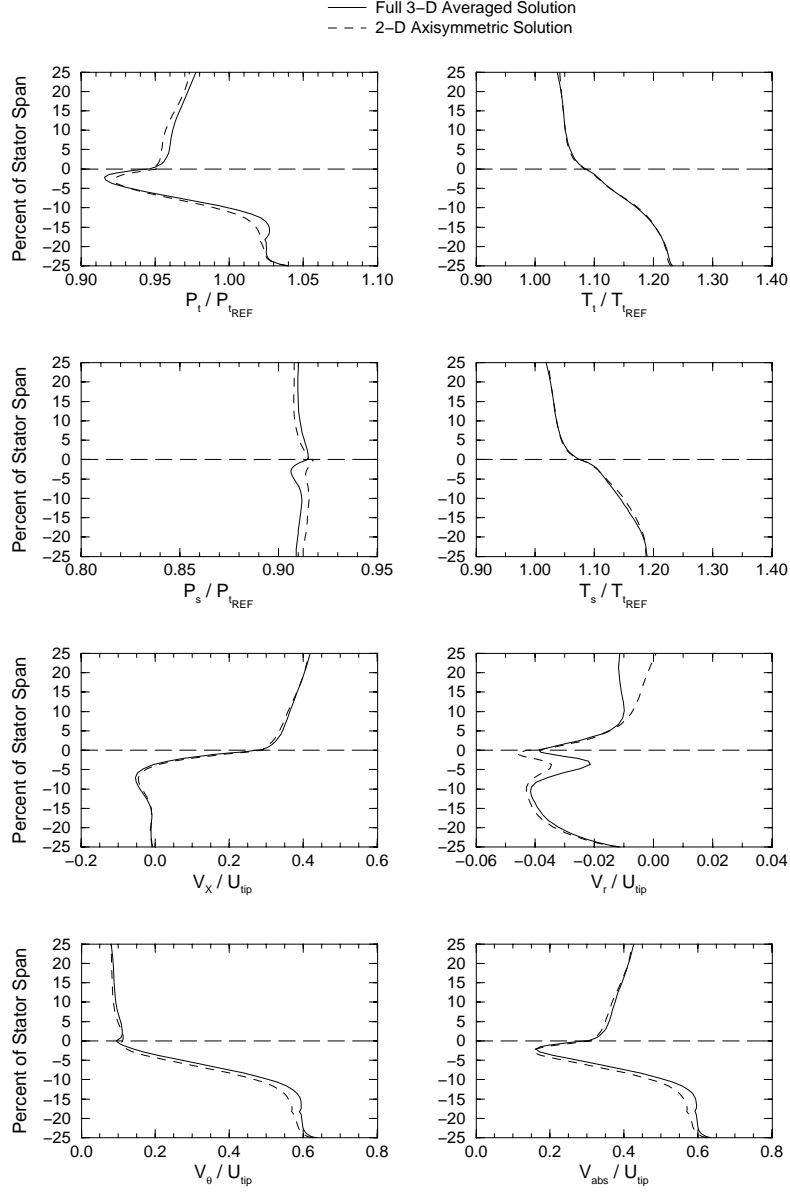


Figure 4.9: Comparison of radial distributions at downstream stream mid-trench axial location between the averaged full 3-D baseline solution and the 2-D axisymmetric solution.

4.6.2 Pitchwise Distributions in the Cavity Trenches

Data on constant radius surfaces were extracted from the baseline solution at several spanwise locations (0%, -5%, -10%, -15%, and -20%) extending into the seal cavity trenches shown in Figure 4.10. These data were then mass-averaged across the pitch of the blade passage. Presented in Figures 4.11 and 4.12 are the pitchwise distributions of total and static pressures and temperatures and the velocity components. By comparing the distributions through the trench, the effective influence region of the main flow path was determined. The stator blade flow field did have an impact upon the seal cavity. However, this impact diminished with distance into the trench, and at approximately -10% span the distributions show almost no pitchwise variation.

There was both positive and negative radial flow in both the upstream and downstream trench gaps along the hub. In the upstream trench, some of the main flow was forced into the seal cavity in the region of the stator leading edge; in the downstream trench some of the flow exited the trench into the main flow primarily in the high loss region of the stator wake. The decrease in static pressure across the blade passage in the upstream trench was shown from the pressure side to the suction side most prominently at 0% span and lessened with distance into the trench.

As was shown in the mid-trench radial property distributions in Figures 4.11 and 4.12, as the leakage flow entered the downstream trench, the tangential velocity increased. The tangential velocity appeared to reach a maximum near -10% span; from the particle traces of the Baseline case, this corresponded to the location where the leakage flow comes in closest contact to the spinning downstream rotor. A corresponding rise and fall in total pressure was also observed going into the downstream trench. The total temperature levels continue to increase with decreasing span location as more energy was imparted to the leakage flow.

4.7 Comparison of All Parameterized Cases

The figures of merit listed previously were calculated for the parameterized seal cavity solutions. The results for all the cases are plotted in Figure 4.13. This figure includes the seal cavity leakage mass flow as a percentage of the stator blade passage mass flow, the total pressure drop across the stator blade row, the total temperature rise across the stator blade row, and tangential velocity comparison at both the upstream and downstream cavity trenches. In the tangential velocity graphs, the open circles represent the mass-averaged value of V_θ in the stator main flow passage measured at the constant axial data planes described earlier; the filled circles represent the directionally mass-averaged tangential velocity of the seal cavity leakage flow calculated at the -5% span location. That is, in the upstream trench, only flow with a positive radial velocity component was included in the mass-average and conversely, in the downstream trench, only negative radial velocity component regions were used; this was done to reduce the effect of the rotating region of leakage flow just inside the cavity trenches. In Figure 4.13, the thin horizontal line corresponds to the baseline configuration value, and the thick vertical lines separate the several cases tested into

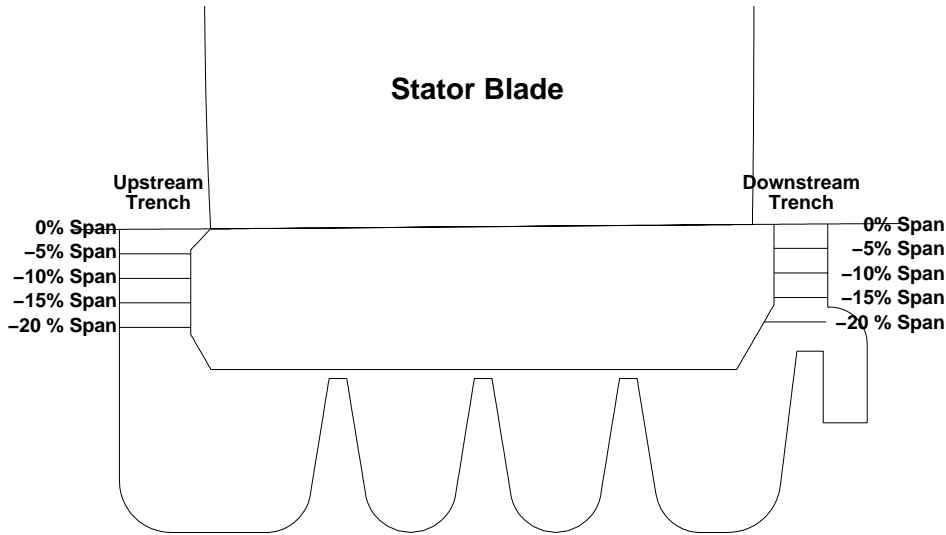


Figure 4.10: Spanwise locations where flow quantities were mass-averaged generating the pitchwise distributions across the upstream and downstream trench gaps.

related parameter groups.

Overall trends will be discussed below, leaving many of the details for the individual parameter sections to follow. With respect to leakage mass flow, most of the cases, except the tooth gap parameter set, did not vary significantly from the baseline leakage rate of 0.60% of the main passage mass flow. The weak relationship between leakage flow rate and rotational wheel speed had also been seen in earlier experimental studies [2]. The tooth gap parameter mass flow results appeared to vary almost linearly with increasing tooth gap; this point is discussed in further detail when the tooth gap parameter results are compared with the current seal cavity design analysis predictions in the tooth gap section.

The total pressure loss graph again showed most of the data points near the baseline levels. The variation with hub radial mismatch showed a much greater sensitivity to the upstream cavity mismatch than downstream. The decrease in total pressure drop as the tooth gap increased was surprising as one would expect that as the leakage flow increased so would the mixing losses through the stator blade; however, since the flow exiting the upstream cavity was at a higher energy state than the main stator flow, any mixing losses might have been reduced by this high momentum leakage flow. This would also explain the higher total pressure drop when the wheel speed was reduced in that the flow exiting the upstream cavity was at a lower energy state than in the Baseline case.

The total temperature rise across the stator was due entirely to the injection of seal cavity leakage flow since no other mechanism for energy addition existed. Rises in T_t corresponded to a combination of the amount of leakage flow and the increase in tangential velocity of that flow through the cavity. For example, with the tooth gap parameter results, as the leakage mass flow increased the rise in total temperature also

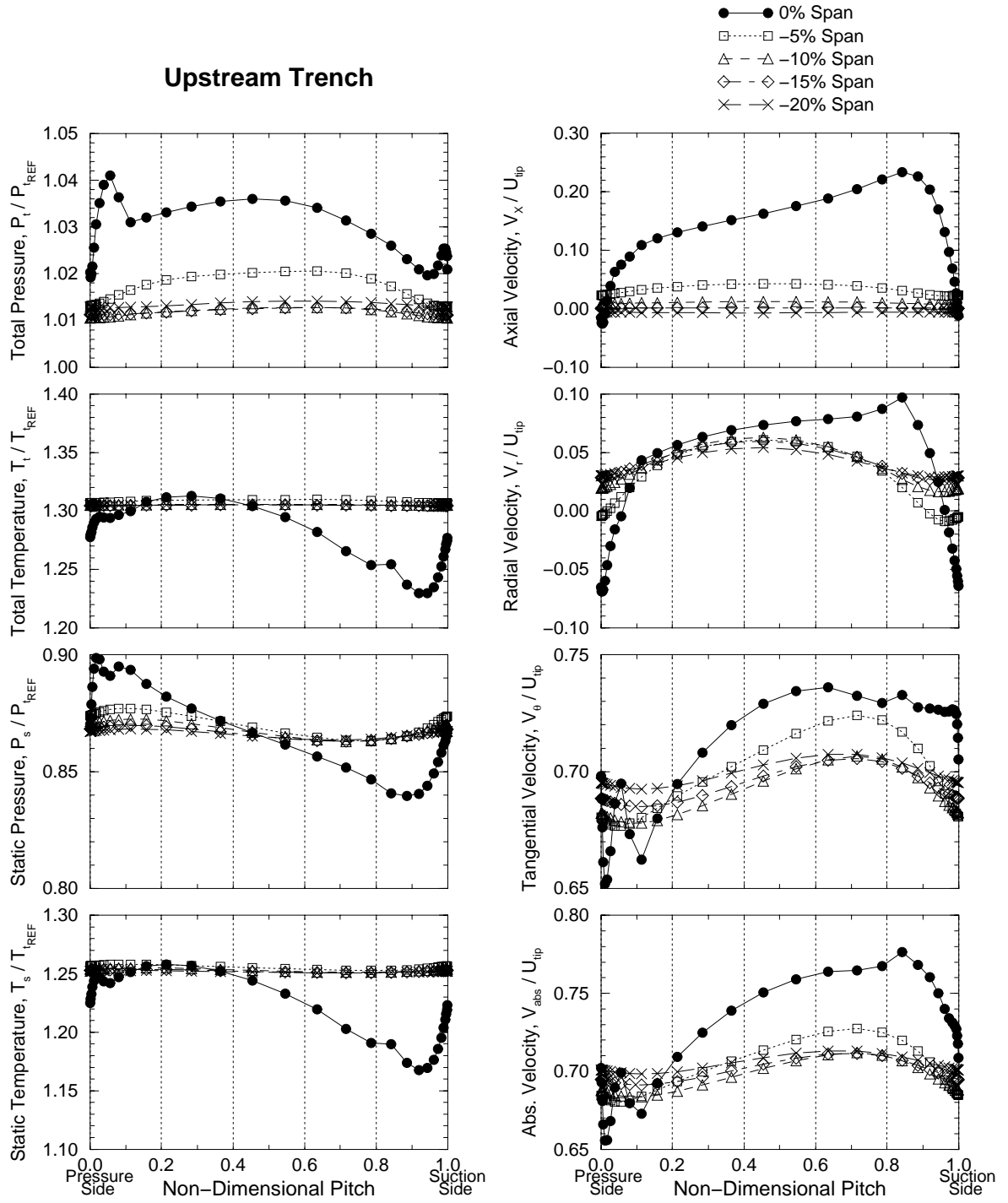


Figure 4.11: Pitchwise variation of flow quantities mass-averaged across the upstream trench gap at several spanwise radii for the Baseline case.

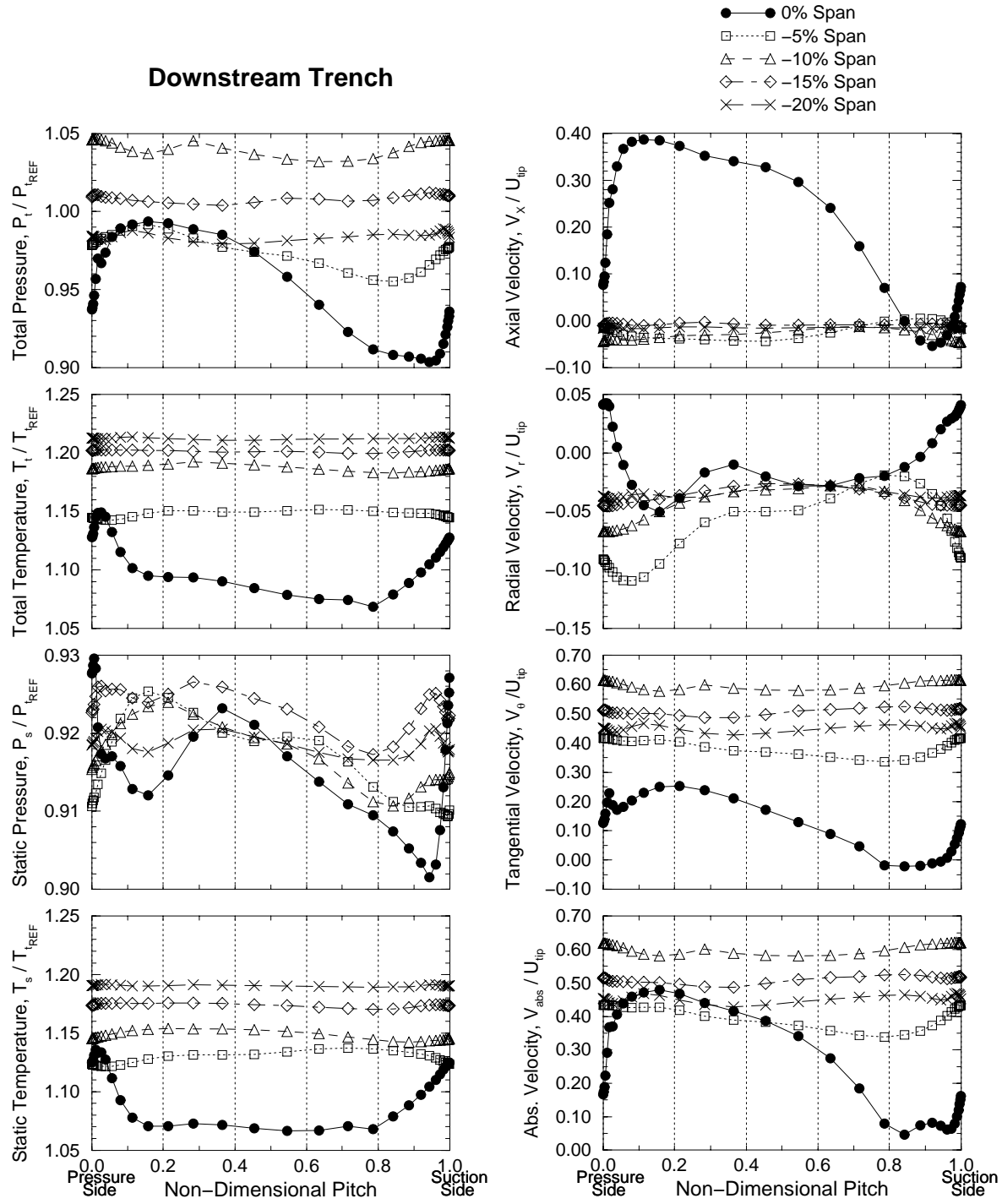


Figure 4.12: Pitchwise variation of flow quantities mass-averaged across the downstream trench gap at several spanwise radii for Baseline case.

increased despite a decrease in tangential velocity speed-up. Also, when the wheel speed was reduced, thereby decreasing the tangential velocity increase through the cavity, the rise in total temperature across the stator decreased for the same leakage flow rate. The rim seal geometry solution also showed this same trend. As was noted in the axisymmetric solution comparison, the temperature field took significantly longer to reach a steady state than the pressure field. Due to this larger uncertainty in the temperature values when compared to values of pressure and velocities, only general comparisons will be made where significant differences exist.

The comparison of tangential velocity showed an interesting character of the high-speed seal cavity leakage flow. In the downstream trench, the leakage flow was accelerated tangentially extremely quickly as it reaches almost two-thirds of its upstream trench value by -5% span into the downstream trench. As the amount of leakage flow increased, the amount of tangential velocity spin-up decreased. The lower wheel speed case was tested to try and match the exiting leakage flow tangential velocity to the stator freestream value as wheel speed had an obvious strong affect on the tangential velocity. The rim seal geometry did show a slightly lower exit velocity than the Baseline case as alluded to in the discussion of total temperature rise above. However for most cases, the exit tangential velocity from the upstream seal cavity trench remained close to the baseline and significantly different from the freestream value and was not affected greatly by the changes in the seal cavity design tested. This may indicate that as compressor designs evolve to higher wheel speeds corrective action for this injection of higher tangential velocity needs to be addressed in the design of the stator blade rather than the seal cavity.

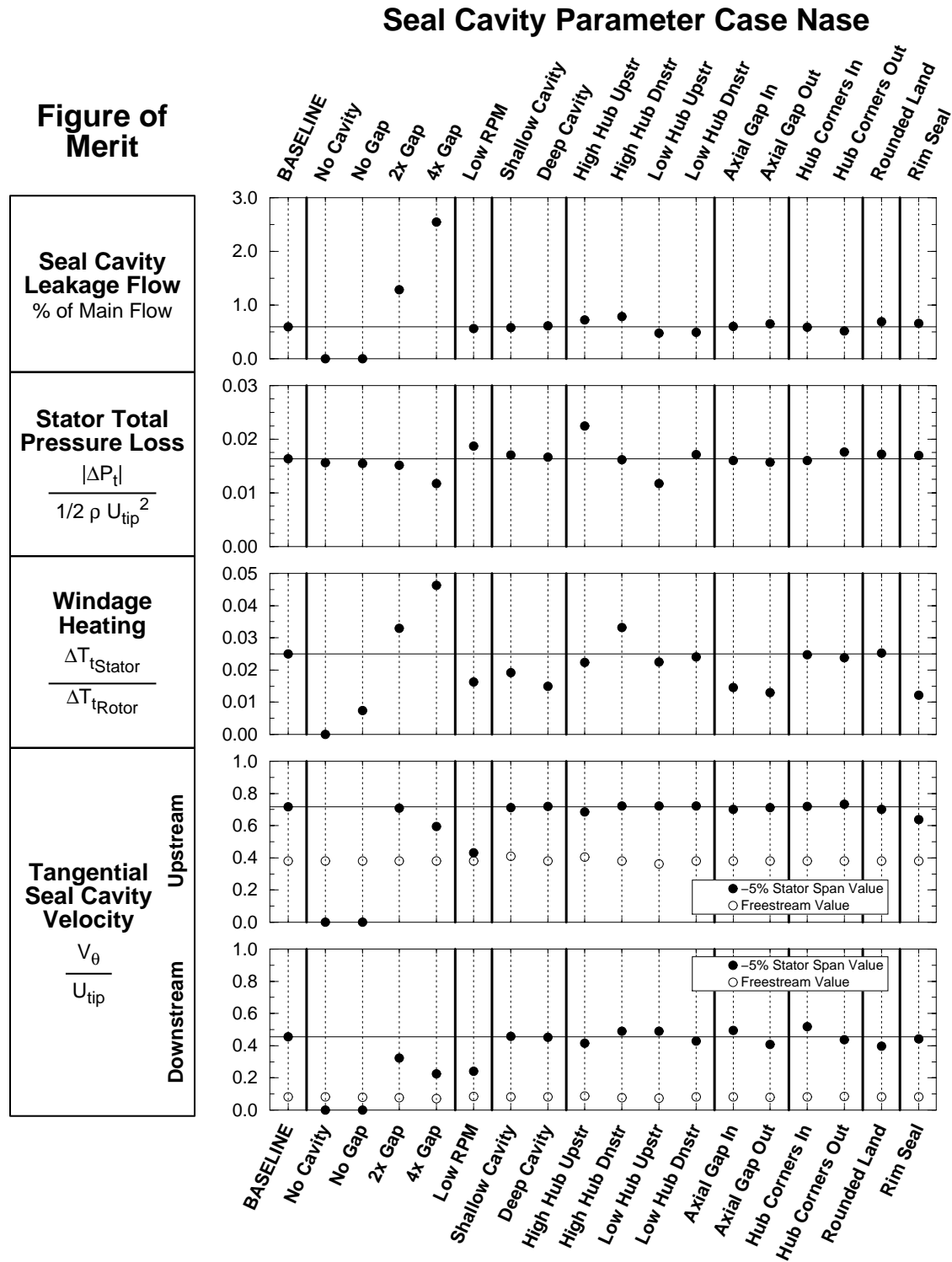


Figure 4.13: Comparison of the figures of merit for all parameterized seal cavity solutions collected.

4.8 Tooth Gap Parameter

The seal tooth gap between the knife tip and the stator land was varied to throttle the amount of seal cavity leakage flow. The geometries tested and their corresponding meshes are shown in Figure 4.14. In addition to a No Cavity solution, a No Gap solution was also collected to simulate the limiting case of the seal teeth embedded into the stator land allowing no leakage flow. The mass flows through the seal cavity as a percentage of the mass flow through the stator blade row were shown previously in Figure 4.13. The expected increase in mass flow through the cavity with increasing tooth gap was approximately linear in the region tested.

Particle traces for the axisymmetrically-averaged cavity solutions are presented in Figure 4.15. From these results, the overall structure of the seal cavity flow does not appear to change dramatically with the increase in tooth gap. In all the solutions, clockwise-rotating driven cavities appear in *both* the upstream and downstream seal cavity trenches. The size of the driven vortices is radially longer in the upstream trench than in the downstream trench; this is partially due to the fact that the rotor wheel pumping force is in the same direction as the main axial flow in the upstream trench region and in the opposite direction downstream. When no seal cavity leakage flow is present, these rotating regions fill the trenches completely as seen in the No Gap solution. As the seal cavity leakage flow is increased, these vortices in the trenches become compressed against the stator land.

Also shown in Figure 4.13 is the tangential component of the mass-averaged exit velocity leaving the upstream seal cavity trench. This flow variable is linked to the incidence on the leading edge of the stator near the hub and to the resulting size of separation region starting at the mid-chord on the suction side of the stator blade near the hub. Figures 4.16, 4.17, and 4.18 show the radial profiles of velocities, flow angles, and performance data, respectively, for the Tooth Gap parameter solutions.

The results from the Tooth Gap parameter solutions showed trends similar to those collected earlier under the High-Speed Compressor Study. In Figure 4.16, the radial distributions of upstream axial velocity show that as the leakage rate through the cavity increased (a result of increasing tooth gap), the velocity profile near the hub decreased and increased slightly over the upper span to maintain mass flow. Exiting the stator blade row, the axial velocities near the hub show increasing velocity deficits as the leakage flow was increased.

Figure 4.19 shows the axial velocity contours just above the hub surface where negative values are enclosed between the contour line and the blade shape boundary. As the seal cavity flow increased, the near-hub region of separation along the suction side appeared to decrease at this near-hub slice. The No Cavity, No Gap, and Baseline cases all appear to have the same amount of separated flow region near the hub. As the leakage flow was increased, the region of reversed flow decreased near the hub; this is primarily the result of the reduction in the leading-edge incidence on the stator blade. Also possibly contributing to this reduction is the fact that as the leakage flow was increased enlarging the hub recirculation zone, the region of separated flow was “pushed” radially outward beyond the near-hub cutting plane.

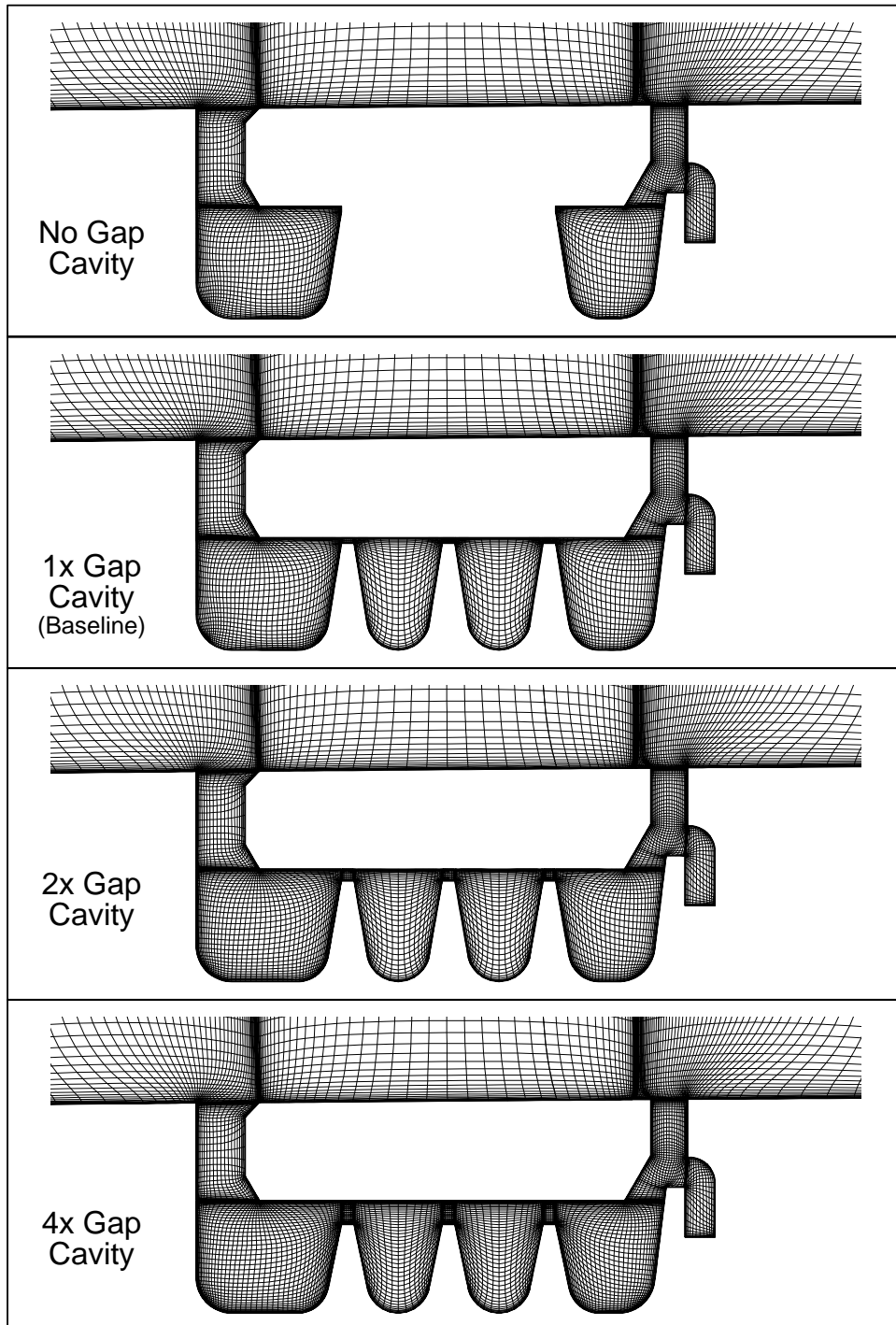


Figure 4.14: Meridional plane grids showing the variation of the Seal Tooth Gap parameter.

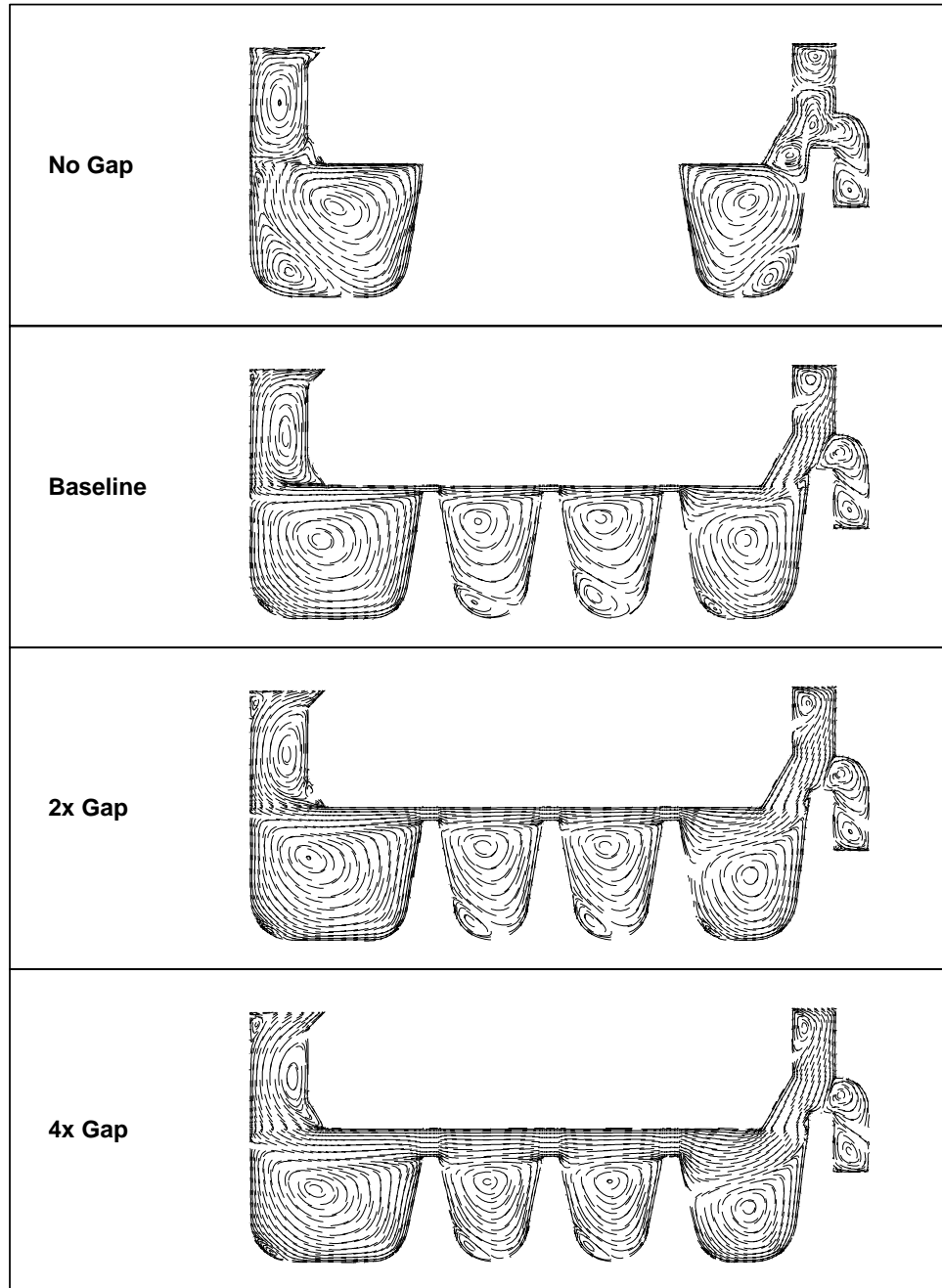


Figure 4.15: Axisymmetrically-averaged particle traces within the seal cavity for the Tooth Gap parameter series.

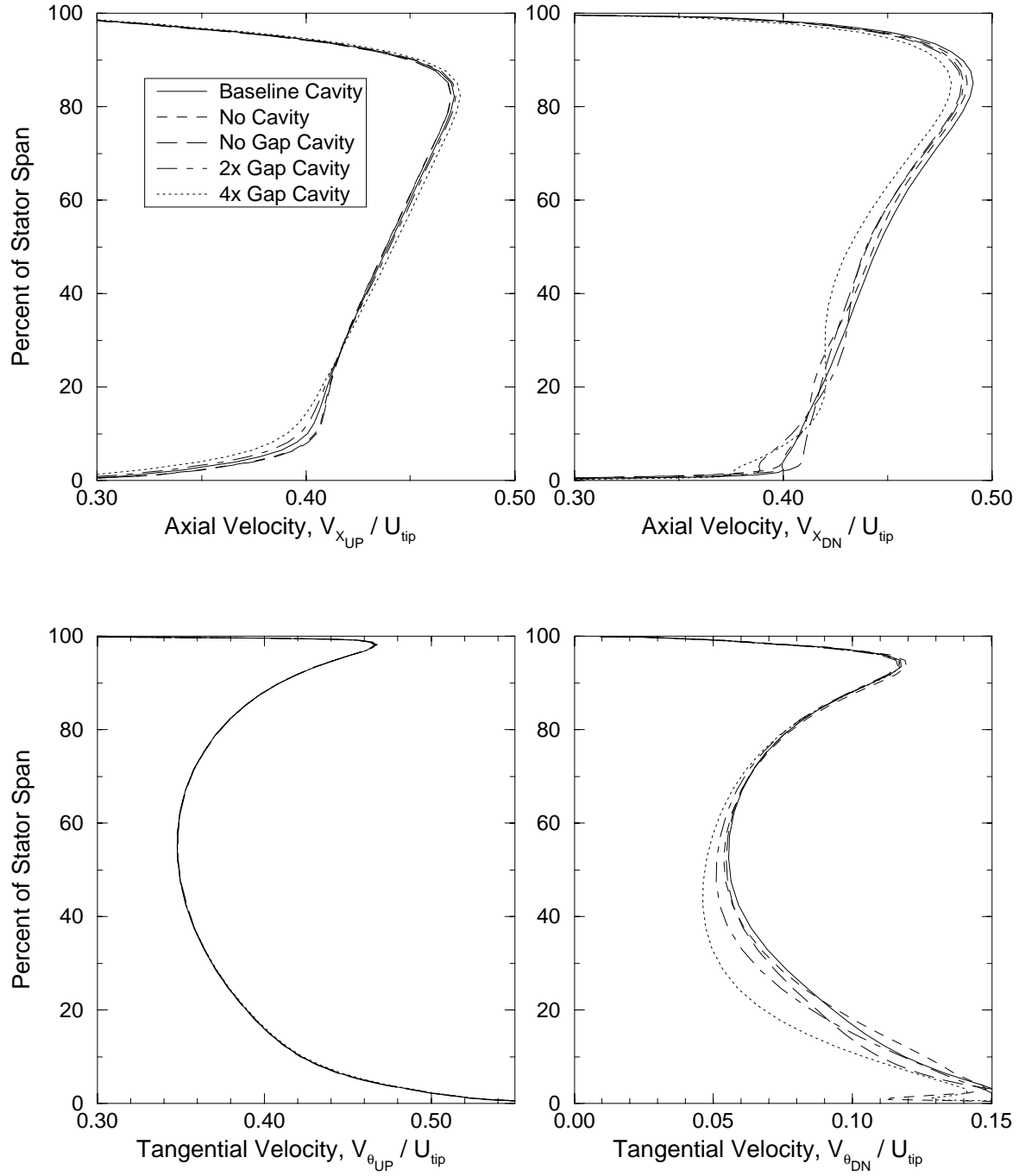


Figure 4.16: Radial profiles of axial and tangential velocities upstream and downstream of the stator blade for variations of the Tooth Gap parameter.

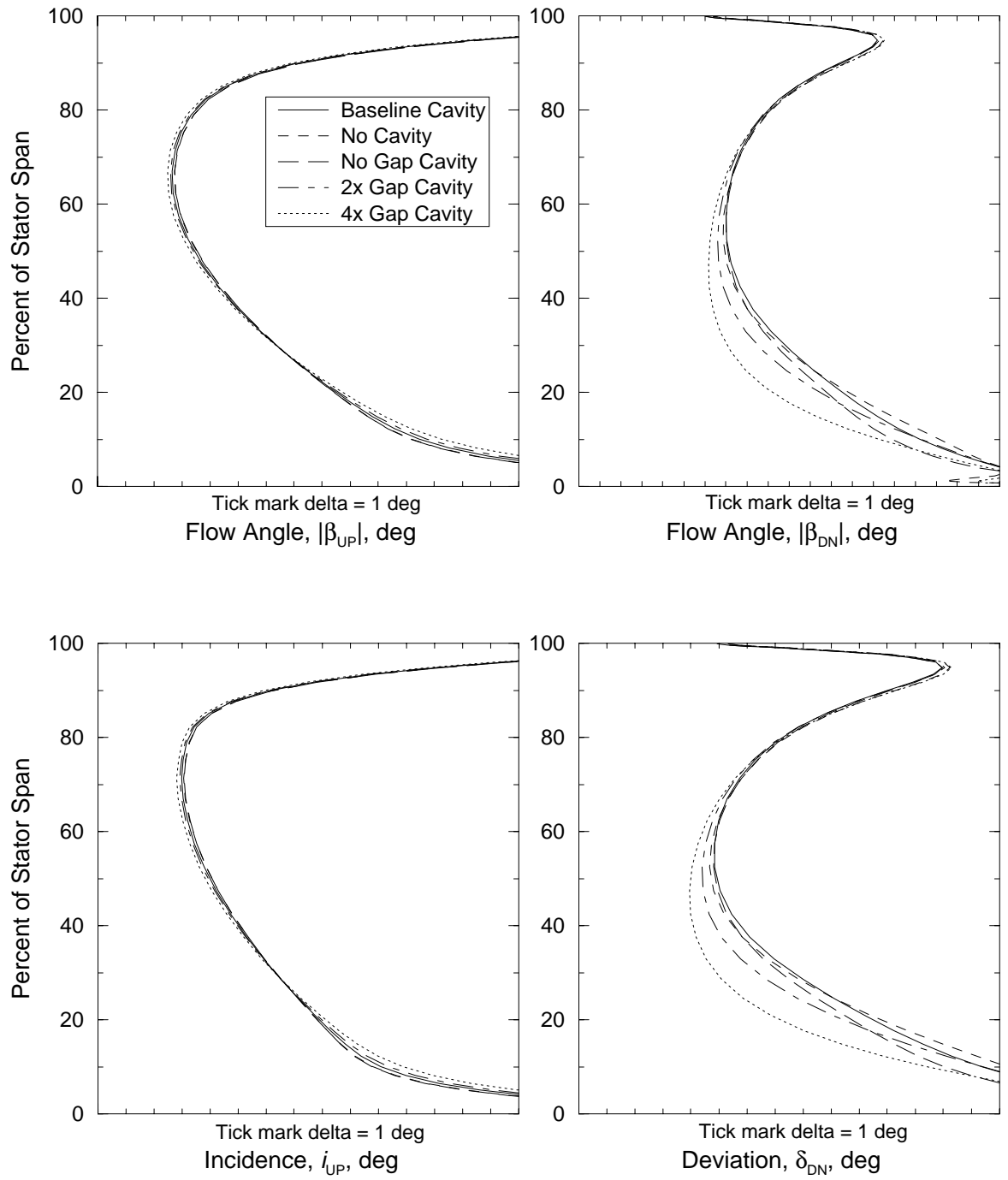


Figure 4.17: Radial profiles of flow angles upstream and downstream of the stator blade, and incidence and deviation for variations of the Tooth Gap parameter.

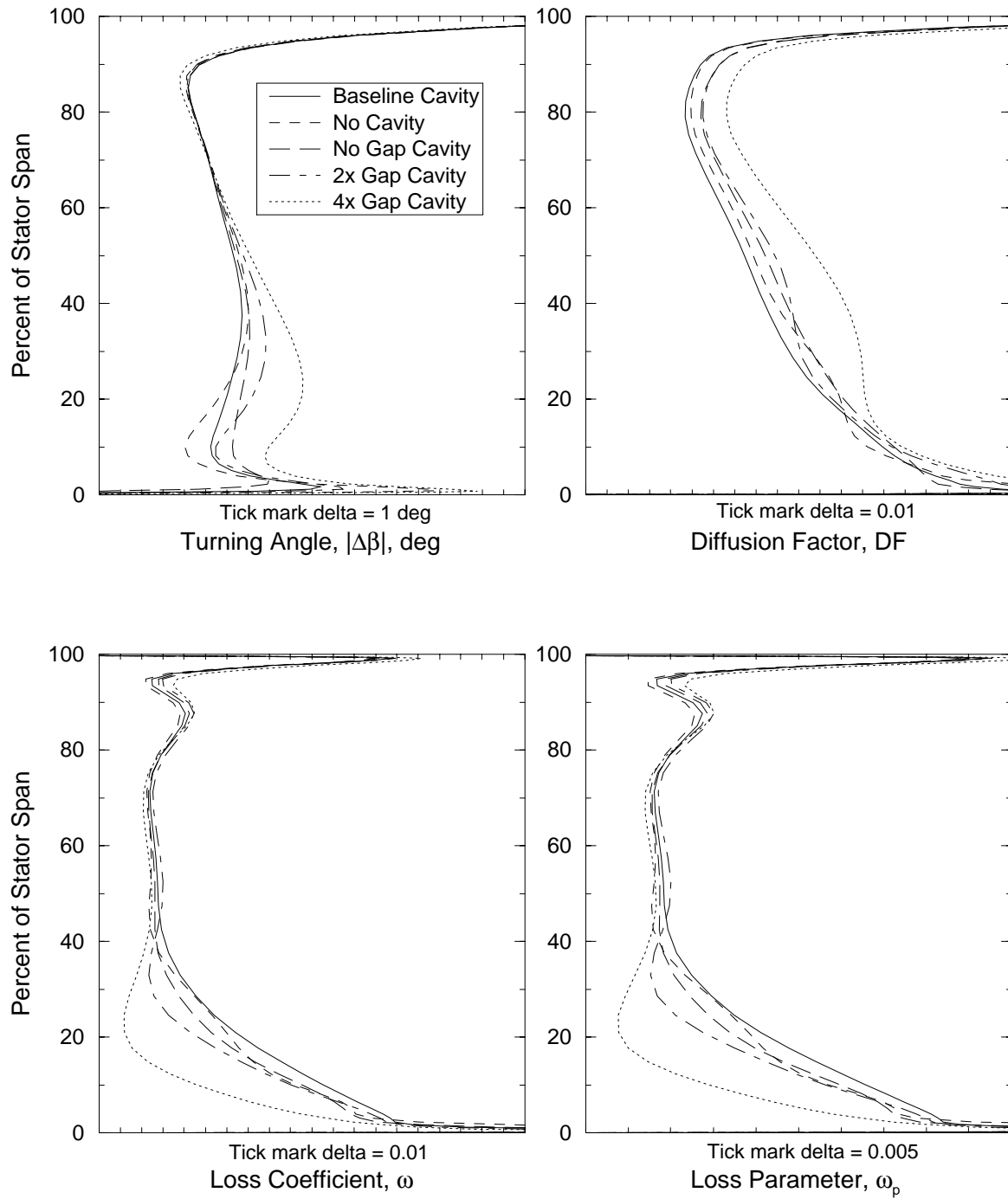


Figure 4.18: Radial profiles of stator blade performance parameters measured across the stator blade for variations of the Tooth Gap parameter.

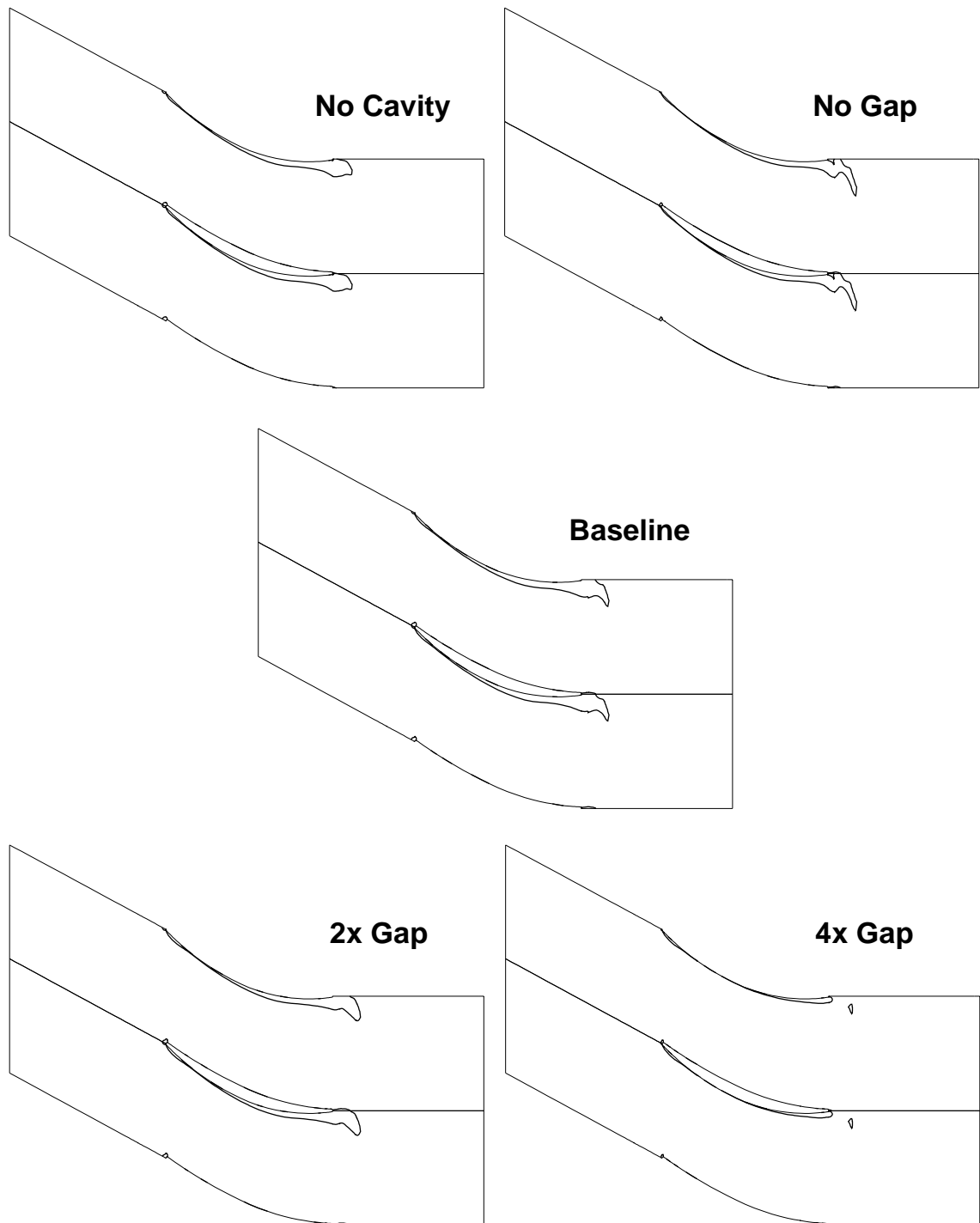


Figure 4.19: Zero axial velocity contour line at the near-hub location for the No Cavity, No Gap, Baseline, 2x Tooth Gap, and 4x Tooth Gap configurations.

4.8.1 Comparison with Current Design Methods

In order to compare *ADPAC* results with current secondary flow design tools, a series of runs was completed using BC88 [33], a computer model which solves the flow through a circuit with various restrictions such as seal cavities. The current baseline triple-knife labyrinth seal cavity was modeled using BC88 for several different knife gap clearances. All input to the BC88 code was taken from the 2-D seal geometry definition and the compressor design deck so as not to bias the BC88 answer by using *ADPAC* results. The resulting predicted leakage rates were plotted as a percentage of the main passage flow and compared to the *ADPAC* results from the tooth gap parameter study in Figure 4.20. Good agreement was found between the *ADPAC* results and the BC88 model. The triple-knife *ADPAC* results fell slightly below the BC88 prediction. Previous single-knife seal cavity *ADPAC* results from the High-Speed Compressor Study, also presented in Figure 4.20, show a larger reduction in leakage when more knives are added. Both BC88 and *ADPAC* showed that at very large knife clearances, the number of knives becomes secondary to the size of the clearance.

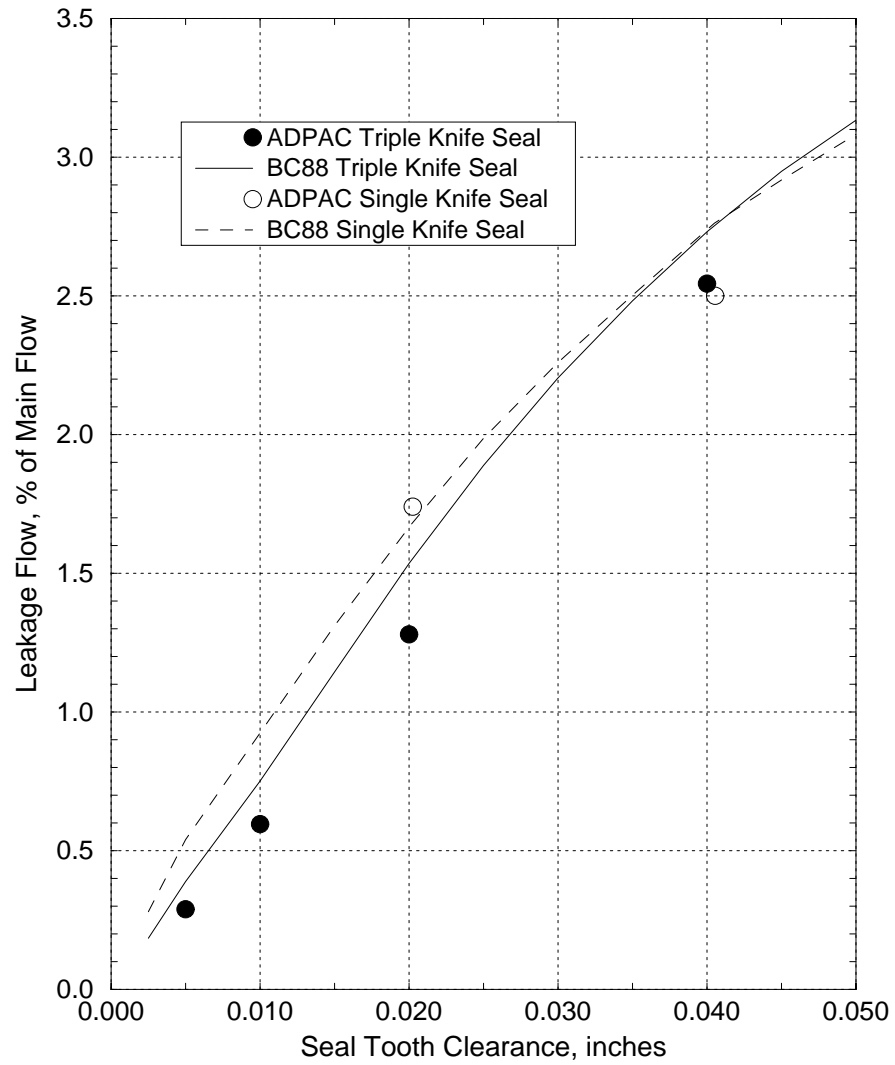


Figure 4.20: Leakage flow rate comparison between 3-D *ADPAC* seal cavity solutions and BC88 seal cavity solutions.

4.9 Lower Wheel Speed Cavity Case

From the High-Speed Compressor Study, the exit tangential velocity out of the upstream cavity trench was identified as a critical variable affecting the stator blade performance. In order to confirm this finding, a baseline geometry case with a lower hub rim speed was tested. The inlet conditions to the stator blade in this case (i.e., velocity triangles) were **not** changed; the change in rotational speed was only used to control the exit tangential velocity of the seal cavity flow. The rotational speed was reduced to 58% from the baseline value so that the exit flow from the seal cavity trench would more closely match the main flow swirl velocity.

The seal cavity mass flow for the Lower Wheel Speed case was 0.56% of the main passage mass flow, whereas the Baseline case leaked at 0.60%. This weak correlation of seal cavity mass flow with rotational speed corresponds with earlier experimental findings [2]. The tangential velocity of seal cavity flow exiting the upstream cavity trench for the Lower Wheel Speed case slowed significantly in absolute value from the Baseline case value, but remained near 75% of hub wheel speed.

In order to visualize the effect of the seal cavity flow interacting with the main passage flow, particle traces were released in the upstream cavity trench at the hub surface in both the Baseline case and the Lower Wheel Speed case. Black and white particle traces were released in alternating blade passages and are shown in Figures 4.21 and 4.22. The particle traces in the Baseline case (Figure 4.21) exited the upstream seal cavity trench with enough tangential velocity that they traveled up along the pressure side of the stator blade. Those traces released near the upstream trench edge next to the rotor wheel actually traveled into the neighboring blade passage. When the particle traces exit with a lower tangential velocity as in the Lower Wheel Speed case (Figure 4.22), the traces remained very near the hub surface and did not travel onto the pressure side of the blade. (Particle traces were useful in obtaining a qualitative picture of the flowfield; however, the traces were released at grid points clustered at the hub and may not reflect where the majority of the flow traveled.)

As the seal cavity flow re-entered the main flow passage, a total temperature rise and total pressure loss were associated with the seal cavity flow. This introduction of low axial momentum flow with an increased total temperature from the seal cavity changed the distribution of total pressure and total temperature along the stator span. Figure 4.23 shows the spanwise distribution of changes in total pressure and total temperature calculated across the stator blade, using measuring stations UP and DN, for the No Cavity case, the Baseline case, and the Lower Wheel Speed case. The total pressure values were non-dimensionalized by $\rho U_{tip}^2/2$ and the total temperature values by the rise in total temperature through the upstream rotor blade. When no seal cavity was present (dotted line), the stator blade experienced approximately a 2 to 3 psia drop in total pressure and a redistribution of total temperature with no net gain; since without the rotating cavity no mechanism existed to add energy to the flow. When the baseline seal cavity was added (solid line), a slightly larger pressure loss was calculated; however, a much larger increase in total temperature (almost 20% of the total temperature rise through the upstream rotor) was found centered at

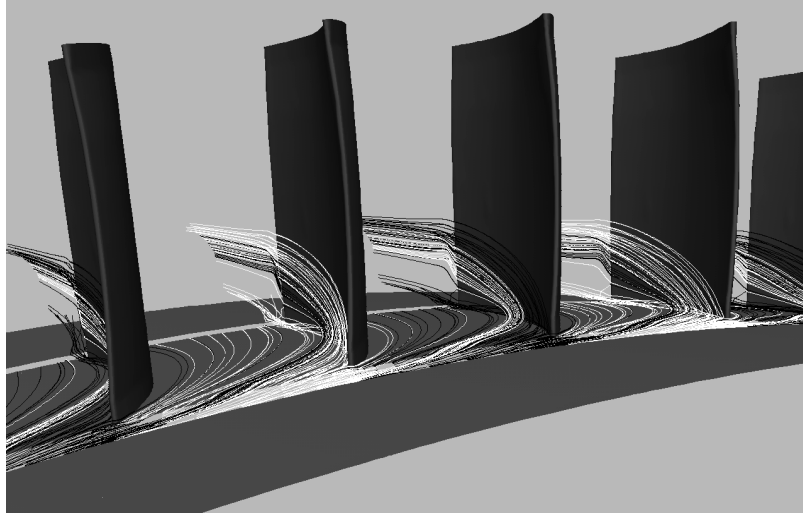


Figure 4.21: Alternating black and white passages of particle traces released in the upstream cavity trench for the Baseline case.

approximately 25% stator span. This spanwise location corresponded to the region where the particle traces left the stator blade pressure side in Figure 4.21. When the baseline seal cavity rotational speed was slowed as in the Lower Wheel Speed case (dot-dash line), the seal cavity flow stayed near the hub and a larger total pressure loss was calculated in the lower 10% span and a corresponding total temperature rise in the same spanwise region.

Since in the Lower Wheel Speed case the seal cavity leakage flow remained in the lower 10% span region through the stator blade, an effective contraction of the flow area occurred as the hub surface “seen” by the main flow extended further into the stream. The seal cavity flow near the hub caused a redistribution of axial velocity through the stator blade, as shown in Figure 4.24, with a large deficit in the lower 10% span and an offsetting increase in the upper portion of the blade to maintain a specified mass flow. The redistribution affected the flow angles and the stator blade performance parameters as shown in Figures 4.25 and 4.26. The diffusion factor distribution showed the lower 10% of the stator blade to be more heavily loaded while the upper 90% was unloaded relative to the Baseline case distribution. As the Lower Wheel Speed case has shown, the effect of exit tangential velocity out of the upstream cavity and where that flow goes is a major determining factor in the performance of the stator blade.

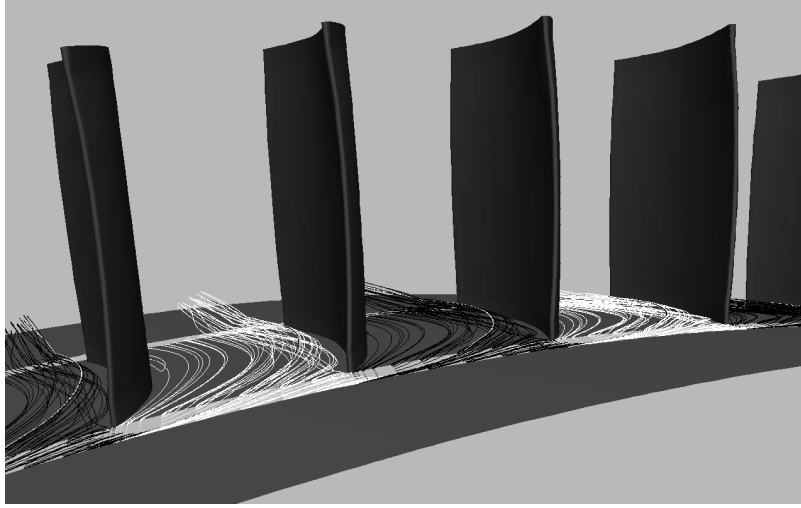


Figure 4.22: Alternating black and white passages of particle traces released in the upstream cavity trench for the Lower Wheel Speed case.

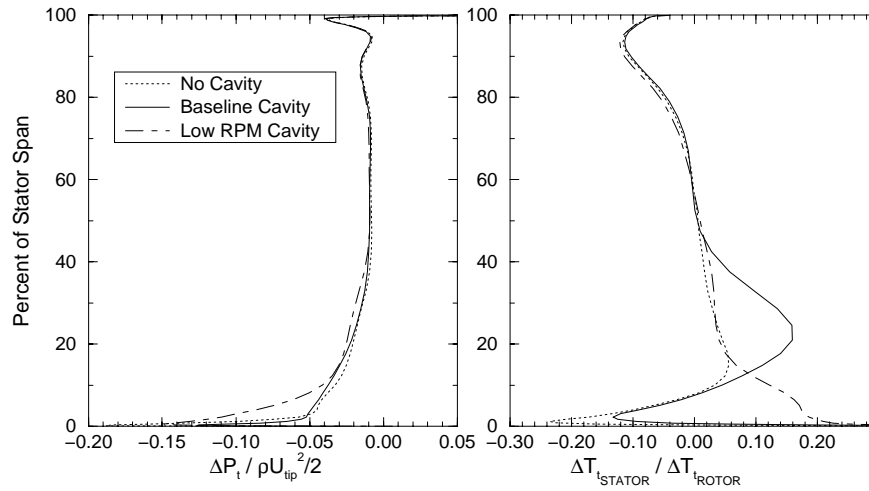


Figure 4.23: Comparison of radial profiles of change in total pressure and total temperature distributions across the stator blade between the No Cavity case, the Baseline case, and the Lower Wheel Speed case.

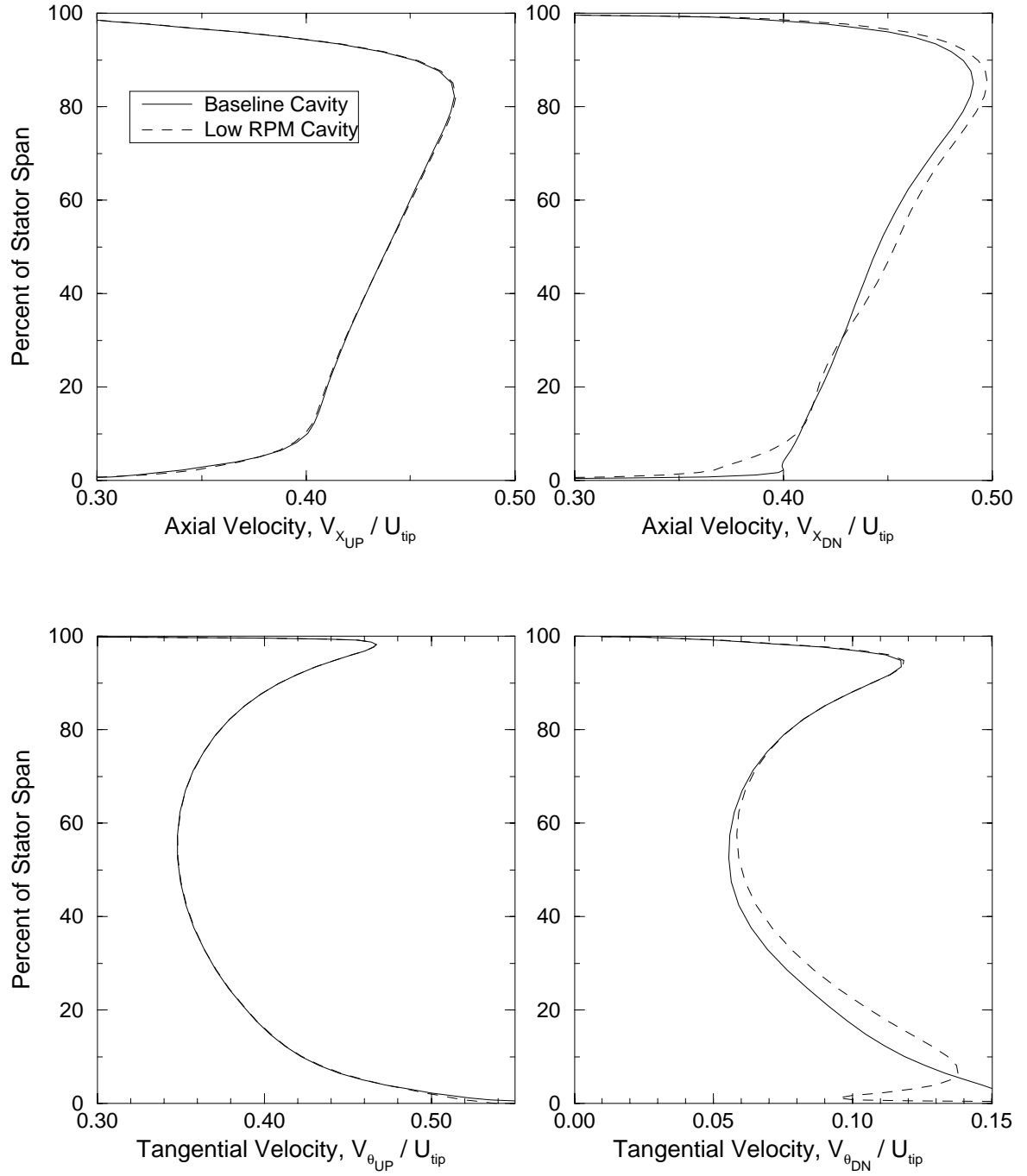


Figure 4.24: Radial profiles of axial and tangential velocities upstream and downstream of the stator blade for the Lower Wheel Speed case.

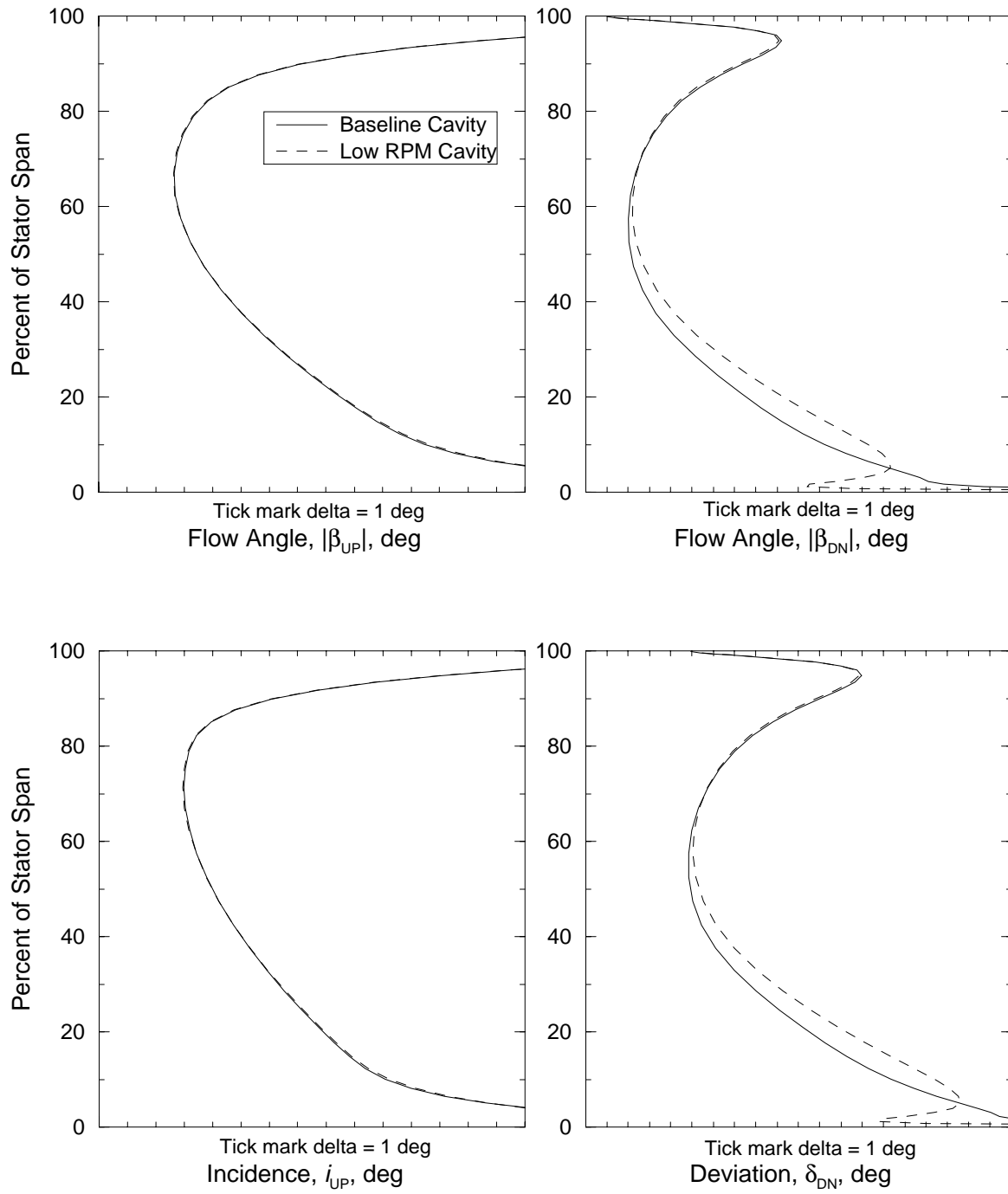


Figure 4.25: Radial profiles of flow angles upstream and downstream of the stator blade, and incidence and deviation for the Lower Wheel Speed case.

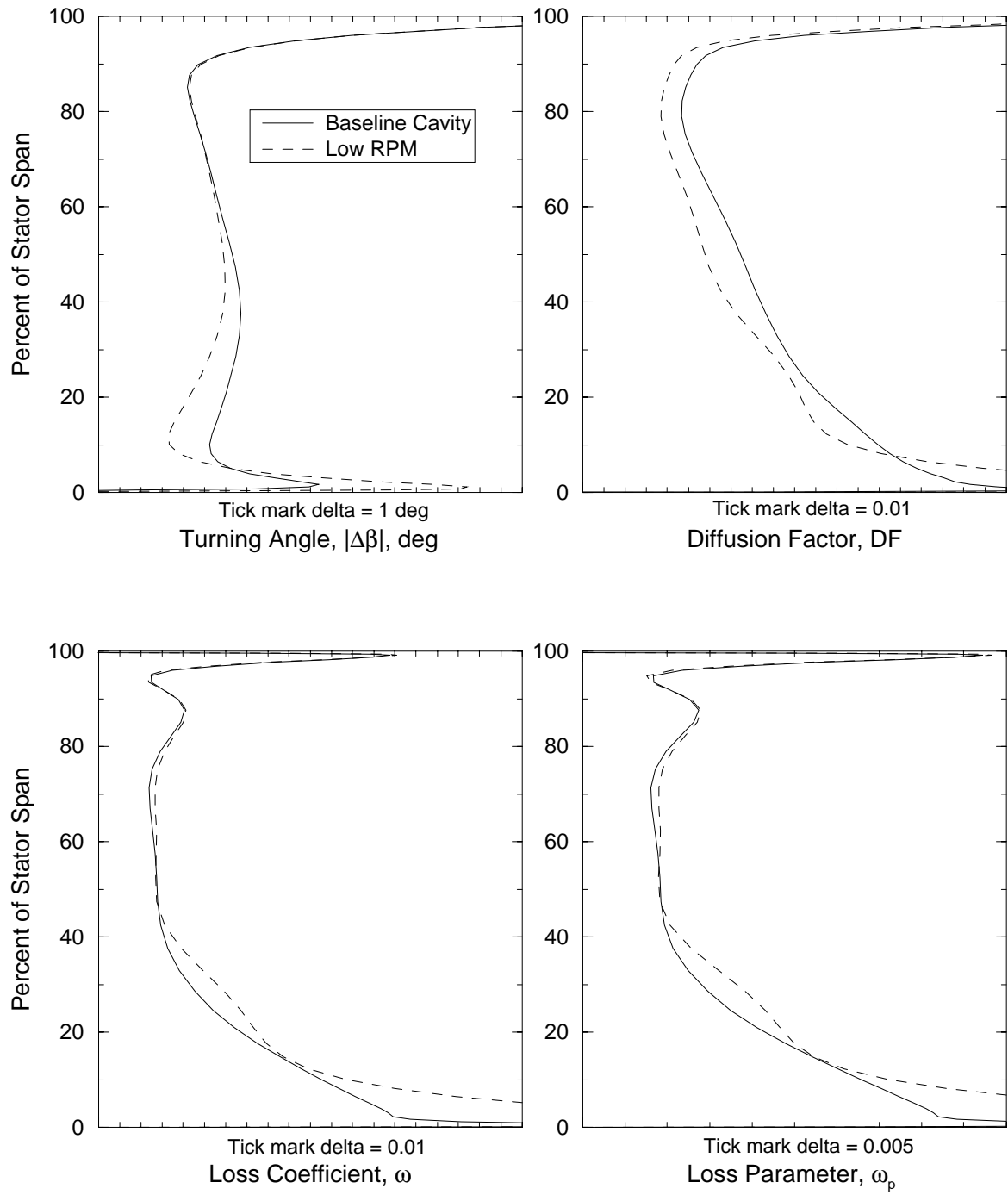


Figure 4.26: Radial profiles of stator blade performance parameters measured across the stator blade for the Lower Wheel Speed case.

4.10 Cavity Depth Parameter

The depth of the seal cavity was changed by $\pm 50\%$ of the baseline cavity depth as measured from the base of the stator land. Figure 4.27 shows the meridional meshes for the two cases along with the baseline. The depth of the seal cavity had a minor effect on the mass flow through the cavity; as the cavity became deeper, slightly more mass flow passed over the knife seal at the same clearance.

Particle traces from an axisymmetrically-averaged solution are shown for the three cases in the Cavity Depth parameter study in Figure 4.28. As the cavity depth was increased, more secondary vortices were formed in the lower section between the knife seals. The increase in leakage mass flow with increasing cavity depth may be the result of less compression on the main rotating vortices filling the majority of the space between the knife seals.

Figures 4.29, 4.30, and 4.31 show the radial profiles for velocities, flow angles, and performance data, respectively, for the Cavity Depth parameter solutions. In all the figures, there was very little change between the three configurations, signifying from these results that cavity depth had little to no effect on the main flowpath. Pitchwise distributions for the upstream and downstream trenches (not shown in this report) also showed little variation when the cavity depth was changed.

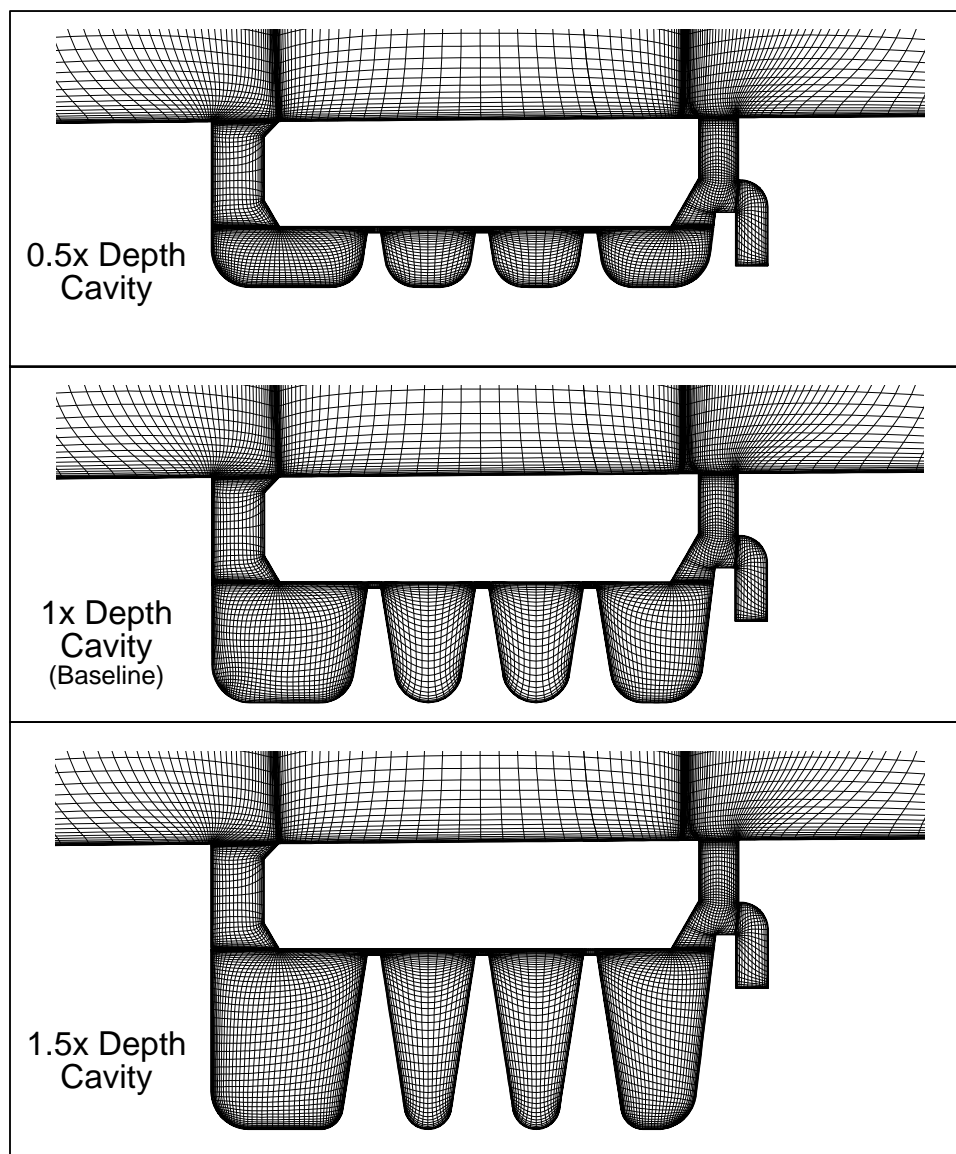


Figure 4.27: Meridional plane grids showing the variation of the Seal Cavity Depth parameter.

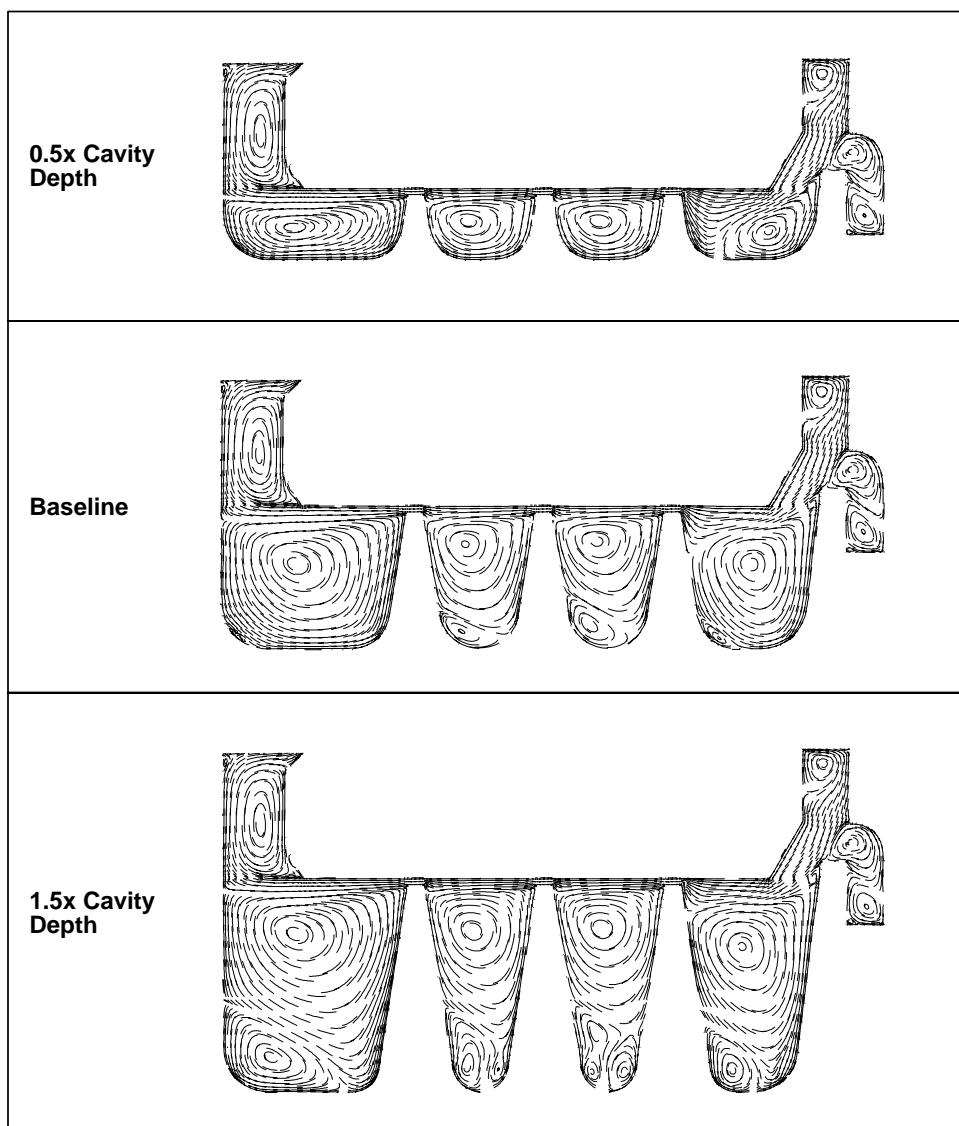


Figure 4.28: Axisymmetrically-averaged particle traces within the seal cavity for the Cavity Depth parameter series.

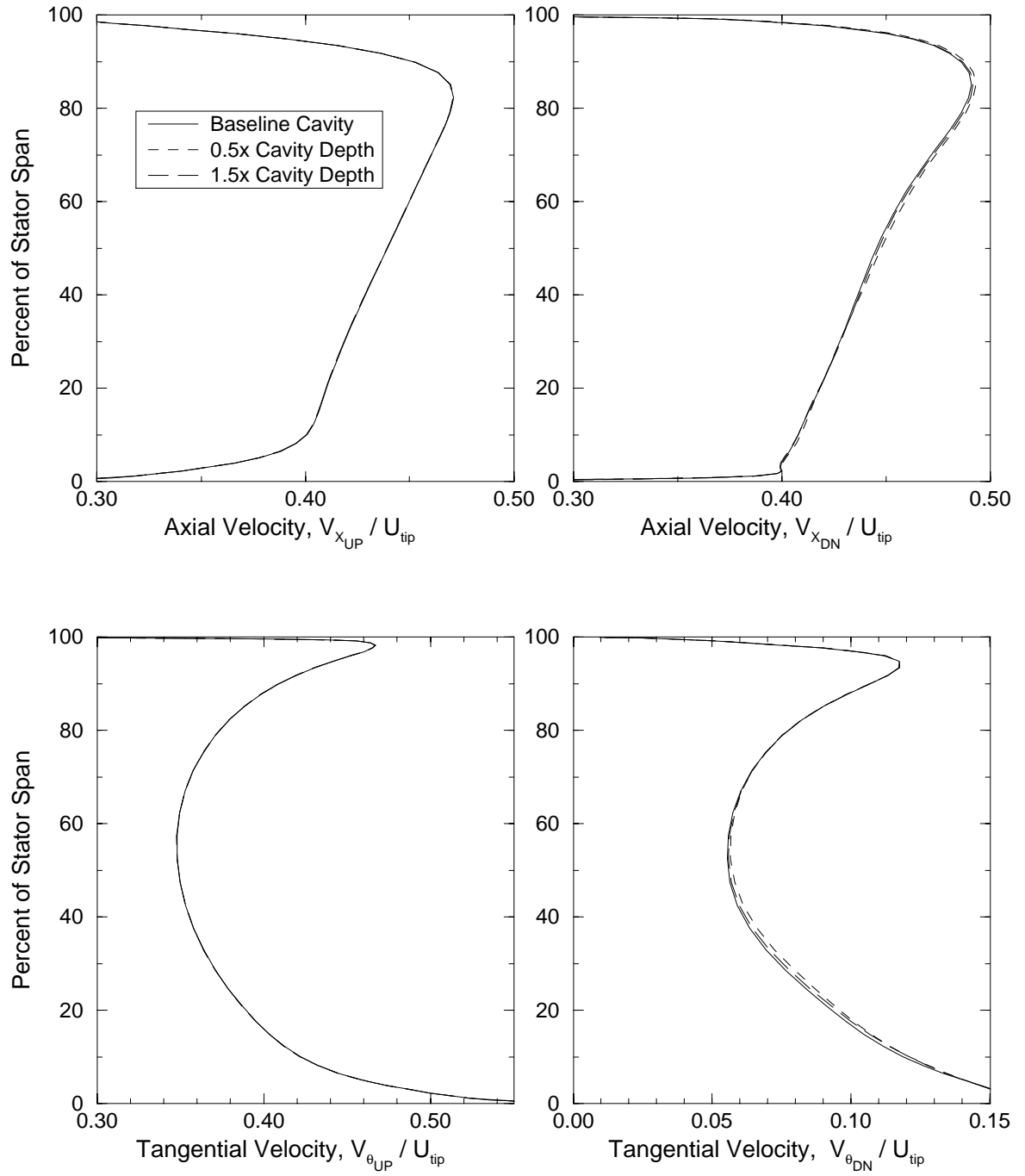


Figure 4.29: Radial profiles of axial and tangential velocities upstream and downstream of the stator blade for variations of the Cavity Depth parameter.

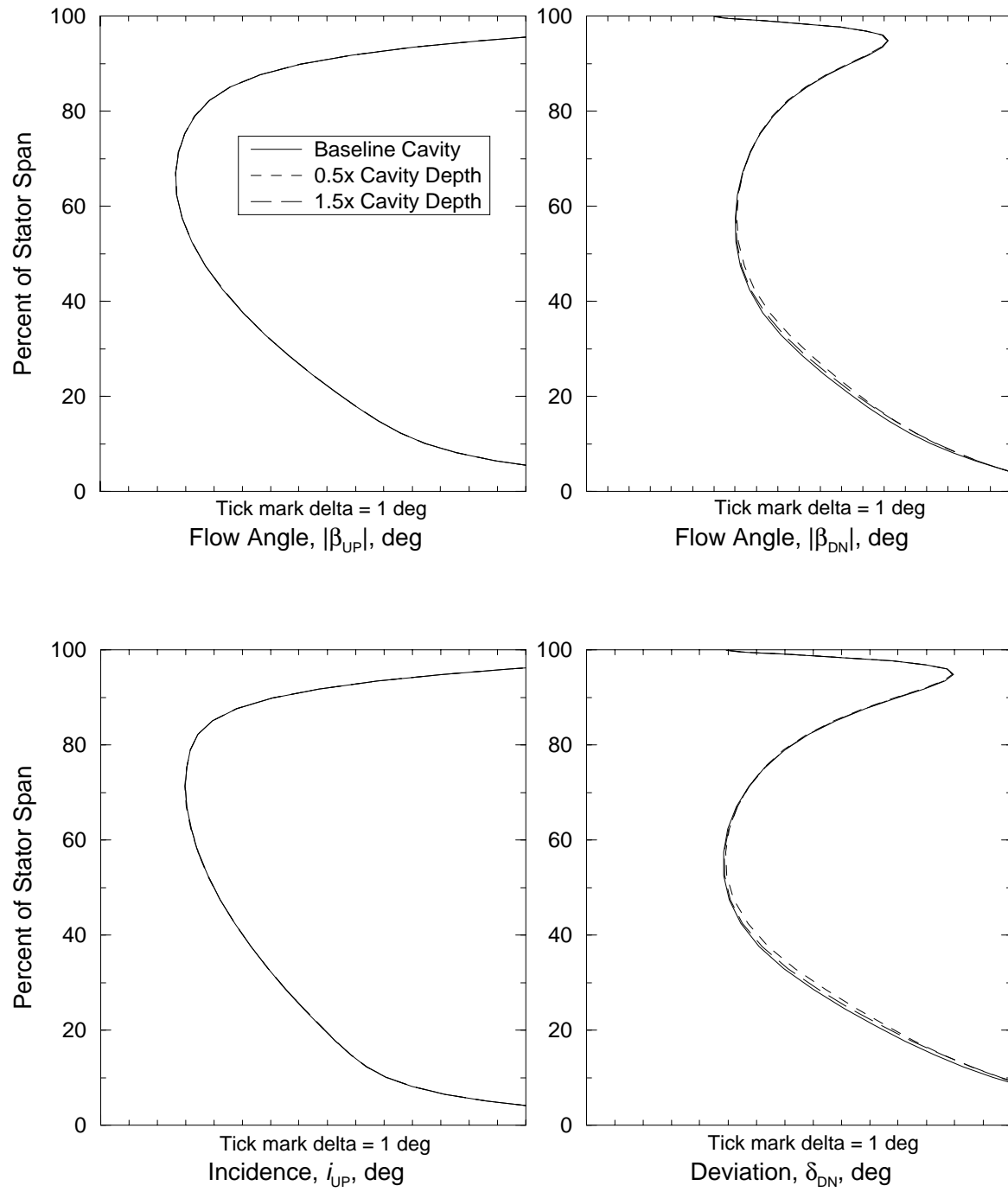


Figure 4.30: Radial profiles of flow angles upstream and downstream of the stator blade, and incidence and deviation for variations of the Cavity Depth parameter.

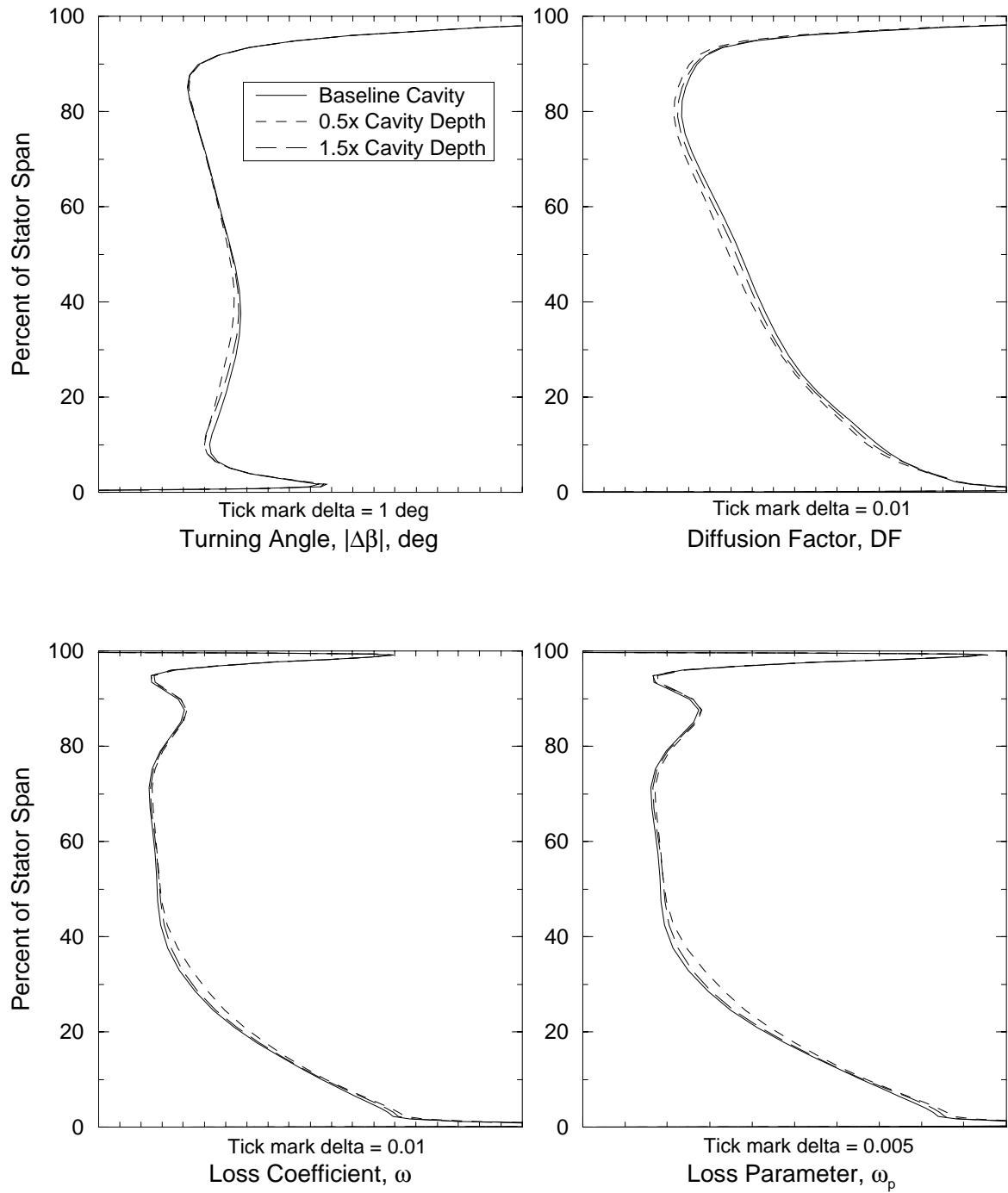


Figure 4.31: Radial profiles of stator blade performance parameters measured across the stator blade for variations of the Cavity Depth parameter.

4.11 Hub Radial Mismatch Parameter

The baseline configuration has essentially a straight line for the hub flowpath definition. The alignment of the hub flow path from rotor wheel to stator land was considered an important parameter that had a direct impact upon the interface region between the stator main flow and the seal cavity flow, Figure 4.32 shows the extent of the radial shift (5% stator span) of the hub flowpath for the cases examined in this study. This figure shows the changes applied to both the upstream and downstream cavity trench regions; however, four separate cases were run: raised hub upstream, lowered hub upstream, raised hub downstream, and lowered hub downstream. The hub offset of 5% stator span was intentionally large in order to amplify the effect of hub radial mismatch; it was recognized that this large value of offset was **not** representative of any offset that might occur in current high-speed compressors.

Changing the radial mismatch of the hub surface across the upstream or downstream trench had a significant effect on the mass flow through the seal cavity. When the rotating hub was raised above the stator land hub radius either upstream or downstream, the mass flow through the cavity increased slightly. Conversely, when the hub was lowered below stator land hub radius, the seal cavity mass flow was reduced slightly. This was the result of the main flow either “jumping” the seal cavity trench (i.e., backward facing step) or impacting and stagnating against the hub flowpath raised into the flow field (i.e., forward facing step); this is illustrated in the particle traces in Figures 4.33 and 4.34.

The particle traces for the upstream modifications are shown in Figure 4.33. When the upstream hub was raised, the main flow expanded over this “backward step” and this lower pressure allowed the rotating driven cavity in the upstream trench to move radially outward. This allowed more flow to be entrained in the main flow stream from the seal cavity which resulted in a larger mass flow through the seal cavity. The opposite happened when the upstream hub was lowered radially, the driven cavity was pushed back down into the trench, and the main flow stagnated against the stator land which increased the static pressure and decreased the driving potential for mass flow through the seal cavity.

Similar effects were found when the rotating hub radius was varied downstream of the stator blade. The particle traces for these configurations are shown in Figure 4.34. When the hub was raised, the flow stagnated against the downstream rotor wheel, thus forcing more flow through the seal cavity. Conversely, when the hub radius was lowered downstream, the flow traveling along the stator land expanded over the downstream trench opening; this lowering of the static pressure decreased the driving potential through the seal cavity, thereby reducing the mass flow across the knife seals.

The four different radial mismatch test cases can be paired into two sets: those simulating a converging annulus (raised hub downstream and lowered hub upstream) and those simulating a diverging annulus (raised hub upstream and lowered hub downstream). This effect is shown schematically in Figure 4.35 where the shaded area in each of the diagrams describes the general area trend affecting the main stator flow. Figures 4.36, 4.37, and 4.38 show radial profiles of velocities, flow angles, and

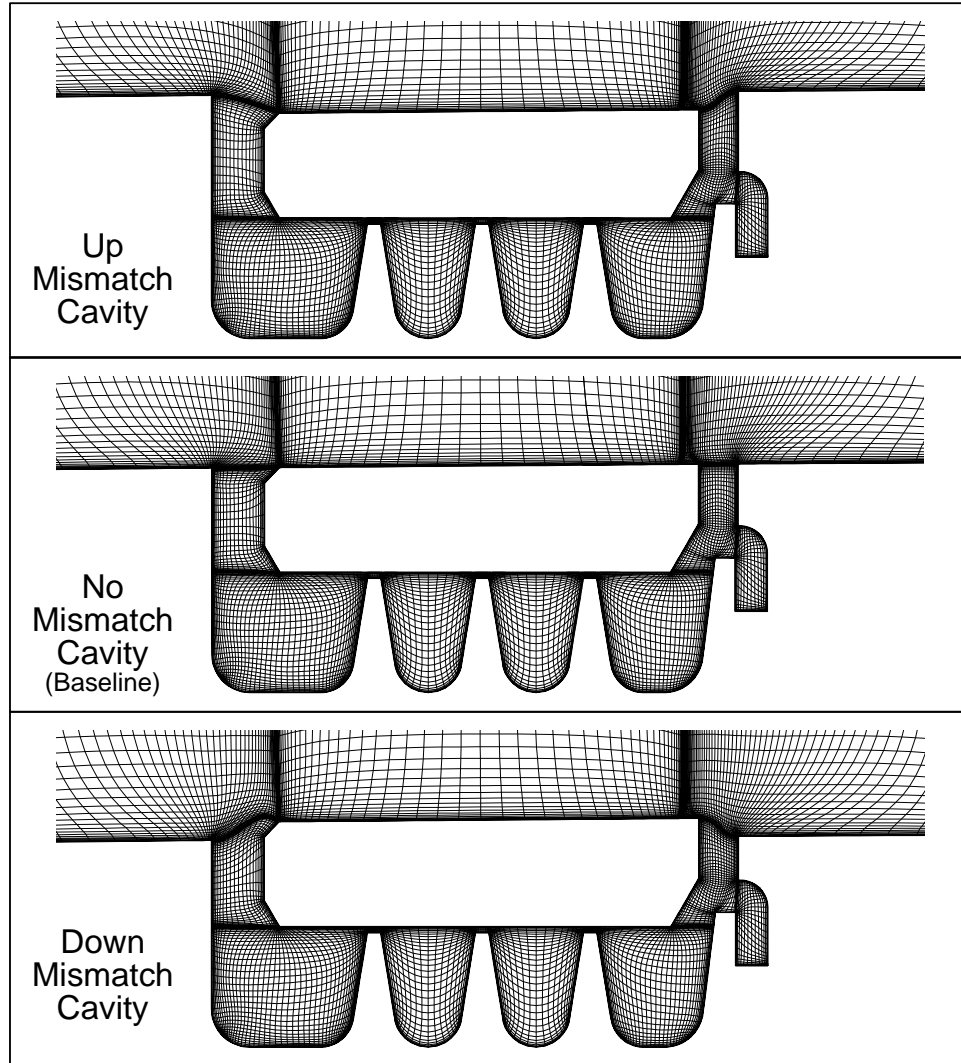


Figure 4.32: Meridional plane grids showing the variation of the Hub Radial Mismatch parameter.

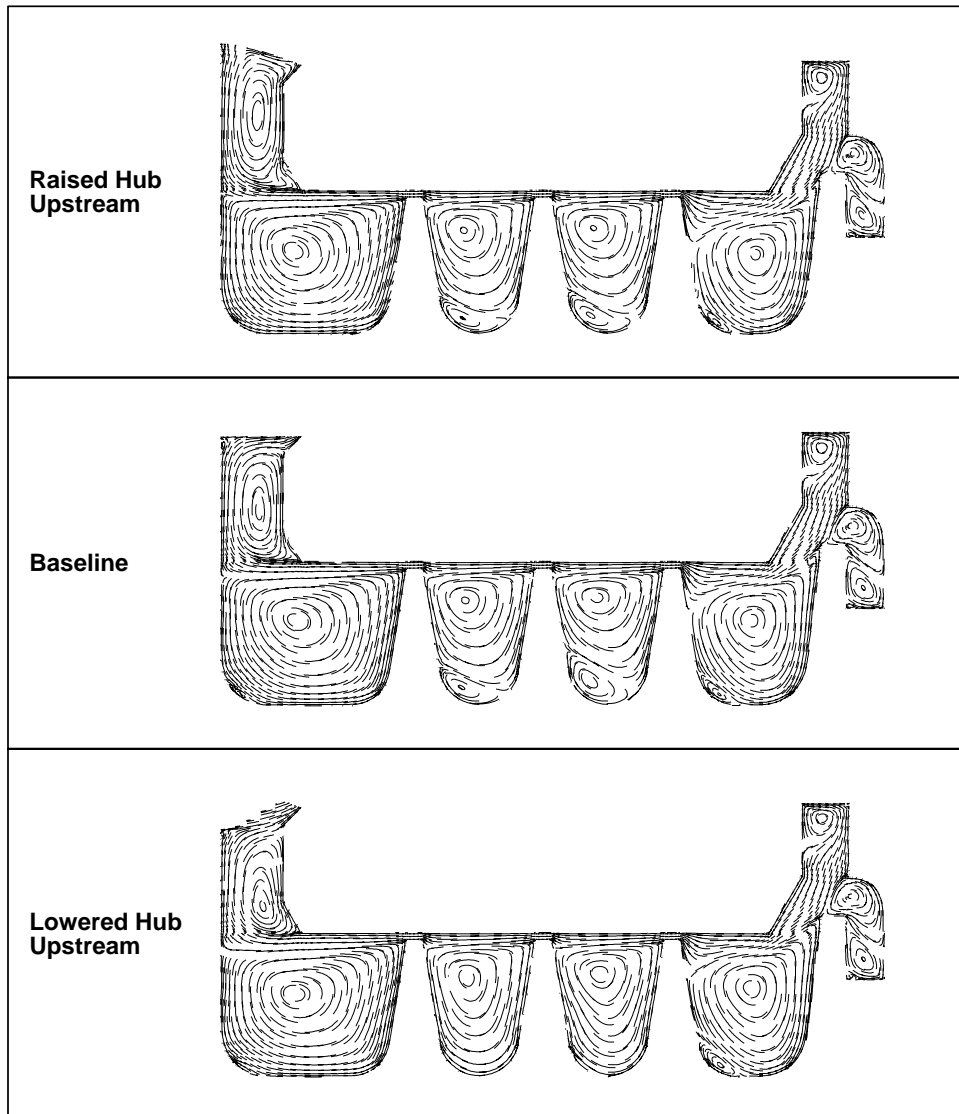


Figure 4.33: Axisymmetrically-averaged particle traces within the seal cavity for the Radial Mismatch parameter series upstream of the stator blade.

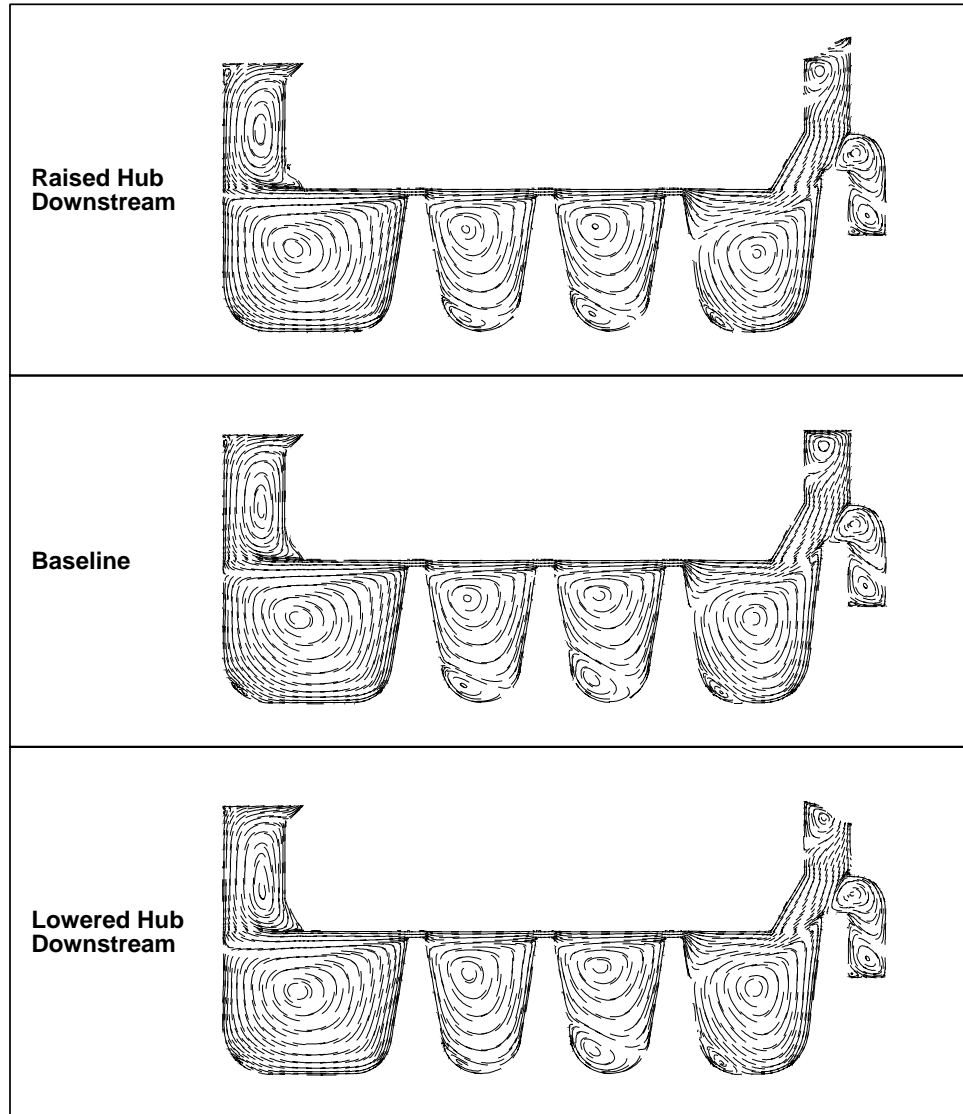


Figure 4.34: Axisymmetrically-averaged particle traces within the seal cavity for the Radial Mismatch parameter series downstream of the stator blade.

stator blade performance, respectively. Due to the constant mass flow exit boundary imposed, when the hub flowpath was raised upstream closing the annular flow region, the upstream axial and tangential velocities increased to maintain mass flow and flow inlet angle. Conversely, when the upstream hub was lowered, the upstream velocities decreased due to the opening up of the flow inlet annulus. A similar effect on the axial velocity distribution was also seen at the downstream data plane when the hub was raised and lowered downstream of the seal cavity trench. Radial mismatch cases having the same area trend (diverging or converging) appeared to align in the radial distributions of absolute turning and diffusion factor. The sharp decrease in blade loading shown in the diffusion factor distribution for the case with the downstream hub raised was attributed to the acceleration of the axial velocity component near the hub as it passed over the raised hub flow path.

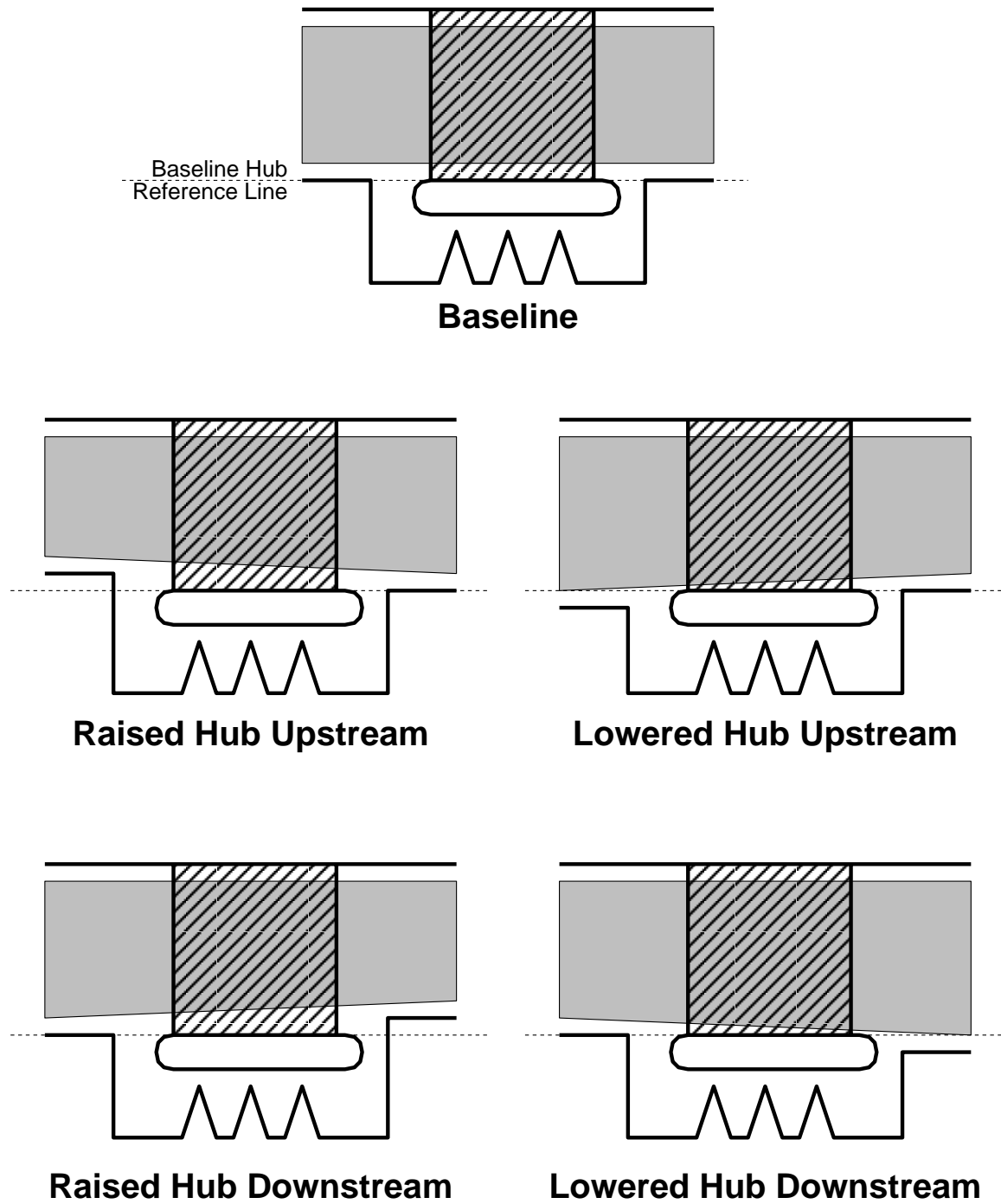


Figure 4.35: Schematic diagrams of the four different Radial Mismatch parameter cases showing the general area trend in the shaded area.

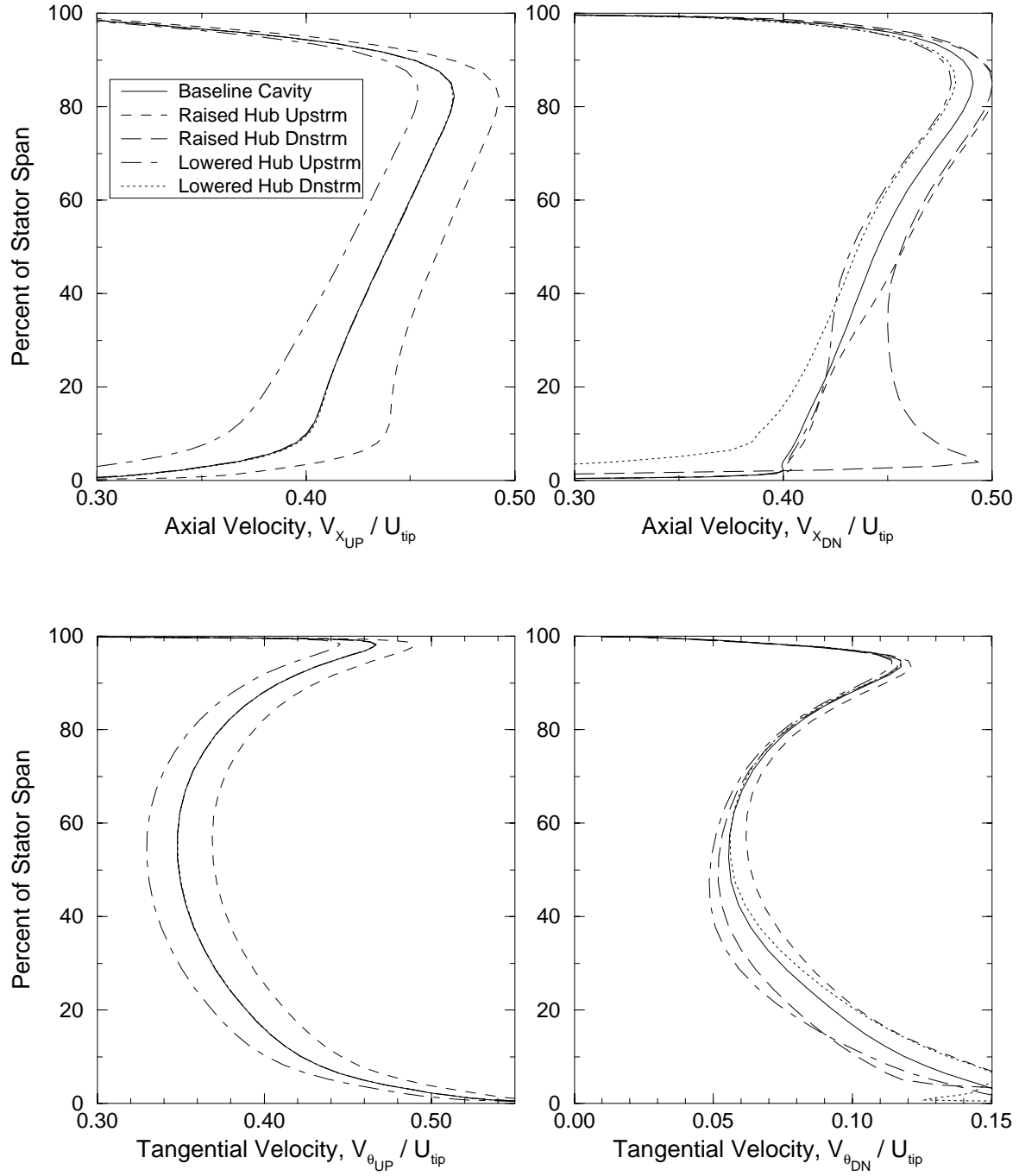


Figure 4.36: Radial profiles of axial and tangential velocities upstream and downstream of the stator blade for variations of the Hub Radial Mismatch parameter.

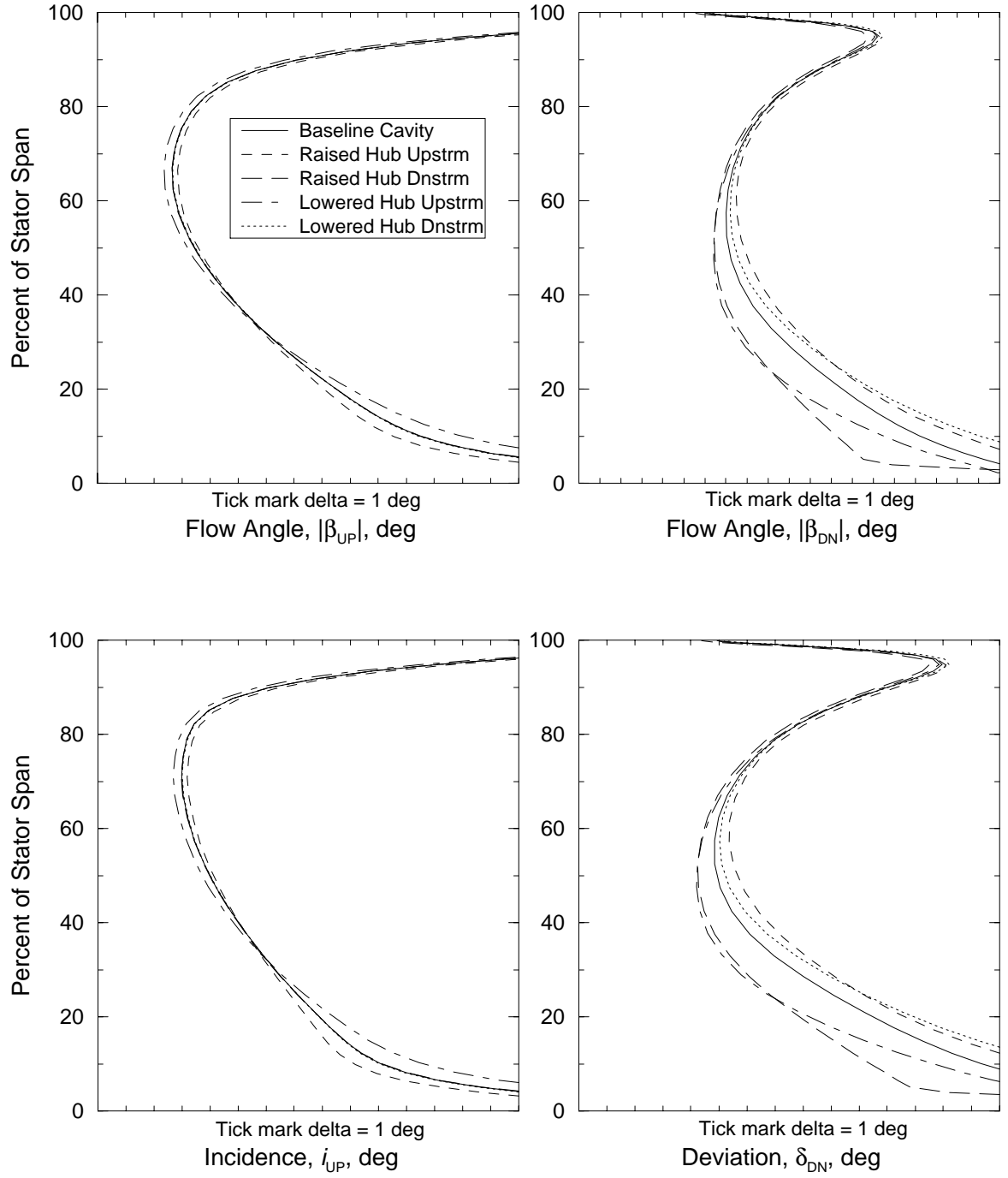


Figure 4.37: Radial profiles of flow angles upstream and downstream of the stator blade, and incidence and deviation for variations of the Hub Radial Mismatch parameter.

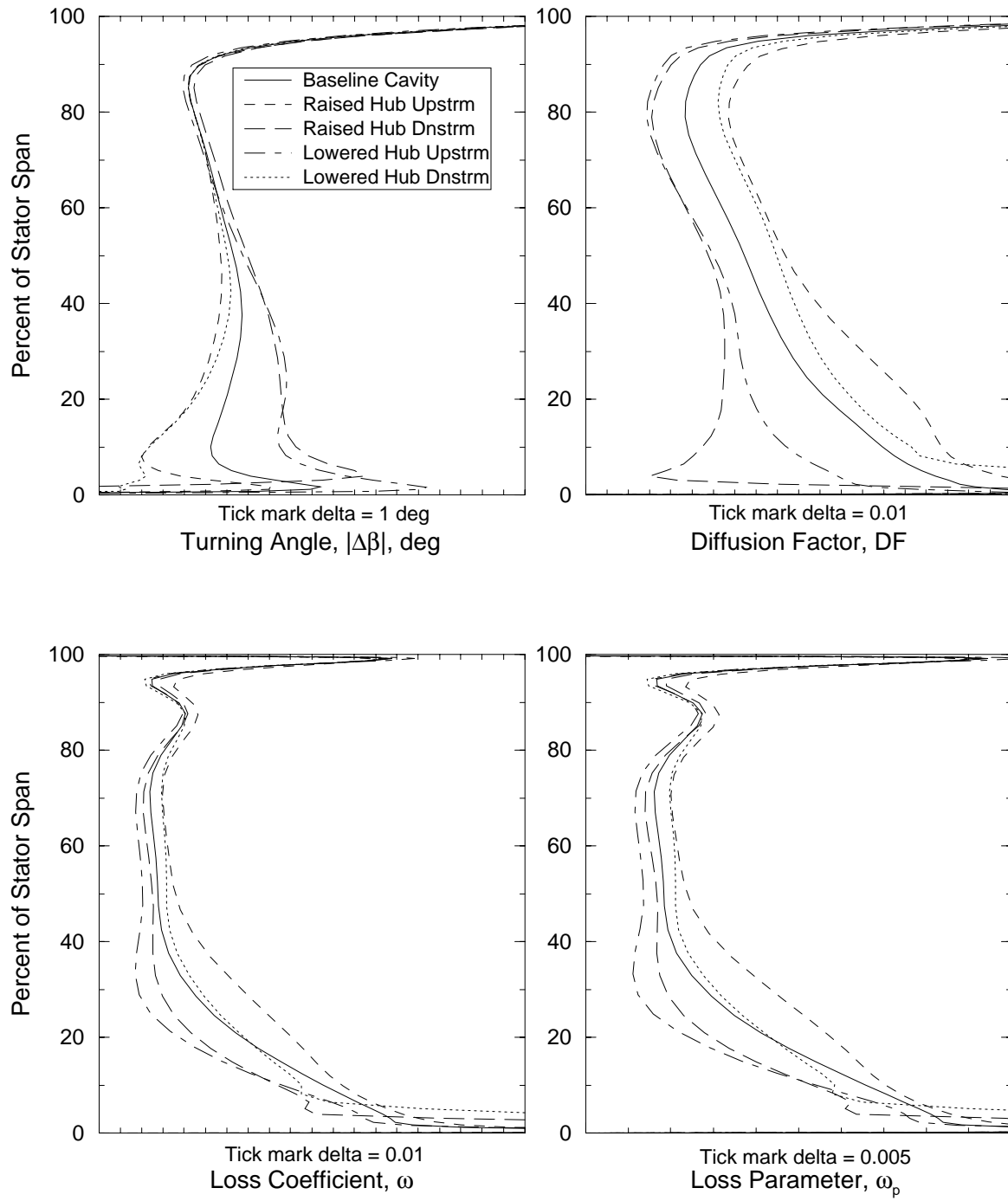


Figure 4.38: Radial profiles of stator blade performance parameters measured across the stator blade for variations of the Hub Radial Mismatch parameter.

4.12 Axial Trench Gap Parameter

The distances between the spinning rotor wheels and the stator inner-band are usually determined by the mechanical design considerations including thermal growth and machining tolerances. In order to investigate the influence in variation of this seal cavity dimension, two cases were tested: one with 20% larger axial trench gaps and one with 20% smaller gaps. Figure 4.39 show the geometry definition and meridional mesh slices for the two cases.

The seal cavity leakage flow for both cases did not differ much from the Baseline case. The particle traces released in the axisymmetrically-averaged cavity solutions revealed a seal cavity flow structure similar to the Baseline case. When the axial gaps were tightened, the driven cavity flow structures in the cavity trenches became compressed. This compression in the downstream trench caused the flow to be spun up tangentially faster by -5% span than the Baseline case as shown earlier in Figure 4.13. The opposite also appeared to be true; as the axial trench gaps were widened the rotating flow structures expanded and were not as compressed against the spinning downstream rotor wheel and therefore did not have as high tangential velocity at the same -5% span location. Despite this small difference, the upstream trench values for the tangential velocity for both cases were very similar to the Baseline case value.

Radial profiles for the Axial Trench Gap parameter solutions are shown in Figures 4.41, 4.42, and 4.43. There were no significant variations between the Axial Trench Gap parameter distributions and the Baseline case distributions. This indicated that the width of the axial gaps, while they should remain as small as possible to reduce the size of the compressor, did not have a significant effect on the stator blade flow over the range tested.

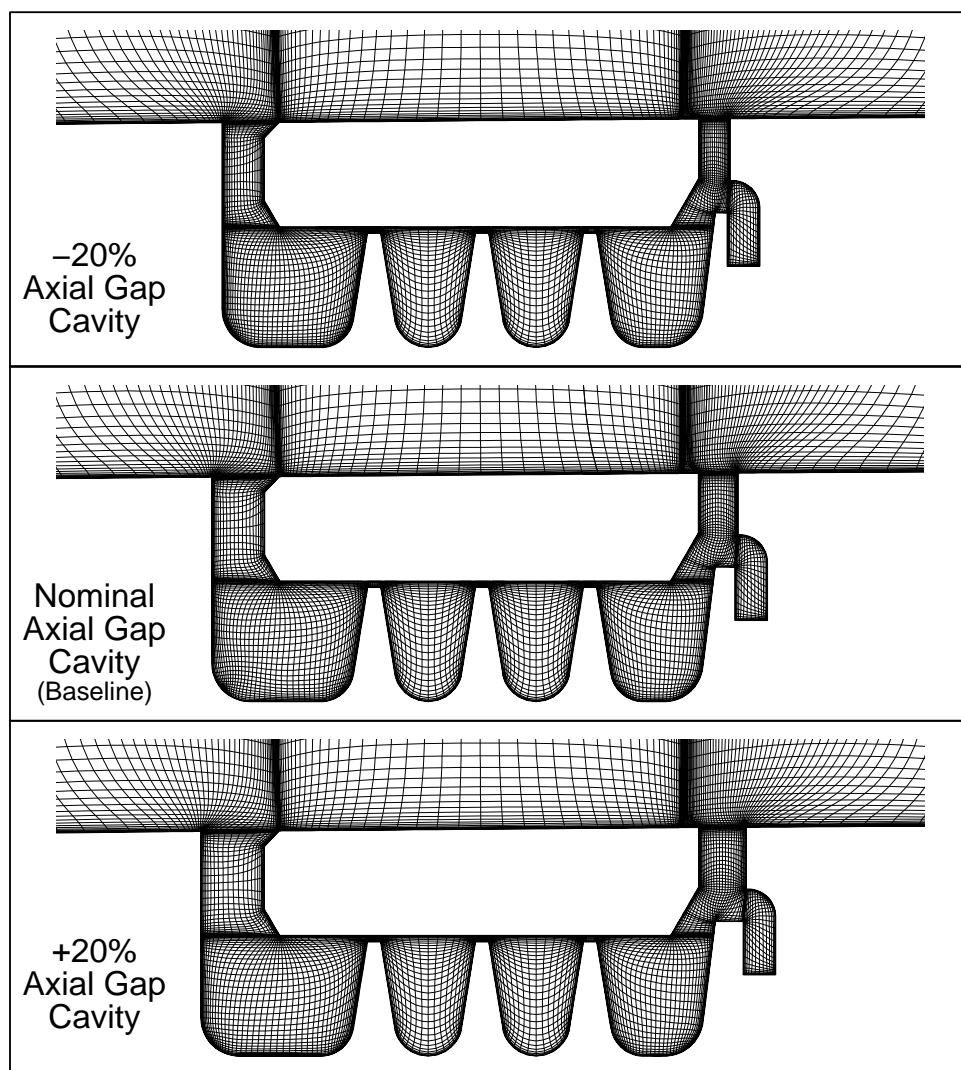


Figure 4.39: Meridional plane grids showing the variation of the Axial Trench Gap parameter.

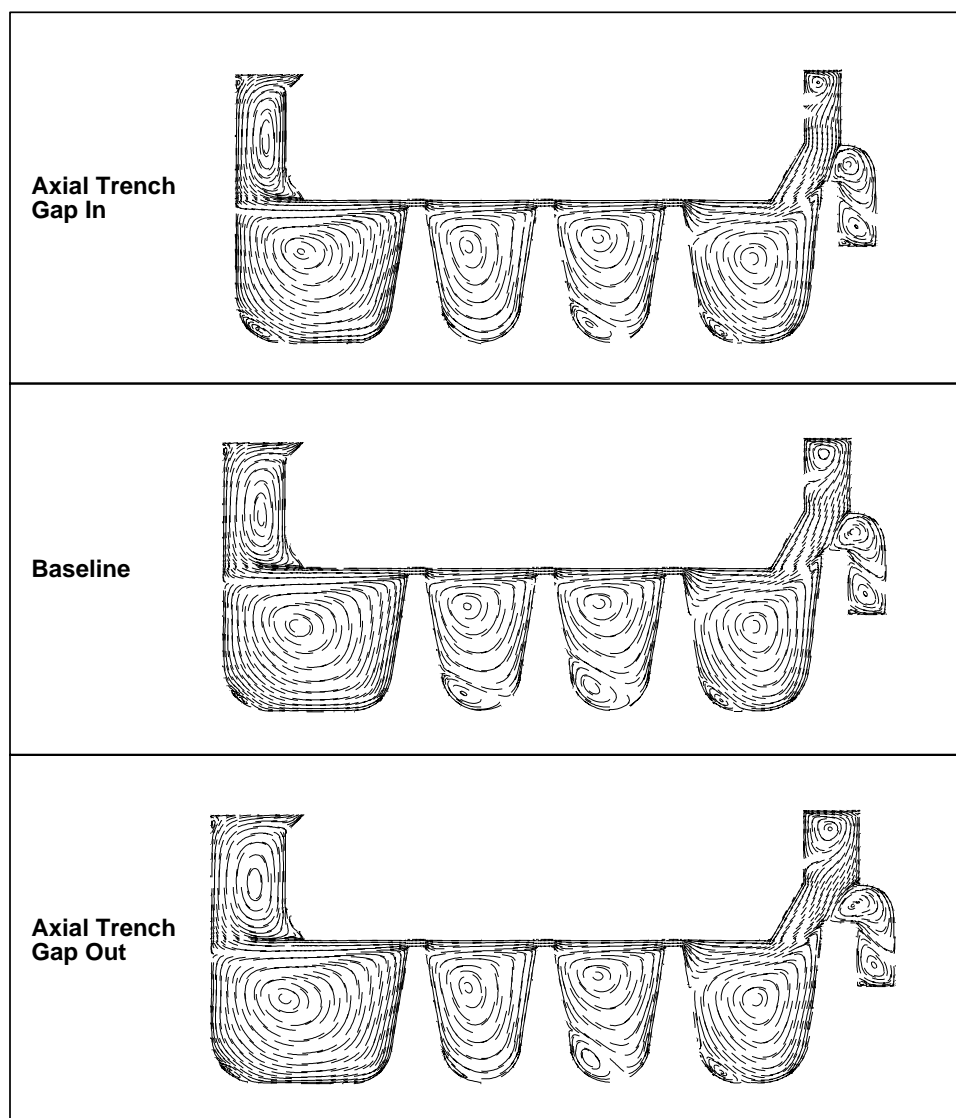


Figure 4.40: Axisymmetrically-averaged particle traces within the seal cavity for the Axial Trench Gap parameter series.

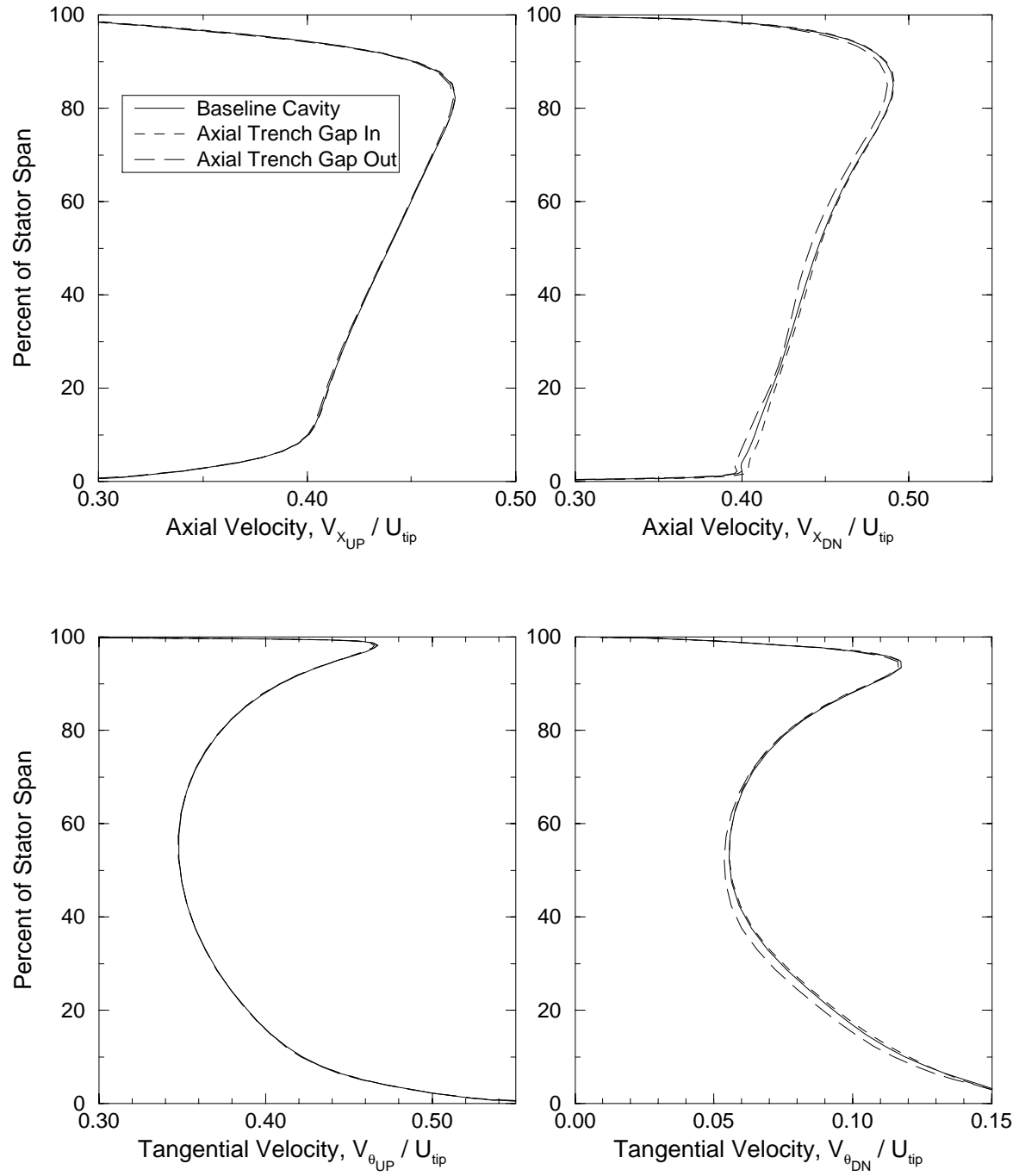


Figure 4.41: Radial profiles of axial and tangential velocities upstream and downstream of the stator blade for variations of the Axial Trench Gap parameter.

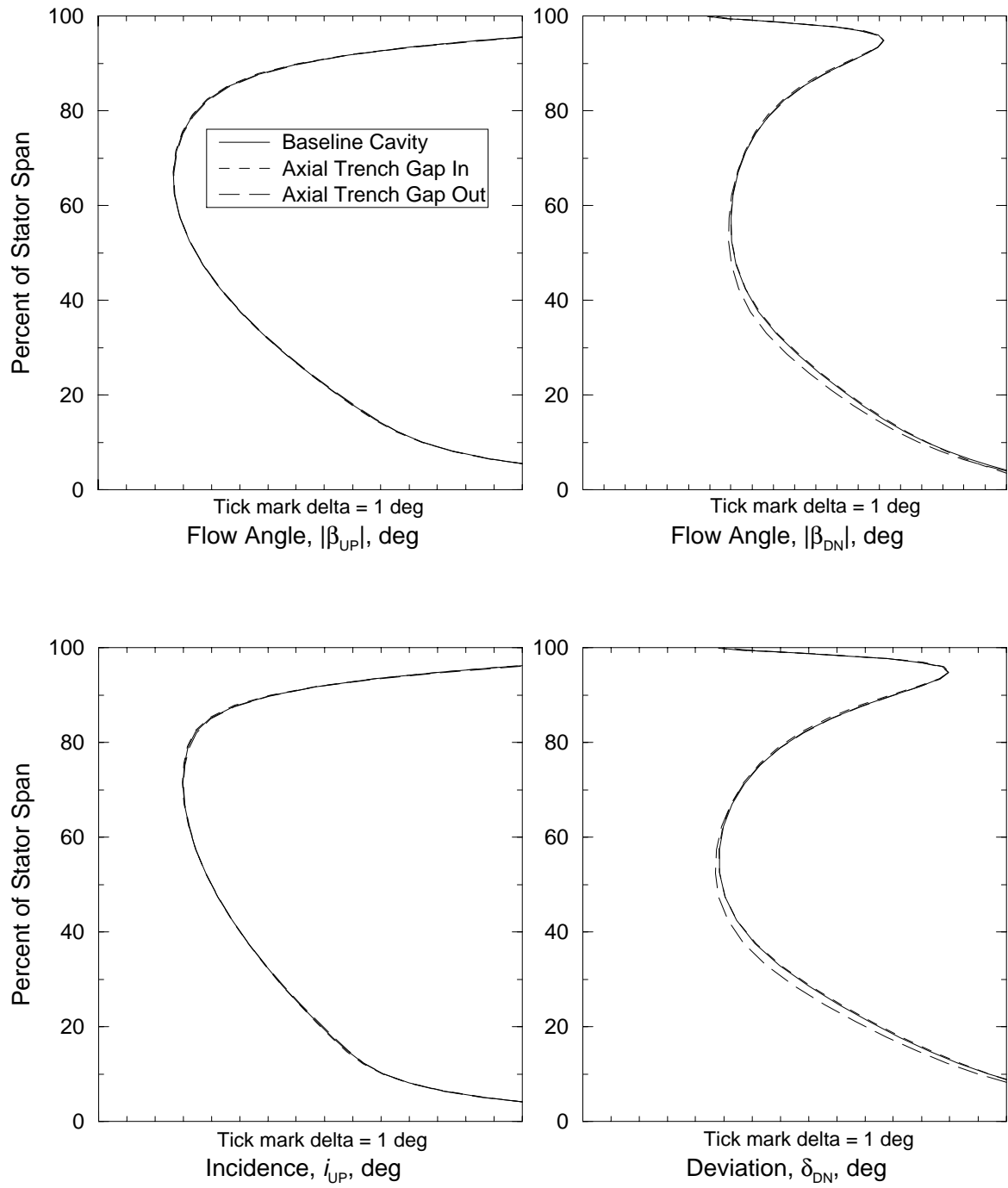


Figure 4.42: Radial profiles of flow angles upstream and downstream of the stator blade, and incidence and deviation for variations of the Axial Trench Gap parameter.

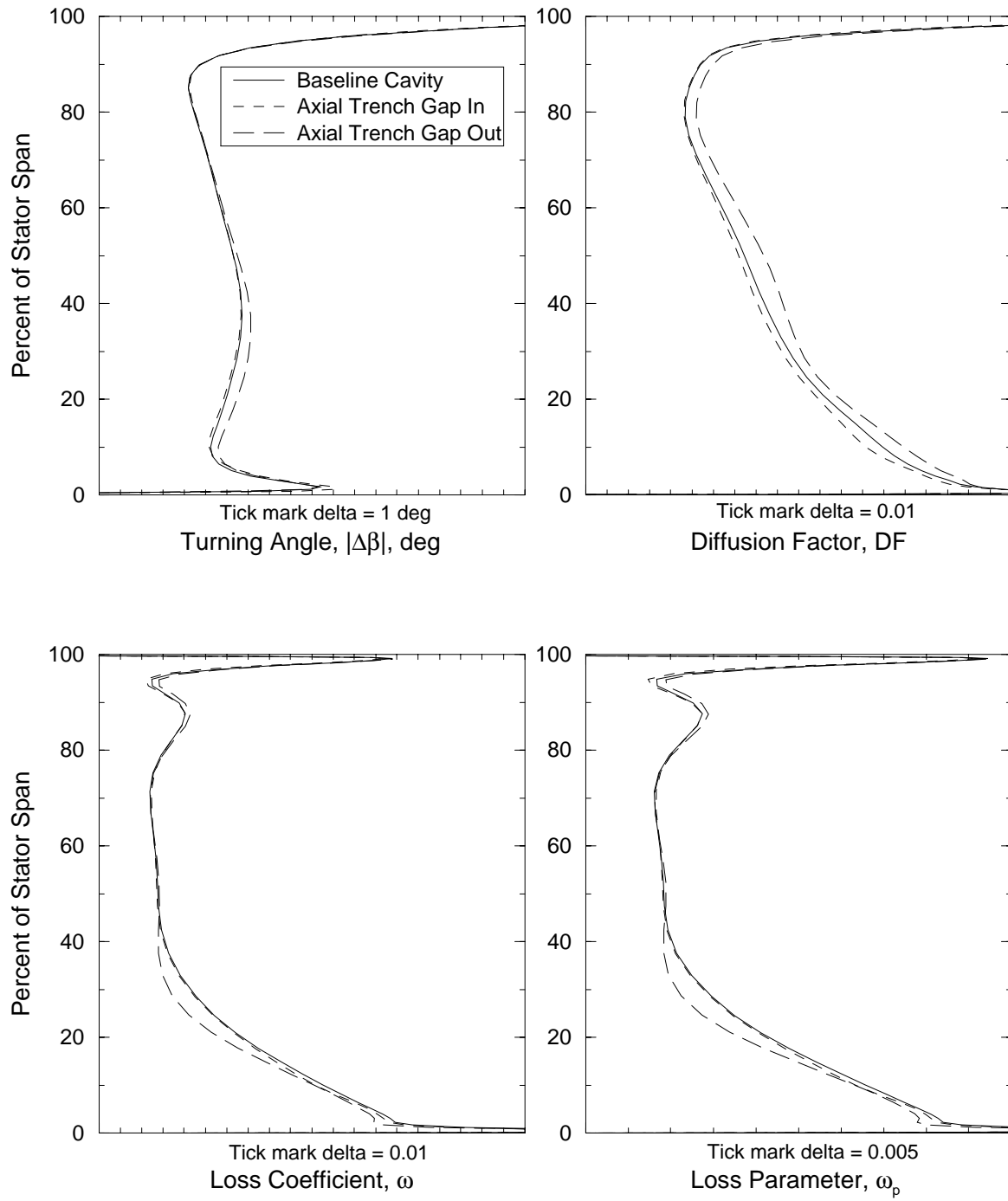


Figure 4.43: Radial profiles of stator blade performance parameters measured across the stator blade for variations of the Axial Trench Gap parameter.

4.13 Hub Corner Parameter

Solutions from the High-Speed Compressor Study displayed interesting rotating flow structures in the seal cavity trenches just below the hub flowpath. In order to determine the stability of these “driven cavity” vortices, modifications were made to the corner of the hub surface on the rotor wheel. The surface was either rounded into the seal cavity trench or rounded back by a small amount as shown in Figure 4.44. As shown earlier in Figure 4.13, neither one of these modifications appeared to affect the stator blade or the seal cavity flow to a great extent.

Particle traces for these two cases in comparison to the Baseline case are shown in Figure 4.45. The flow looks very similar to the baseline flow with some minor exceptions. In the downstream trench when the hub corners are turned in, the driven cavity structure appears to be surrounded by the extended rotating hub surface. This increase in wetted rotating area in contact with the leakage flow accounted for the increase over the baseline value of downstream trench tangential velocity shown in Figure 4.13. Radial profiles of flow velocities, flow angles, and stator blade performance are shown in Figures 4.46, 4.47, and 4.48, respectively. Overall, there were no significant differences between the cases. The small differences in the tip region in the distribution of loss coefficient may be attributed to possible tip region shedding from a small region of reversed flow. When the hub corners were turned out rounding over the sharp corner, the stator blade did not turn the flow quite as much and was therefore less loaded than the Baseline case.

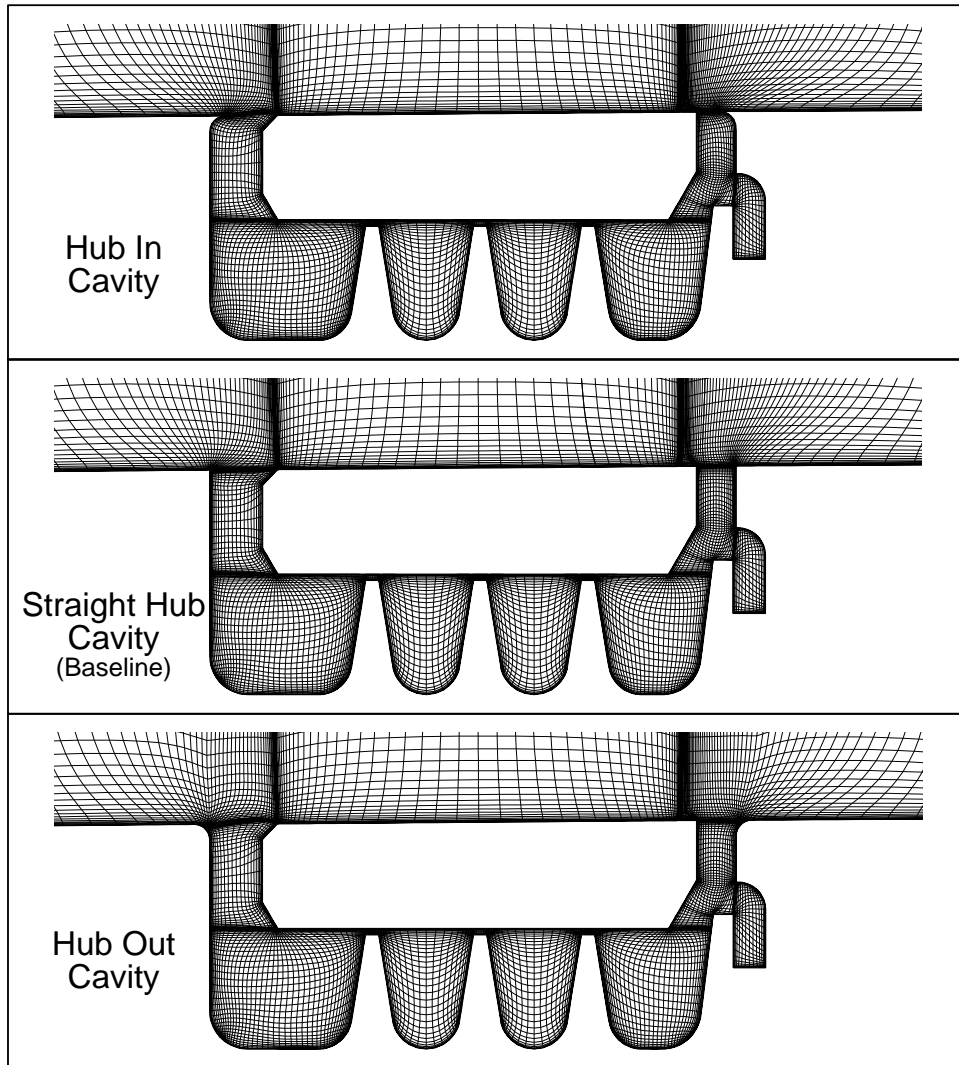


Figure 4.44: Meridional plane grids showing the variation of the Hub Corner Treatment parameter.

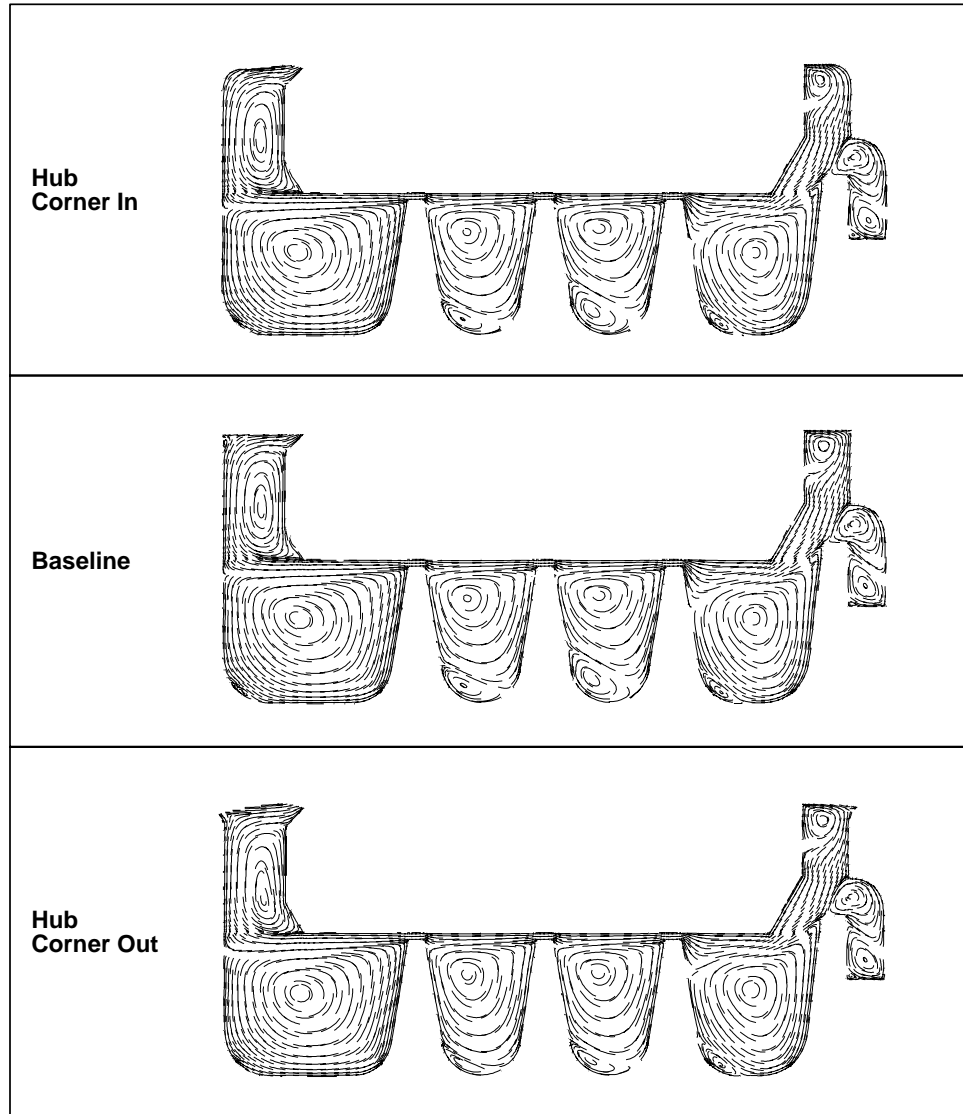


Figure 4.45: Axisymmetrically-averaged particle traces within the seal cavity for the Hub Corner parameter series.

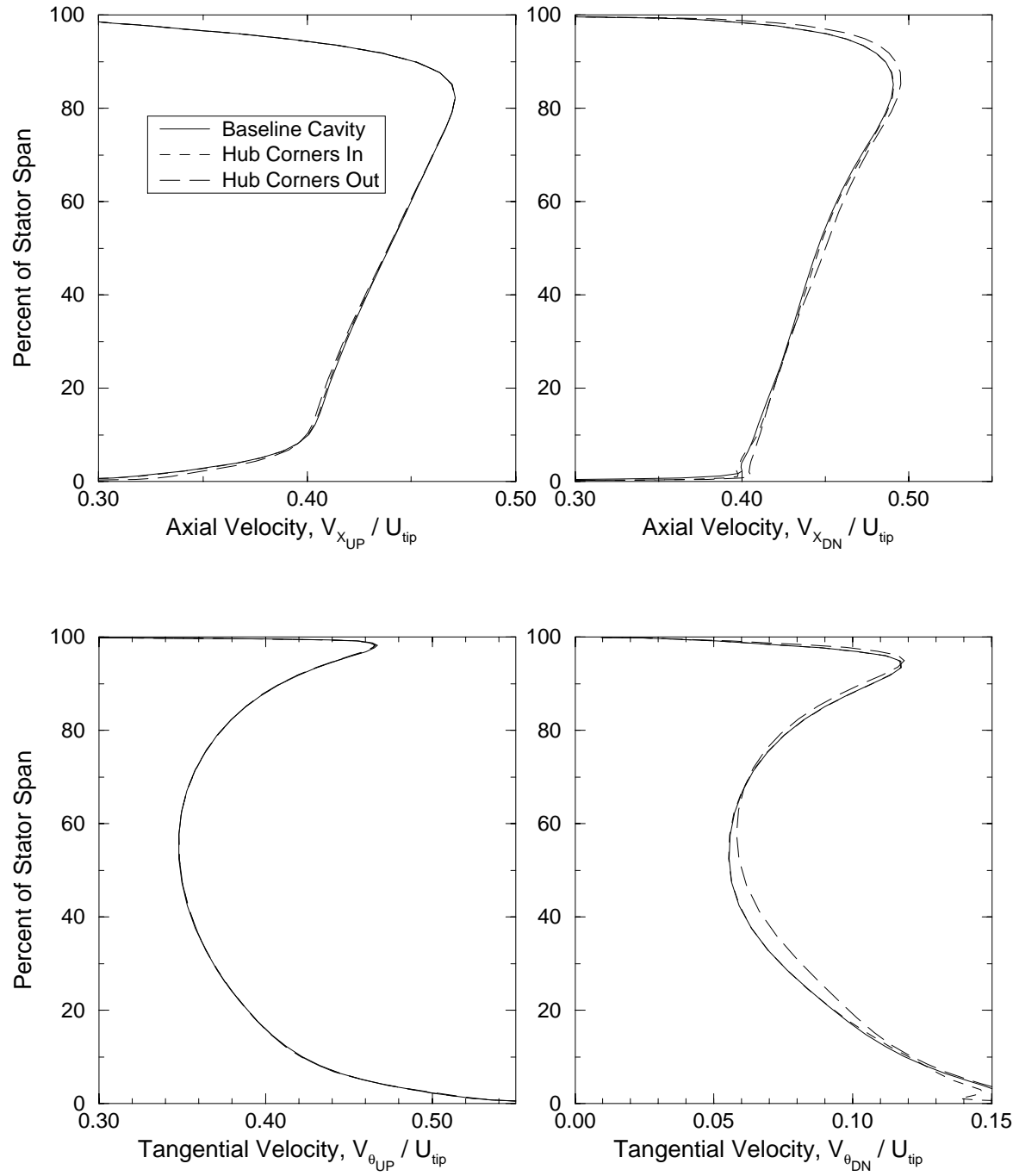


Figure 4.46: Radial profiles of axial and tangential velocities upstream and downstream of the stator blade for variations of the Hub Corner parameter.

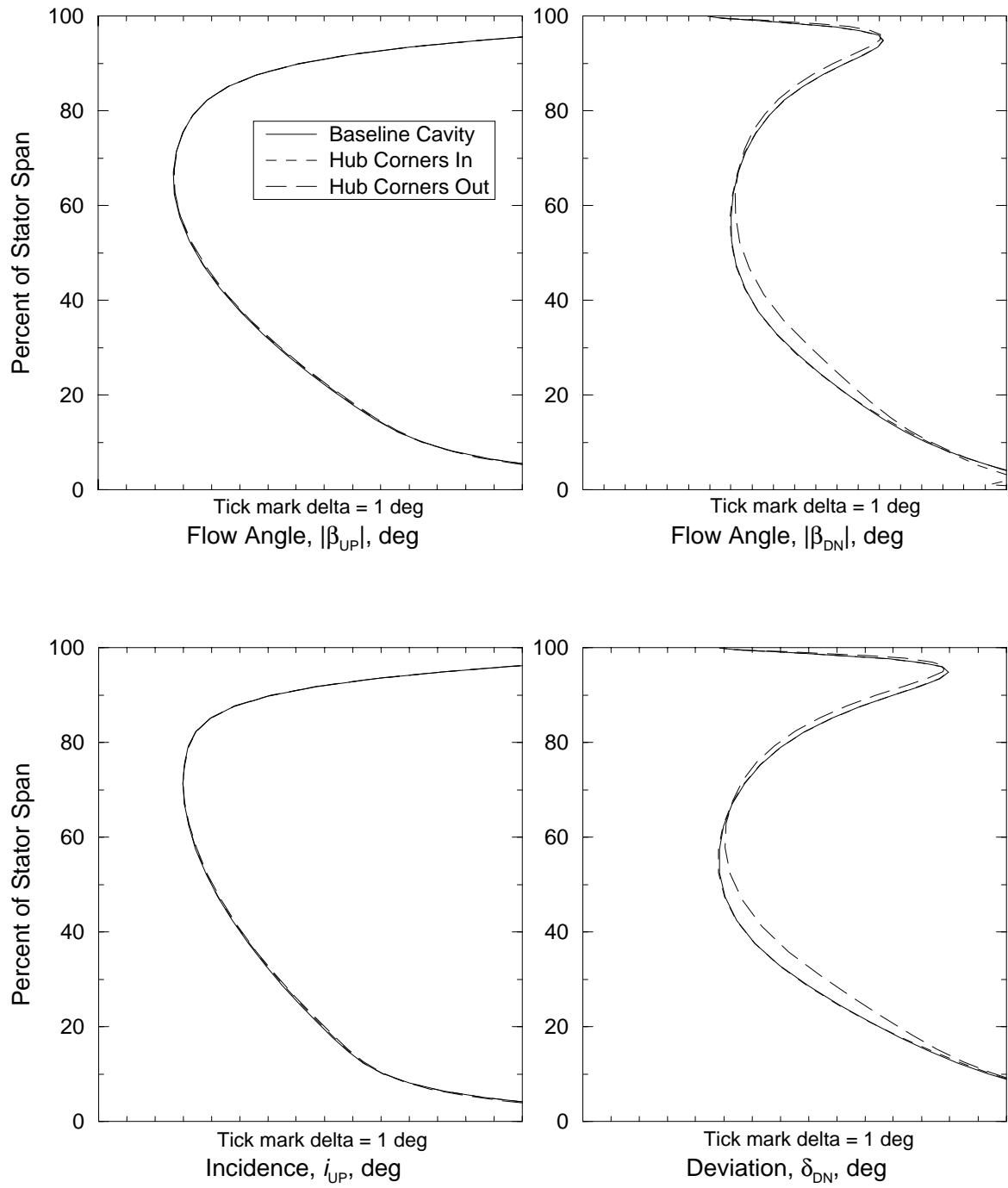


Figure 4.47: Radial profiles of flow angles upstream and downstream of the stator blade, and incidence and deviation for variations of the Hub Corner parameter.

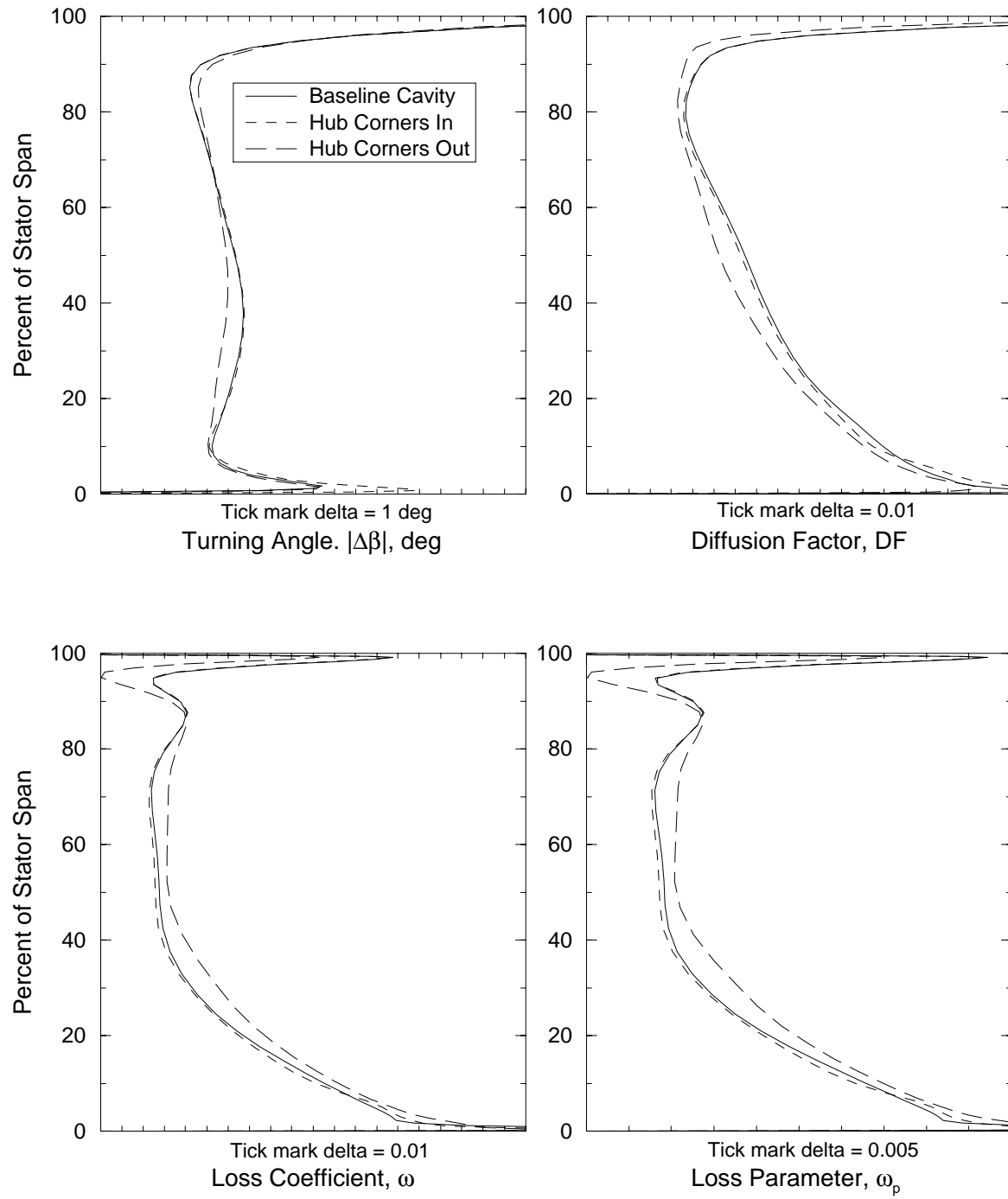


Figure 4.48: Radial profiles of stator blade performance parameters measured across the stator blade for variations of the Hub Corner parameter.

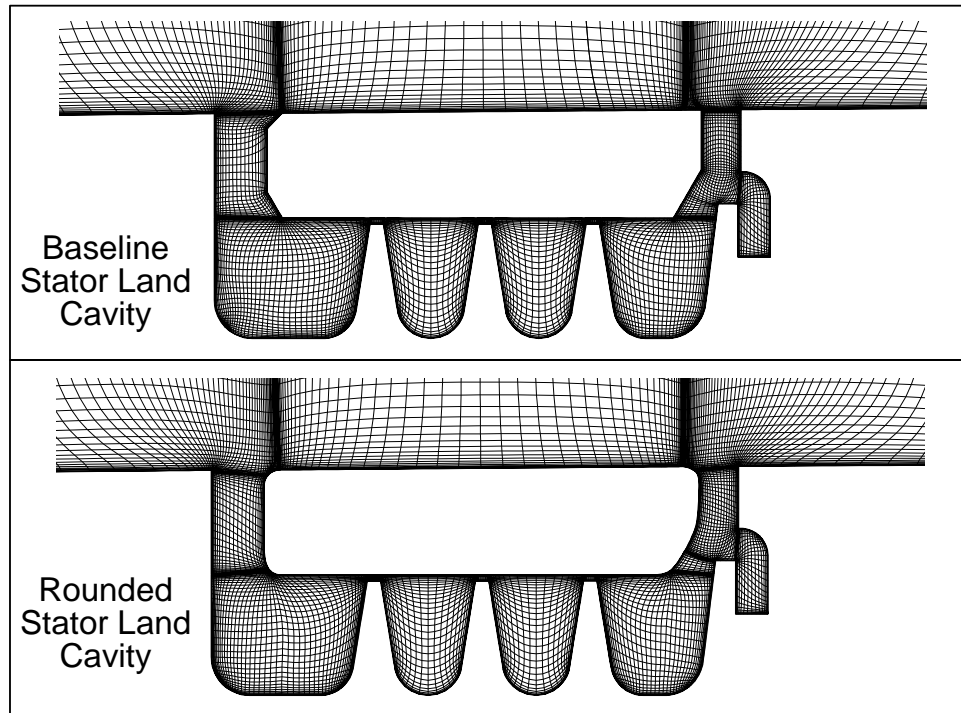


Figure 4.49: Meridional plane grids showing the variation of the Stator Land Edge Treatment parameter.

4.14 Stator Land Edge Parameter

A minor stator land modification was tested to determine the effect of the shape of the stator land on the stator flow. The faceted corners of the stator land geometry presented in the original cavity layout drawing were rounded as shown in Figure 4.49. This modification was not expected to create any large variations in the stator flow-field, but was tested to determine the sensitivity of the flow to the shape of stator land. From the results collected for this study, the expectation of little effect proved true. All of the rounded stator land results presented in Figure 4.13, comparing all of the parameter cases tested, did not vary significantly from the baseline configuration.

The axisymmetric particle traces, presented in Figure 4.50, show little differences between two cases. The radial distributions, shown in Figures 4.51, 4.52, and 4.53, also show little variation. This parameter appeared to have the weakest effect on the stator flow of any of those tested.

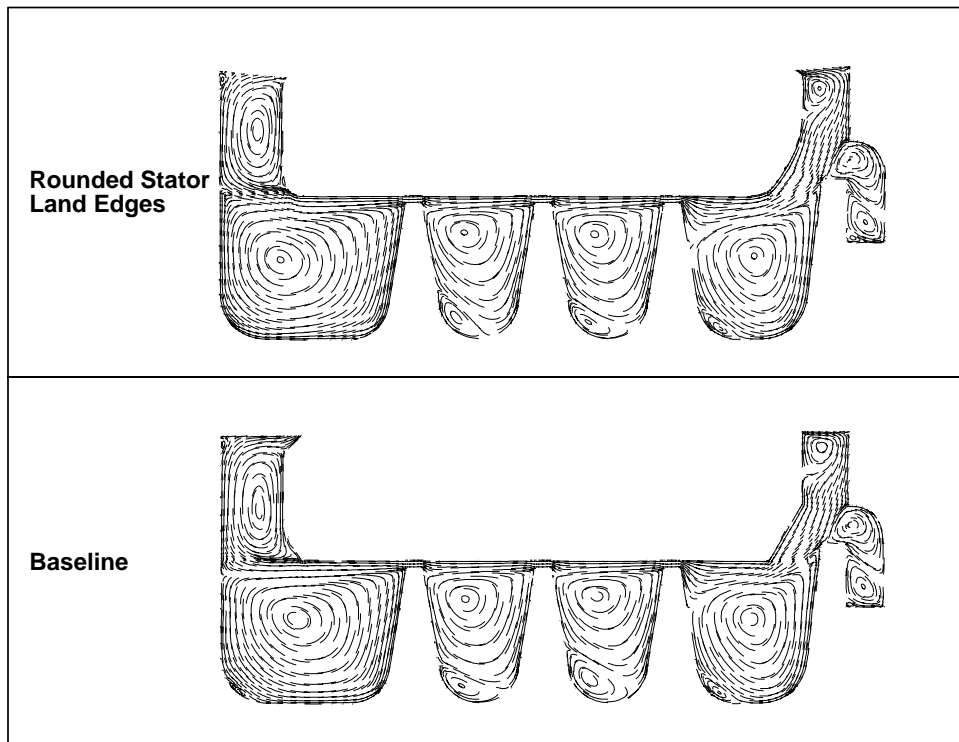


Figure 4.50: Axisymmetrically-averaged particle traces within the seal cavity for the Stator Land Edge parameter.

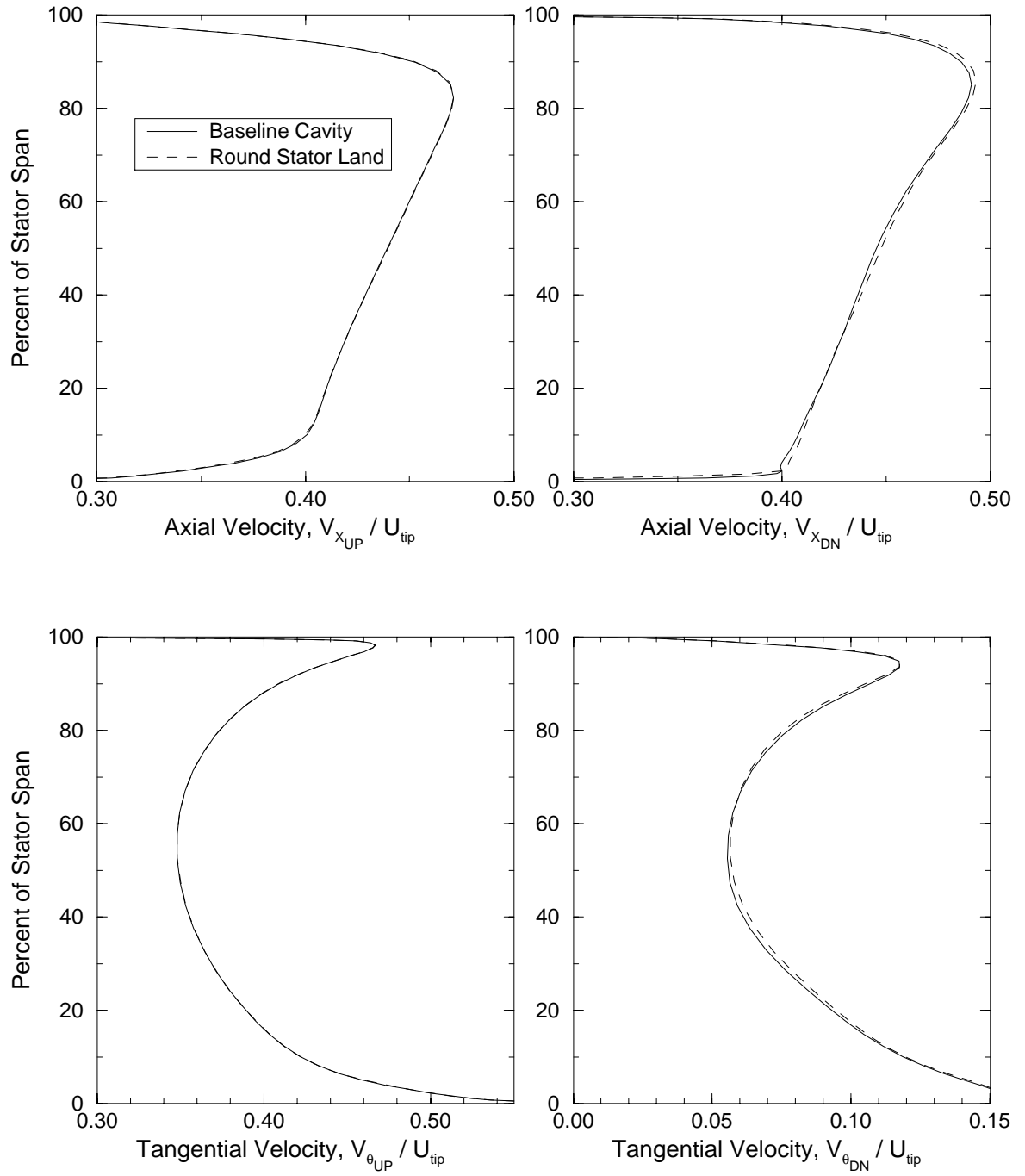


Figure 4.51: Radial profiles of axial and tangential velocities upstream and downstream of the stator blade for variations of the Stator Land Edge parameter.

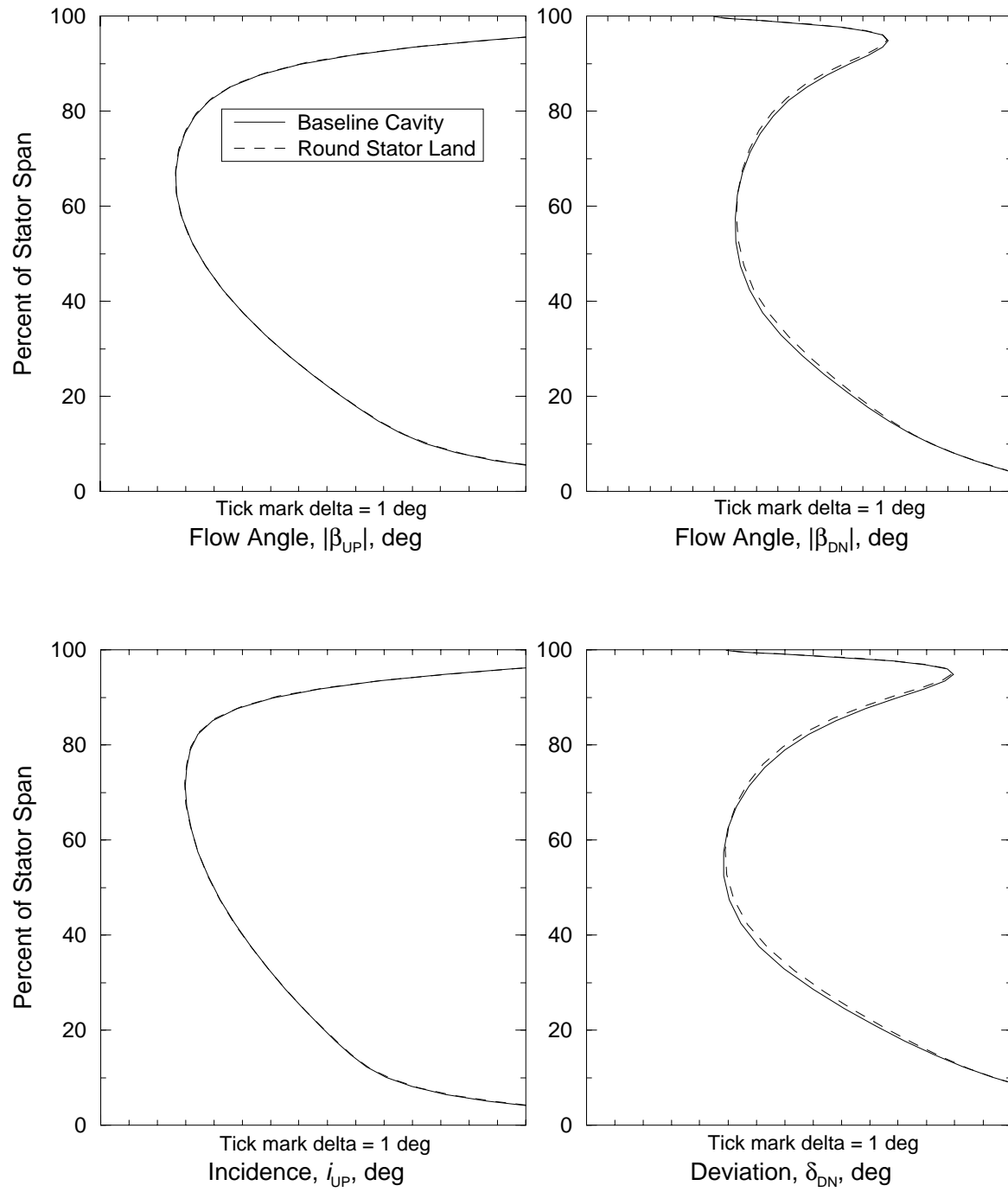


Figure 4.52: Radial profiles of flow angles upstream and downstream of the stator blade, and incidence and deviation for variations of the Stator Land Edge parameter.

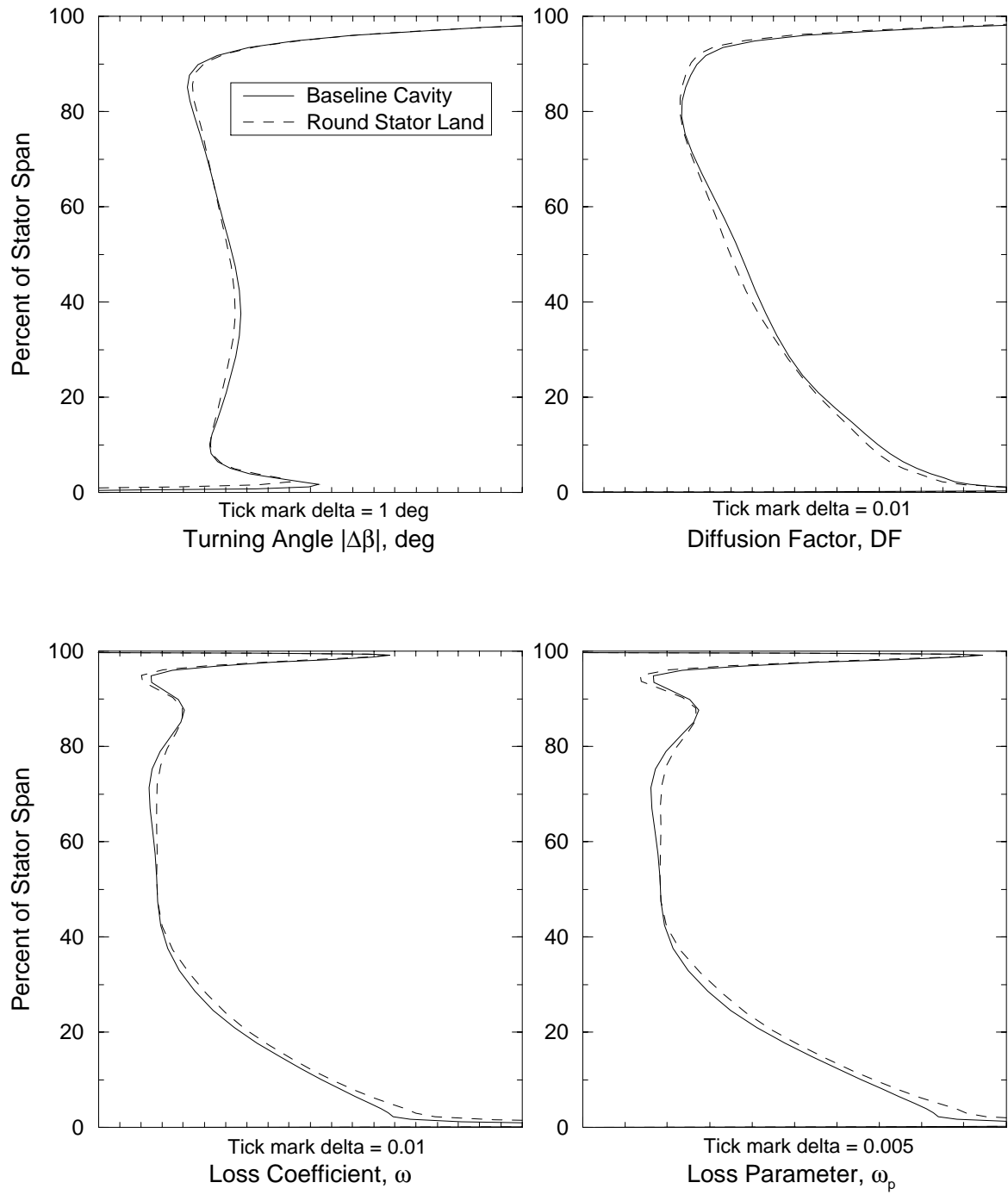


Figure 4.53: Radial profiles of stator blade performance parameters measured across the stator blade for variations of the Stator Land Edge parameter.

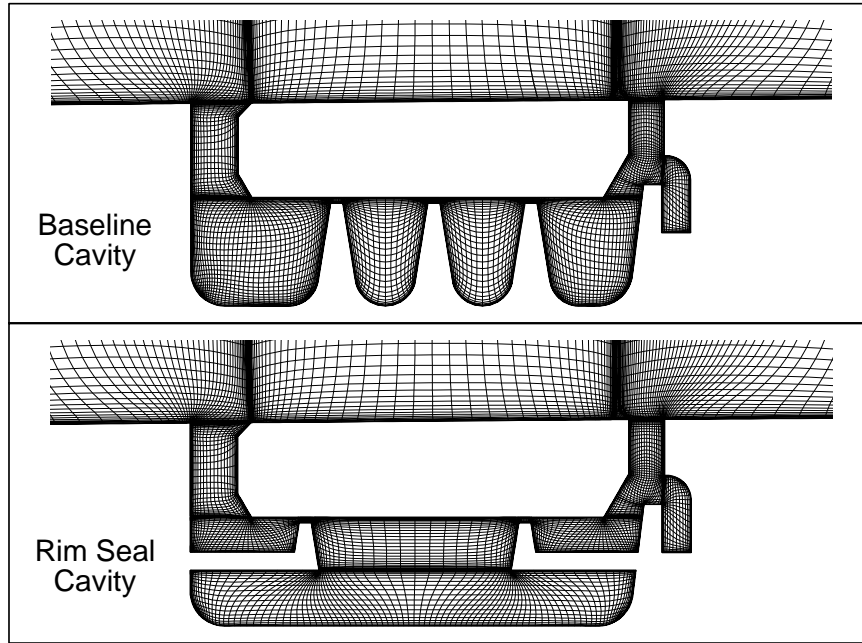


Figure 4.54: Meridional plane grids showing differences between the Baseline configuration and the Rim Seal configuration.

4.15 Rim Seal Cavity Configuration

In addition to the many modifications to the baseline triple-knife seal investigated in the parameterized study, a simple rim seal configuration was solved as an alternative seal geometry. The rim seal geometry differed most significantly from the labyrinth knife seal in the way the seal teeth were supported. The labyrinth seal configuration supported the knife seal teeth from the base of the spacer under the stator land, whereas the rim seal configuration supported the seal teeth from extensions off of the rotor wheels. The rim seal geometry is shown along with the baseline seal cavity configuration in Figure 4.54. By attaching the seal teeth to the sides of the rotor wheel, the cavity depth could have been increased without having to extend the teeth height; however, the rim seal geometry used in this investigation did not lower the base of the seal cavity in order to determine the effect of the rim seal teeth only. The seal tooth clearance was kept at the same value as the baseline configuration. Since only two knife seals were used, it was assumed that this rim seal geometry would perform similarly to a double labyrinth knife seal.

Particle traces were released in the axisymmetrically-averaged cavity solution to describe the flow character of the rim seal and are shown in Figure 4.55. The upstream and downstream seal cavity trenches look similar to the baseline flow with driven cavities in both trenches. The regions of the seal cavity below the trenches, but before the knife edges, is similar in character to when the cavity depth was halved (see Figure 4.28). The interior of the cavity consisted of a collection of vortices.

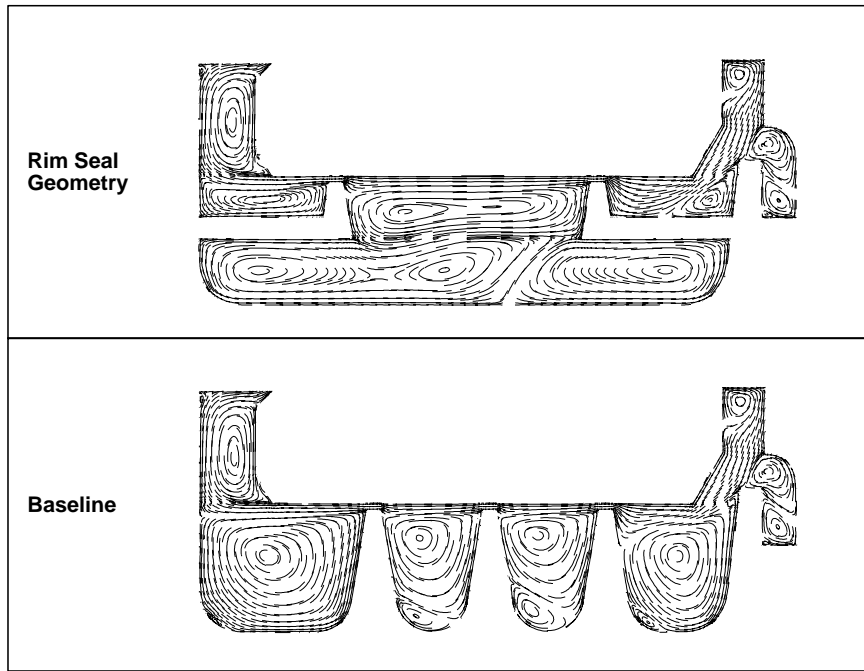


Figure 4.55: Particle traces released in the cavity region of the Rim Seal configuration.

Radial profiles for the rim seal geometry were calculated and compared with the baseline configuration results in Figures 4.56, 4.57, and 4.58. The seal cavity mass flow was found to be 0.65% of the main passage mass flow, whereas the baseline seal cavity flow was 0.60%. For the most part, there were no differences between the two seal configuration radial profiles.

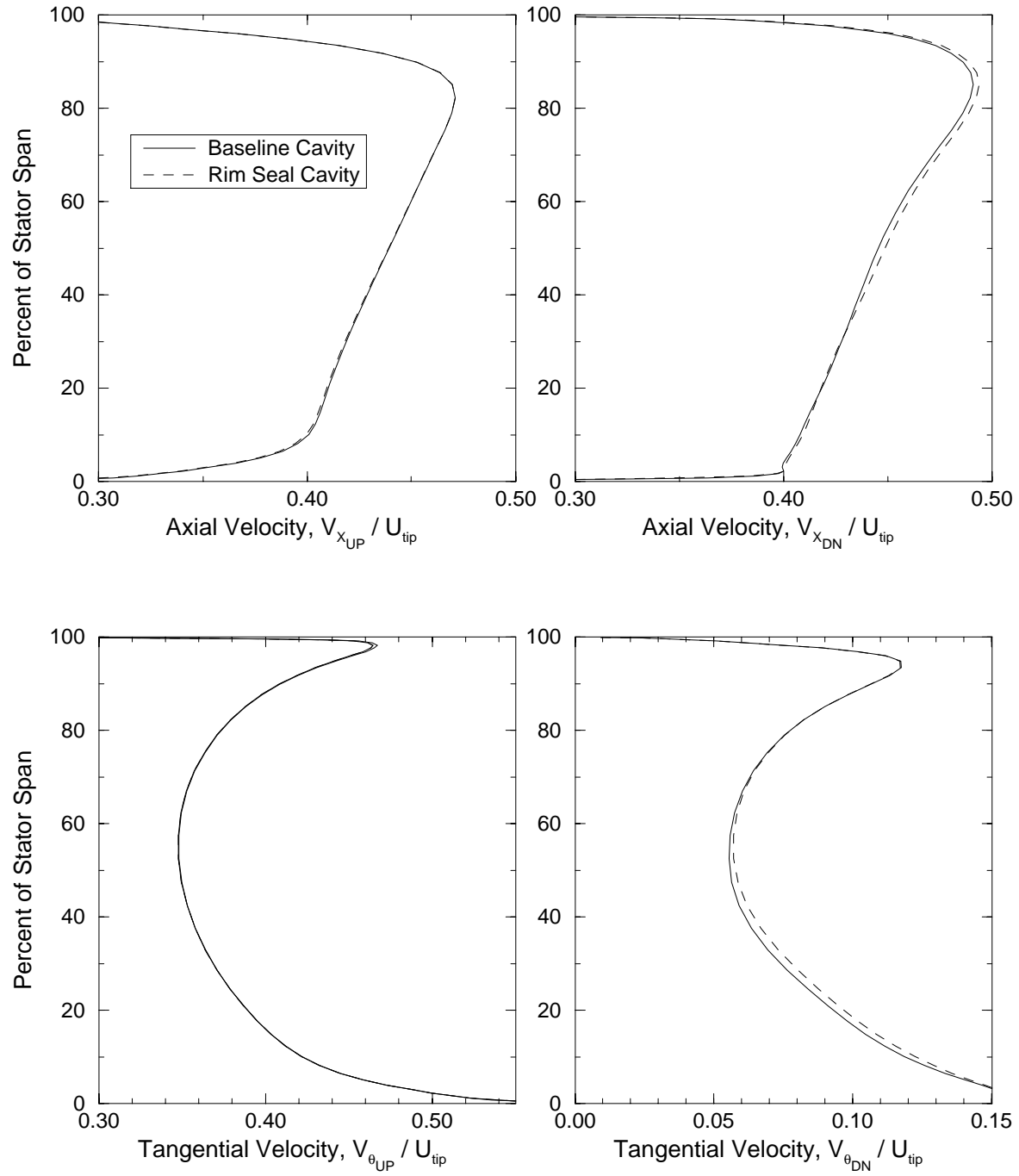


Figure 4.56: Radial profiles of axial and tangential velocities upstream and downstream of the stator blade for the Rim Seal Geometry.

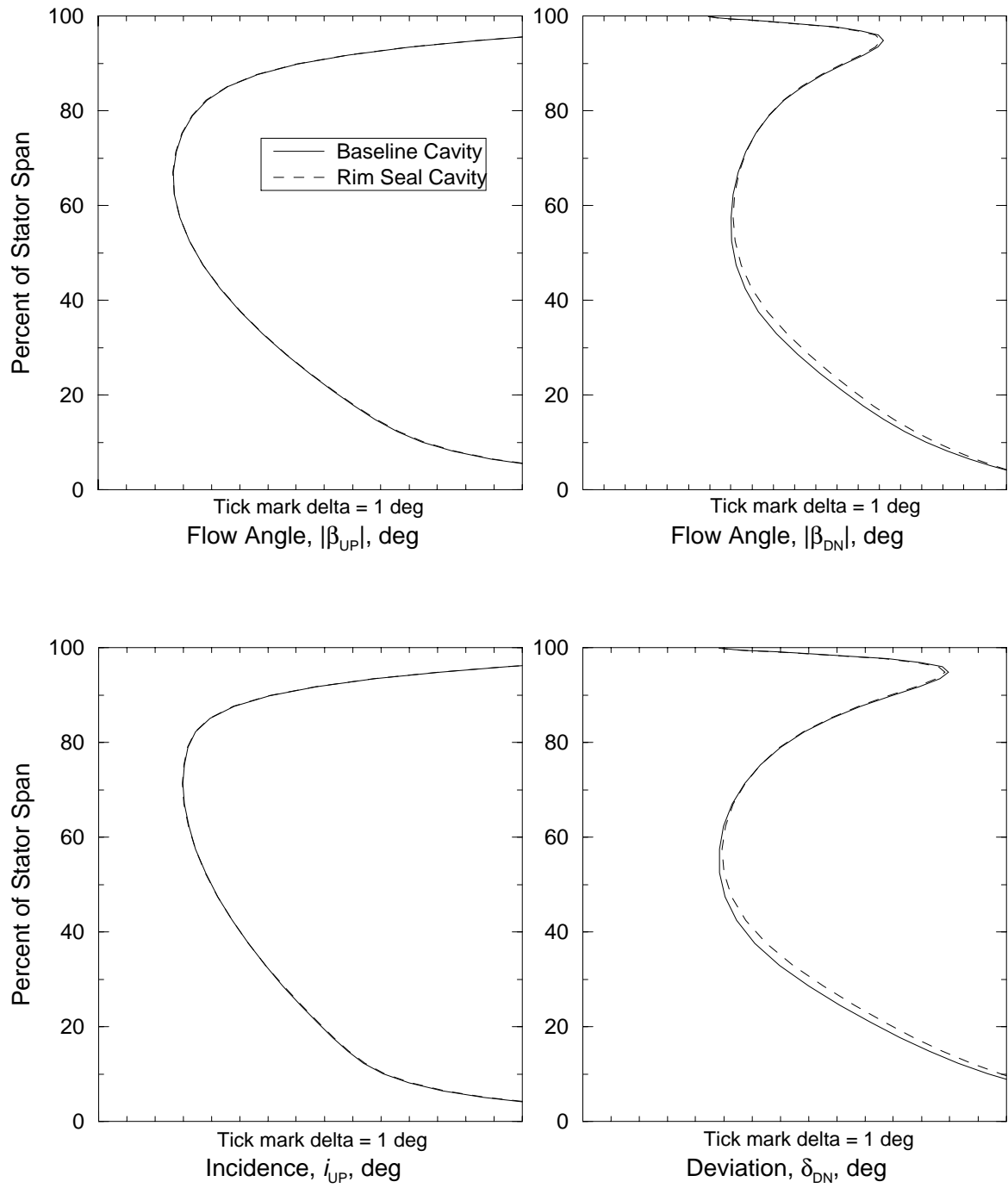


Figure 4.57: Radial profiles of flow angles upstream and downstream of the stator blade, and incidence and deviation for the Rim Seal Geometry.

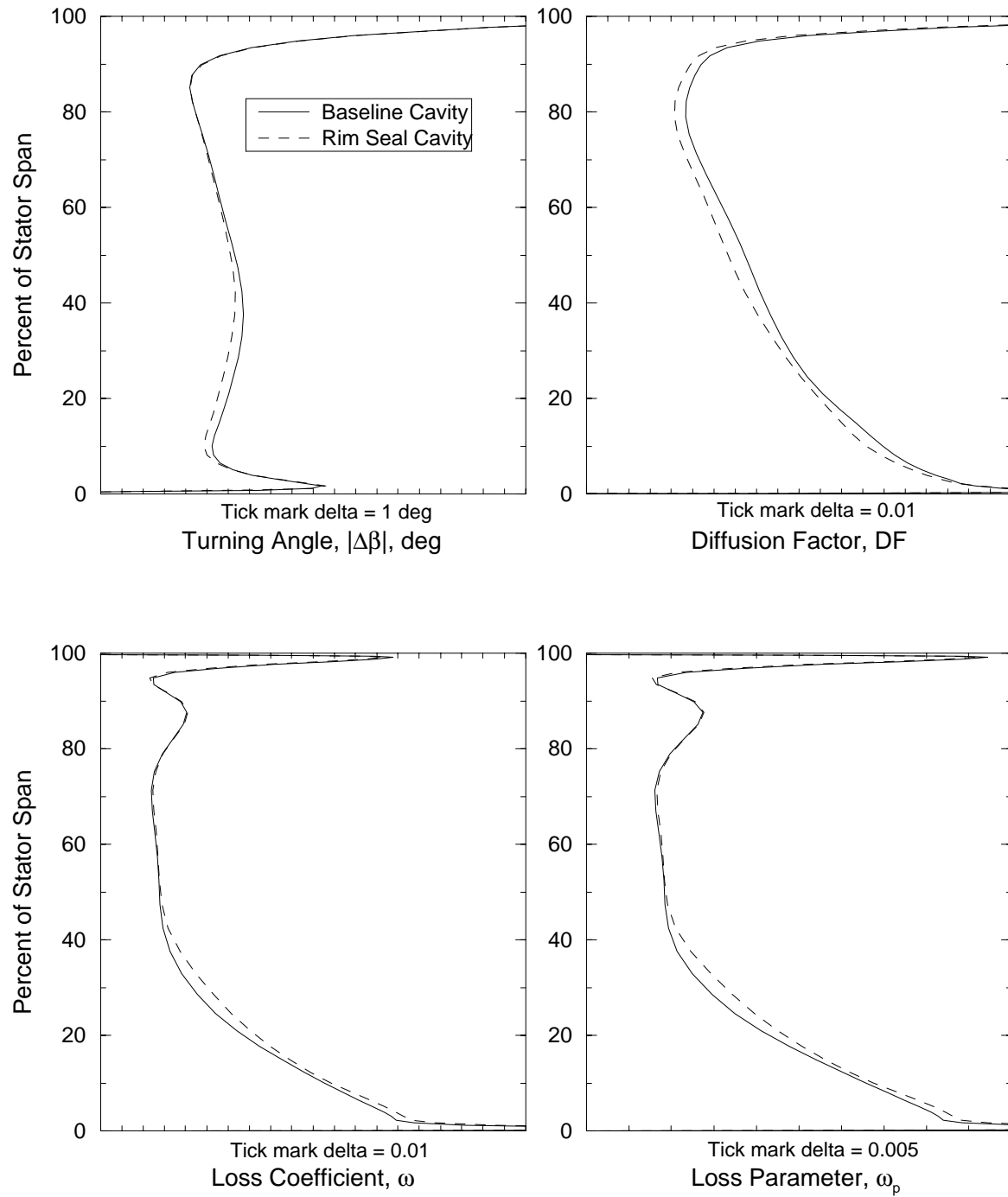


Figure 4.58: Radial profiles of stator blade performance parameters measured across the stator blade for the Rim Seal Geometry.

Chapter 5

CONCLUSIONS

The flow through a compressor inner-banded stator seal cavity and its interaction with the stator flowfield were investigated through the use of CFD analysis using the *ADPAC* flow solver. Several significant observations, made throughout this investigation, are presented in this chapter. This seal cavity investigation was divided into two main parts: a High-Speed Compressor Study and a Seal Cavity Parameterized Study. This chapter focuses on the major conclusions drawn from those studies.

The High-Speed Compressor Study simulated the coupled flowfield through a stator and an inner-banded stator seal cavity. The modeled seal cavity was selected from the eighth stage of the Allison Advanced Subsonic Technologies (AST) Candidate compressor. The seal cavity geometry consisted primarily of a triple-knife labyrinth seal; a single-knife version of this seal cavity geometry was also tested. A grid resolution study performed as part of the high-speed study showed that the numerical flow solution became grid independent with approximately 500,000 mesh points divided evenly between the stator main flow path and the seal cavity flow path. As the grid was refined, the stator passage mass flow and the seal cavity leakage mass flow increased asymptotically to constant values. The leakage flow rate for the nominal knife gap was 1.74% of the stator passage mass flow. When the gap was doubled, the leakage flow increased to 2.50%, and when the knife was completely removed, the leakage mass flow rate jumped to 3.56%.

The seal cavity leakage flow entered the downstream seal cavity trench and flowed through the first knife tip gap. The flow then traveled across the series of knives and impinged upon the upstream spinning rotor wheel. The leakage flow then turned radially outward, exited the seal trench, and re-entered the stator main flow near the stator land. As the leakage flow passed through the seal cavity, the tangential velocity increased from nearly zero to approximately 75% hub wheel speed (for the Baseline case). This increase in tangential momentum, in addition to a temperature increase due to windage, caused a significant increase in the total temperature of the leakage flow. Since the leakage flow exited the cavity with a higher tangential velocity than the main flow, the flow incidence on the stator blade very near the hub was up to 20 degrees higher than the mid-span value. This caused a region of flow to separate on the suction surface of the stator blade near the hub. As the leakage mass flow through the seal cavity increased, the exit tangential velocity of the leakage flow decreased

to closer to 50% hub wheel speed reducing the high incidence on the stator blade near the hub. This in turn reduced the size of the separated region on the suction side of the stator blade. The injection of this high tangential-momentum seal cavity leakage flow immediately upstream of the stator blade leading edge was identified as an important flow feature that needed to be considered in the compressor design process.

Several other interesting flow features were discovered from the numerical solutions of the seal cavity. In both of the seal cavity trenches connecting the cavity to the main flow path, “driven cavity”-like flow structures existed. The driving potential for these structures comes from the main passage flow and the leakage flow traveling through the seal cavity more than from the disk pumping action of the neighboring rotor wheels. This was illustrated as the downstream trench driven flow structure rotated in the direction opposite to the disk pumping action; however, it was also reduced in size due to this opposing force in comparison to the corresponding upstream trench region where the disk pumping force was in the direction of rotation.

The distributions of radial flow along the hub boundary between the seal cavity and the stator flow path were also of interest. Due to the adverse pressure gradient, the majority of the flow entered the seal cavity downstream of the stator blade and exited upstream. However, there were regions along this interface boundary of the seal cavity where reversed flow was calculated. In the upstream cavity, negative radial velocities were calculated in the region immediately in front of the stator blade; the potential field of the stator blade forced flow downward into the seal cavity. Downstream of the stator blade, positive radial velocity regions appeared in the high loss region of the stator blade wake.

A series of multiple blade row solutions were collected which determined the neighboring blade interactions with the seal cavity. Both the upstream and downstream rotor blade rows were included in the calculations. The rotor blade rows were coupled to the stator blade row using either an exact unsteady communication boundary or using a mixing-plane boundary approximation. From a comparison between these solutions, the influence of the downstream rotor was directly tied to regions of high negative flow into the seal cavity. The influence of the upstream rotor was not nearly as strong. Studies of the upstream rotor in isolation indicated a shift in the rotor constant speed line when the effects of the stator seal cavity were included in the rotor inlet profile; the rotor passed less mass flow at the same pressure ratio.

Having established a better understanding of the flow characteristics of a high-speed inner-banded stator seal cavity, a parameterized study was initiated by identifying several geometric parameters affecting the configuration of the seal cavity. This parameter list was bounded by retaining only those geometric parameters that directly influenced the interaction between the stator passage flow and the leakage flow. The final list of parameters tested included: seal tooth gap, cavity depth, wheel speed, radial mismatch of hub flowpath, axial trench gap, hub corner treatments, and land edge treatments. A rim seal geometry was also studied to provide an alternative seal geometry to the triple-knife labyrinth seal. Several figures of merit were also identified in order to compare the effects of the different seal parameters. The configuration used as a baseline for the Seal Cavity Parameterized Study was a slightly

modified version of the model used in the high-speed study. The clearances on the triple-knife labyrinth seal were reduced to 0.010 inches which reduced the leakage mass flow rate to 0.60% of the stator main passage flow, a leakage flow rate more representative of current compressor design.

Pitchwise flow parameter distributions taken at incrementally deeper spanwise locations into the cavity trenches were calculated both upstream and downstream of the stator blade for the baseline seal cavity. These distributions showed again the mixed positive and negative radial flow across the hub boundary described above. The influence of the stator passage flowfield only affected the cavity trench flow down to -10% stator span into the trenches, after which the pitchwise distributions became essentially constant across the passage. The increase in the tangential velocity and total temperature happened very quickly after the leakage flow entered into the downstream trench. The leakage flow was spun up to over two-thirds of its final exit tangential velocity by -15% stator span.

For each of the parameter study cases, detailed results presented included particle traces describing the flow character and spanwise distributions of stator blade flow properties. The figures of merit derived from these results which were compared among the parameterized solutions included the amount of leakage flow, the drop in total pressure and rise in total temperature across the stator blade row, and the increase in tangential velocity through the seal cavity. For many of the parameters tested, no significant deviations from the Baseline case in these figures of merit were calculated; however, some significant trends were observed.

With respect to leakage flow figure of merit through the seal cavity, the size of the knife seal tooth gap was the most sensitive parameter varied. The amount of leakage flow varied almost linearly with increasing tooth gap. The seal cavity leakage flow rates predicted by *ADPAC* also agreed with results from a secondary flow analysis tool currently being used in the evaluation of seal cavity designs.

The influence of rotational wheel speed was most apparent in the tangential velocity of the seal cavity exit flow. In the Baseline case, particle traces followed the leakage flow as it re-entered the stator flow stream. Due to the high tangential velocity of the flow, most of the leakage flow traveled into and up along the pressure side of the stator to approximately 30% span. The particle traces from the lower wheel speed configuration tested showed the leakage flow to remain close to the hub. In addition to the visual indications of the path followed by the leakage flow, spanwise distributions of the change in total temperature across the stator blade showed the influence of the heated leakage flow.

In summary, the major conclusions of the Seal Cavity Flow Investigation can be briefly stated below roughly in the order covered in the previous chapters:

- Approximately 500,000 mesh points were needed to adequately resolve the coupled 3-D seal cavity and stator blade flow fields, split evenly between the two flowpaths.
- From the unsteady rotor-stator-rotor solutions, the downstream rotor blade position had a strong correlation to region of flow being pumped into the seal

cavity; the upstream rotor blade position did not have as strong of a correlation as the downstream rotor.

- Rotor performance is affected by the inclusion of seal cavity effects in the rotor inlet profile.
- Large increases in tangential velocity of leakage flow occur as it passes through the seal cavity (up to 75% of hub wheel speed mostly occurring in the downstream seal cavity trench). As the leakage mass flow increased the amount of tangential spin-up decreased.
- The exit tangential velocity of the seal cavity leakage flow affects the amount of stator blade suction side separation near the hub.
- Complex flow features were discovered, such as mixed positive and negative radial flow across *both* the upstream and downstream seal cavity / main flow interface regions and “driven cavity”-like flow structures in both seal cavity trenches.
- The average trends of the coupled stator and seal cavity flow can be solved using a 2-D axisymmetric model if the stator flow stream boundary conditions are correctly set.
- The leakage flow through the seal cavity becomes axisymmetric (no change across the blade passage) at approximately 10% of the stator span into both seal cavity trenches.
- The *ADPAC* prediction of leakage mass flow vs. tooth gap clearance matched well with other secondary flow prediction tools.
- When the hub wheel speed was lowered, the leakage flow remained near the hub surface through the stator passage rather than traveling up along the lower pressure surface of the stator blade.
- The rim seal geometry appeared to work almost as well as the baseline triple-knife labyrinth seal configuration.
- Since several of the parameterized cases (with the exception of lower wheel speed) showed little change from the Baseline case with respect to the critical tangential velocity increase through the seal cavity, as compressor designs evolve to higher wheel speeds, the leakage flow needs to be addressed in the design of the stator.

As was shown in this Seal Cavity Flow Investigation, the flow structure of the inner-banded stator seal cavity is extremely complex. This investigation has shed light on some of the important issues regarding the interaction between the stator blade passage flow and the seal cavity leakage flow and possibly only scratched the

surface of others. However, as compressor blade designers become more aggressive with their designs, secondary flows such as the seal cavity flow will become more important to the overall performance of the compressor.

Bibliography

- [1] Stocker, H. L., Cox, D. M., and Holle, G. F., “Aerodynamic Performance of Conventional and Advanced Design Labyrinth Seals with Solid-Smooth, Abradable, and Honeycomb Lands,” NASA CR-135307, 1977.
- [2] Tipton, D. L., Scott, T. E., and Vogel, R. E., “Labyrinth Seal Analysis Volume III: Analytical and Experimental Development of a Design Model for Labyrinth Seals,” Allison Gas Turbine Division of General Motors Corporation, AFWAL-TR-85-2103 Volume III, January 1986.
- [3] Phadke, U. P. and Owen, J. M., “Aerodynamic Aspects of the Sealing of Gas Turbine Rotor-Stator Systems, Part I: The behaviour of simple shrouded rotating-disc systems in a quiescent environment”, School of Engineering and Applied Sciences, University of Sussex Report 86/TFMRC/92, June 1987.
- [4] Phadke, U. P. and Owen, J. M., “Aerodynamic Aspects of the Sealing of Gas Turbine Rotor-Stator Systems, Part II: The performance of simple seals in a quasi-axisymmetric external flow”, School of Engineering and Applied Sciences, University of Sussex Report 86/TFMRC/93, June 1987.
- [5] Phadke, U. P. and Owen, J. M., “Aerodynamic Aspects of the Sealing of Gas Turbine Rotor-Stator Systems, Part III: The effect of non-axisymmetric external flow on seal performance”, School of Engineering and Applied Sciences, University of Sussex Report 86/TFMRC/94, June 1987.
- [6] Graber, D. J., Daniels, W. A., and Johnson, B. V., “Disk Pumping Test,” Air Force Wright Aeronautical Laboratories, AFWAL-TR-87-2050, 1987.
- [7] Johnson, B. V., Mack, G. J., Paolillo, R. E., and Daniels, W. A., “Turbine Rim Seal Gas Path Flow Ingestion Mechanisms,” AIAA Paper 94-2703, 1994.
- [8] Daniels, W. A., and Johnson, B. V., “Experimental Investigation of Turbine Disk Cavity Aerodynamics and Heat Transfer,” NASA Contract NAS8-37462, UTRC Reprt 93-957878-27, 1993.
- [9] Wellborn, S. R., “Effects of shrouded stator cavity flows on multistage axial compressor aerodynamic performance,” Ph.D. Thesis, Iowa State University, Ames, Iowa, 1996.

- [10] Buggeln, R. C., McDonald, H. "Labyrinth Seal Analysis Volume I: Development of a Navier-Stokes Analysis for Labyrinth Seals", Scientific Research Associates, Inc., AFWAL-TR-85-2103 Volume I, January 1986.
- [11] Athavale, M. M., Ho, Y. H., Forry, J. M., Munson, J. H., Hendricks, R. C., and Steinetz, B. M., "Simulation of Secondary Flow in Gas Turbine Disc Cavities and Interaction with the Main Flow Path," AIAA Paper 95-2620, 1995.
- [12] Athavale, M., Przekwas, A., Hendricks, R., and Steinetz, B., "Numerical Analysis of Intra-Cavity and Power-Stream flow Interaction in Multiple Gas-Turbine Disk Cavities," AIAA Paper 94-2803, 1994.
- [13] Przekwas, A., Athavale, M., and Hendricks, R., "Progress in Advanced Modeling of Turbine Engine Seal Flows," AIAA Paper 94-2803, 1994.
- [14] Hall, E. J., Delaney, R. A., and Bettner, J. L., "Investigation of Advanced Counterrotation Blade Configuration Concepts for High Speed Turboprop Systems: Task I - Ducted Propfan Analysis," NASA CR 185217, NASA Contract NAS3-25270, 1990.
- [15] Hall, E. J. and Delaney, R. A., "Investigation of Advanced Counterrotation Blade Configuration Concepts for High Speed Turboprop Systems: Task II - Unsteady Ducted Propfan Analysis - Final Report," NASA CR 187106, NASA Contract NAS3-25270, 1992.
- [16] Hall, E. J. and Delaney, R. A., "Investigation of Advanced Counterrotation Blade Configuration Concepts for High Speed Turboprop Systems: Task V - Counterrotation Ducted Propfan Analysis, Final Report," NASA CR 187126, NASA Contract NAS3-25270, 1992.
- [17] Hall, E. J., Topp, D. A., Heidegger, N. J., and Delaney, R. A., "Investigation of Advanced Counterrotation Blade Configuration Concepts for High Speed Turboprop Systems: Task VIII - Cooling Flow/Heat Transfer Analysis, Final Report," to be published, NASA Contract NAS3-25270, 1994.
- [18] Hall, E. J., Topp, D. A., Heidegger, N. J., and Delaney, R. A., "Investigation of Advanced Counterrotation Blade Configuration Concepts for High Speed Turboprop Systems: Task VII - Endwall Treatment Inlet Flow Distortion Analysis Final Report", NASA Contract NAS3-25270, NASA CR-195468, July, 1995.
- [19] Hall, E. J., and Delaney, R. A., "Investigation of Advanced Counterrotation Blade Configuration Concepts for High Speed Turboprop Systems: Task V - Unsteady Counterrotation Ducted Propfan Analysis - Computer Program Users Manual," NASA CR 187125, NASA Contract NAS3-25270, 1993.
- [20] Hall, E. J., and Delaney, R. A., "Investigation of Advanced Counterrotation Blade Configuration Concepts for High Speed Turboprop Systems:

Task VIII - Film Cooling/Heat Transfer Analysis - Computer Program Users Manual,” NASA CR 195360, NASA Contract NAS3-25270, 1994.

- [21] Hall, E. J., and Delaney, R. A., “Investigation of Advanced Counterrotation Blade Configuration Concepts for High Speed Turboprop Systems: Task VII - ADPAC User’s Manual”, NASA Contract NAS3-25270, NASA CR 195472, July, 1995.
- [22] Jameson, A., Schmidt, W., and Turkel, E., “Numerical Solutions of the Euler Equations by Finite Volume Methods Using Runge-Kutta Time-Stepping Schemes,” AIAA Paper 81-1259, 1981.
- [23] Adamczyk, J. J., Celestina, M. L., Beach, T. A., and Barnett, M., “Simulation of Three-Dimensional Viscous Flow Within a Multistage Turbine,” ASME Paper 89-GT-152, 1989.
- [24] Jorgensen, P. C. E., and Chima, R. V., “An Unconditionally Stable Runge-Kutta Method for Unsteady Flows,” NASA TM 101347, 1989.
- [25] Ameri, A. A., and Arnone, A., “Navier-Stokes Turbine Heat Transfer Predictions Using Two-Equation Turbulence Closures”, AIAA Paper 92-3067, 1992.
- [26] Steinbrenner, J., et. al. “The Gridgen 3D Multiple Block Grid Generation System,” Final Report WRDC-TR-90-3022, 1990.
- [27] Walatka, P., Buning, P. G., Pierce, L., and Elson, P. A., “PLOT3D User’s Manual, Version 3.6,” NASA TM-101067, 1990.
- [28] Owen, J. M. and Rogers, R. H., “Flow and Heat Transfer in Rotating-Disc Systems, Volume 1 - Rotor-Stator Systems,” Research Studies Press Ltd., Somerset, England, 1989.
- [29] Vaughan, C., “A numerical investigation into the effect of an external flow field on the sealing on a rotor-stator cavity,” D. Phil. thesis, University of Sussex, 1986.
- [30] Wellborn, S. R., Hall, E. J., Heidegger, N. J., and Delaney R. A., “Area of Interest 5 - Multistage Compressor Design Using Advanced CFD,” Bi-monthly Progress Report No. 1, NASA Contract NAS3-27725, May 1996.
- [31] Crook, A. J., and Delaney, R. A., “Investigation of Advanced Counterrotation Blade Configuration Concepts for High Speed Turboprop Systems: Task III-Advanced Fan Section Grid Generator Final Report and Computer Program User’s Manual,” NASA CR-187129, 1991.
- [32] Wellborn, S., private communications.
- [33] Chupp, R. E., “Computer Model for Internal Flow Network Analysis (BC88PLUS) - User’s Manual,” Allison Gas Turbine Division EDR-11830, June 1984.

Appendix A

ADPAC Solution Collection on Various Platforms

Because this parameterized study involved 3-D Navier-Stokes simulations, a large number of CPU hours was required to complete all of the solutions for the several test configurations. However, the total calendar time required for these solutions was reduced by making use of the portability and flexible parallelization of the *ADPAC* code. Solutions were collected on several different computing platforms simultaneously during the Seal Cavity Flow Investigation.

Initial seal cavity solutions were collected on the LACE cluster located at the NASA Lewis Research Center. At the time of use, the LACE cluster was comprised of several IBM RS/6000 560's networked together to simulate a parallel machine. To compliment the computational resources available on the LACE cluster, a proposal was submitted and approved through the NASA Computational Aerosciences (CAS) Parallel Systems project for access to the *davinci* cluster at NASA Ames Research Center to complete part of the parameterized study. The *davinci* cluster is a group of eight SGI Power Challenge L's. A sample case was also run on a Cray C-90 computer for comparison.

Results from a timing comparison on these machines are presented in Table A.1. This table includes a listing of computational times for a seal cavity test case run on the LACE cluster, a Cray C-90, and the *davinci* cluster using different parallel libraries (APPL, PVM, and MPI). The coupled stator and seal cavity meshes had approximately 550,000 points for these cases. The times listed in the table represent wallclock time from the start of a job submission script to the end of the script on the LACE and *davinci* machines, and represents the actual CPU time on the Cray machine. The CPU time used and the wallclock time for the *davinci* cluster should be equal as *davinci* uses a dedicated machine allocation system.

One reason for the dramatic increase in performance over the LACE cluster concerns the difference in the queuing systems. On the *davinci* cluster, only one job per machine was allowed; therefore, there was no job sharing. While on the LACE cluster, LSF balanced all jobs submitted over the available processors. This was good for small job throughput; however, it slowed down longer running jobs such as the seal cavity solutions that were spread over several processors. Calculated run times may

Name	Machine Type	Queueing System	Parallel Library Used	Number of Processors	Time* / Iteration / 100K Mesh Points
LACE Cluster (NASA Lewis)	IBM RS/6000 560's	LSF	APPL	8	32.79**
vonneuman (NASA Ames)	Cray C-90	NQS	n/a	1	8.51
Davinci Cluster (NASA Ames)	SGI Power Challenge L	PBS	APPL	8	4.34
Davinci Cluster	SGI Power Challenge L	PBS	PVM	8	3.30
Davinci Cluster	SGI Power Challenge L	PBS	MPI	8	2.21

* The times recorded in the table represent the wallclock time difference between the start and the stop of the execution script on each of the respective platforms, not directly the CPU time.

** The LACE Cluster performance is greatly affected by the LSF queueing system which allows multiple jobs sharing a single processor, whereas the Davinci Cluster under PBS provides dedicated CPU time.

Table A.1: Run times from three different computing resources for a typical seal cavity problem.

also have been affected by other factors such as operating system upgrades throughout the duration of solution collection.

REPORT DOCUMENTATION PAGE			Form Approved OMB No. 0704-0188	
Public reporting burden for this collection of information is estimated to average 1 hour per response, including the time for reviewing instructions, searching existing data sources, gathering and maintaining the data needed, and completing and reviewing the collection of information. Send comments regarding this burden estimate or any other aspect of this collection of information, including suggestions for reducing this burden, to Washington Headquarters Services, Directorate for Information Operations and Reports, 1215 Jefferson Davis Highway, Suite 1204, Arlington, VA 22202-4302, and to the Office of Management and Budget, Paperwork Reduction Project (0704-0188), Washington, DC 20503.				
1. AGENCY USE ONLY (Leave blank)		2. REPORT DATE December 1996		3. REPORT TYPE AND DATES COVERED Final Contractor Report
4. TITLE AND SUBTITLE Aeropropulsion Technology (APT) Task 23—Stator Seal Cavity Flow Investigation			5. FUNDING NUMBERS WU-509-10-11 C-NAS3-25950	
6. AUTHOR(S) N.J. Heidegger, E.J. Hall, and R.A. Delaney				
7. PERFORMING ORGANIZATION NAME(S) AND ADDRESS(ES) Allison Engine Company P.O. Box 420 Indianapolis, Indiana 46206-0420			8. PERFORMING ORGANIZATION REPORT NUMBER E-10340	
9. SPONSORING/MONITORING AGENCY NAME(S) AND ADDRESS(ES) National Aeronautics and Space Administration Lewis Research Center Cleveland, Ohio 44135-3191			10. SPONSORING/MONITORING AGENCY REPORT NUMBER NASA CR-198504	
11. SUPPLEMENTARY NOTES Project Manager, Michael D. Hathaway, Internal Fluid Mechanics Division, NASA Lewis Research Center, organization code 2640, (216) 433-6250.				
12a. DISTRIBUTION/AVAILABILITY STATEMENT Unclassified - Unlimited Subject Categories 02, 07, and 34 This publication is available from the NASA Center for AeroSpace Information, (301) 621-0390.			12b. DISTRIBUTION CODE	
13. ABSTRACT (Maximum 200 words) The focus of NASA Contract NAS3-25950 Task 23 was to numerically investigate the flow through an axial compressor inner-banded stator seal cavity. The Allison/NASA developed ADPAC code was used to obtain all flow predictions. Flow through a labyrinth stator seal cavity of a high-speed compressor was modeled by coupling the cavity flow path and the main flow path of the compressor. A grid resolution study was performed to guarantee adequate grid spacing was used. Both unsteady rotor-stator-rotor interactions and steady-state isolated blade calculations were performed with and without the seal cavity present. A parameterized seal cavity study of the high-speed stator seal cavity collected a series of solutions for geometric variations. The parameter list included seal tooth gap, cavity depth, wheel speed, radial mismatch of hub flowpath, axial trench gap, hub corner treatments, and land edge treatments. Solution data presented includes radial and pitchwise distributions of flow variables and particle traces describing the flow character.				
14. SUBJECT TERMS Compressor; Seal activity; CFD			15. NUMBER OF PAGES 146	
			16. PRICE CODE A07	
17. SECURITY CLASSIFICATION OF REPORT Unclassified	18. SECURITY CLASSIFICATION OF THIS PAGE Unclassified	19. SECURITY CLASSIFICATION OF ABSTRACT Unclassified	20. LIMITATION OF ABSTRACT	